Remote sensing of swell waves in the North Sea with Sentinel-1 Synthetic Aperture Radar

M. (Martijn) D. Kwant

Delft University of Technology

TU Delft

Deltares
Enabling Delta Life

The cover shows long crested swell waves running towards the shore in the absence of wind. A fortunate situation for local surfers, since these perfect surfing conditions are rare along the Dutch coast. The photograph was taken by the author on 17 October 2015 from the Pier in Scheveningen.

Remote sensing of swell waves in the North Sea with Sentinel-1 Synthetic Aperture Radar

by

M. (Martijn) D. Kwant

to obtain the degree of Master of Science
at the Delft University of Technology,
to be defended publicly on Thursday December 21, 2017 at 04:00 PM.

Student number:	4095871	
Project duration:	March 1, 2017 – December 22, 2017	
Thesis committee:	Prof. dr. ir. A. J. H. M. Reniers,	TU Delft
	Prof. dr. ir. M. Verlaan,	TU Delft, Deltares
	Dr. J. F. Lopez Dekker,	TU Delft
	Dr. ir. A. R. van Dongeren,	Deltares
	Dr. M. A. Eleveld,	Deltares

An electronic version of this thesis is available at http://repository.tudelft.nl/.
Data and scripts are available at https://github.com/mdkwant/msc-thesis on request.

TU Delft

Contents

Preface

This thesis is the result of several months of work at Deltares and the TU Delft and is submitted as part of my Msc. degree in Civil Engineering at Delft University of Technology. In this preface I would like to present the reader my personal motivation for this subject and show my gratitude to everyone who supported me during this research.

As long as I can remember, my favorite holidays were those close to the beach. The sun, the sand, the ocean, as a kid I could play in the water for weeks. During one of these holidays I tried windsurfing for the first time. It was incredibly difficult and I remember falling into the water countless times, but the joy and exhilaration when I did manage to windsurf sparked one of my passions for many years to come. There is something mystical about windsurfing. Being alone on the open oceans, with only a surfboard and sail which are powered by the wind, riding powerful swell waves created by a storms thousands of kilometers away. It is the ultimate experience.

It may come as no surprise that when the time came to choose a track for my Msc. Civil Engineering, Hydraulic Engineering was my first choice. I remember the first year of my Masters, sitting on the front row during courses such as Ocean Waves and Coastal Dynamics. These lectures inspired me to follow the specialization Coastal Engineering and expand my knowledge on waves. This time I learnt something about the waves I was normally surfing on. While windsurfing on the ocean, I could feel the waves slowing down or shoaling and refracting while approaching the coast. During wind gusts I could see capillary waves being generated by the wind and I observed wave-wave interactions when swell and wind waves ran perpendicular.

For my introduction into the world of remote sensing I have to thank Sierd de Vries, who was my supervisor during an additional thesis in Myanmar. For 6 months I lived in Yangon, where I combined wave buoy measurements, modeled wave data and satellite altimeter measurements to analyze the wave climate along the coast of Myanmar. These 6 months were probably the most inspiring time for me as a student. Living abroad changed my view of the world, it was a time where I met amazing people and made numerous friends. For my final thesis I wanted to combine my passion for waves with remote sensing. With the topic of this research (Remote sensing of swell waves in the North Sea with Synthetic Aperture Radar) we found the perfect combination of both worlds.

For me, one of the most difficult aspects of this thesis was understanding the field of radar and signal processing. Coming from a Civil Engineering background, many aspects of signal processing were new to me. This thesis taught me a lot about this interesting field and provided me with extra knowledge and an increased understanding of the world. This is also the reason why I take great pride in the implementation and development of a python based module which automatically processes Sentinel-1 SAR data. For reference, one year ago I had never programmed with Python.

This thesis could not have been produced without the help of a number of people. First of all I would like to thank my graduation committee for their work during this thesis. prof. Ad Reniers and prof. Martin Verlaan, who were always there to guide me through the different progress meetings and provide critical feedback on my research. I would thank Paco Lopez Dekker, who inspired me to increase my understanding of radar processing and helped with processing SAR and OCEANSAR data. I would like to thank Ap van Dongeren for proof-reading my report numerous times and providing excellent feedback. Last but not least, I would like to thank Marieke Eleveld for her incredible support during this thesis. Always open for any questions, providing feedback and improving my academic English, she inspired me to put my best foot forward. Without these people the thesis would not have been what it is today.

I ’d also like to thank Gerbrant van Vledder and Caroline Gautier who helped me in the earlier phase of my research to formulate my research question and find a knowledge gap. Part of my thesis was funded by the Flood Risk Early Warning team at Deltares, from which I would like to thank Daniel Twigt and Jan Verkade for making this money available and of course my colleagues at ZKS-MCI, in particular Annette Zijderveld, for hosting me.

This research could not have been completed without the use of several tools and data. First of all I would like to thank Rijkswaterstaat and Instituto Hidrográfico who provided wave buoy data during this thesis. I would also like to thank the European Space Agency (ESA) for making the Sentinel-1 radar data available. Programming for this thesis was done using Python, all software, tools and data are publicly available on github.

I would also like to thank my fellow interns at Deltares, who were always there to listen to my stories and struggles during this thesis. We had some great moments during the many lunch breaks and coffee breaks we shared, which made the past 9 months at Deltares a very enjoyable experience. At last I would like to thank my girlfriend Anne, for her tremendous support and patience during the last months of this thesis. Whenever I discovered something new, she had to endure lengthy stories on e.g. swell waves and remote sensing. And of course I would like to thank my parents for their unconditional support.

Martijn Kwant
5th December 2017, Delft

Abstract

The North Sea is known for its marine activities, which need ocean data for safe operations. The ocean surface is described using the two-dimensional wave spectrum. This ocean wave spectrum can be estimated using wave buoys, wave models or remote sensing techniques. Wave buoys and numerical models are known to contain inaccuracies, which stresses the importance of other observation techniques. The solution of this thesis is using a remote sensing technique from Sentinel-1: Synthetic Aperture Radar.

The main imaging mechanism of SAR over the oceans is through resonant Bragg scattering with capillary wind-driven waves. Long ocean waves will modulate the returned Bragg scatter through a number of processes: tilt modulation (from a different local incidence angle), hydrodynamic modulation (resulting from the orbital velocities of ocean waves) and velocity bunching (caused by the relative motion of waves, compared to the motion of the satellite). This brings us to the main problem of this thesis, to what extent we can measure low-frequency swell waves from Sentinel-1 SAR images in the North Sea.

The method to derive wave data from SAR images consists of two steps: calculating the cross-spectrum between different sub-looks and estimating the ocean wave spectrum using a Modulation Transfer Function (MTF). In this thesis the first step, calculating the cross-spectrum was performed on Sentinel-1 SAR images. Pre-processing of the Sentinel-1 data consisted of three steps. First, the radar images were calibrated by converting pixel values to radiometric backscatter. Second, the antenna pattern from electronic steering of the satellite antenna was removed in a process called deramping. At last the SAR image were centered around the zero Doppler frequency by shifting the peak of the spectrum through demodulation. The most important step during processing of the SAR data was splitting the image in Frequency domain to create multiple time-separated sub-looks. Literature showed that calculating the cross-spectrum between sub-looks makes it possible to resolve the direction of the waves.

In total 11 case studies were analyzed in the North sea and 3 case studies in Portugal. Sentinel-1 SAR cross-spectra were verified and validated using wave buoy measurements and cross-spectra from simulated SAR images from OCEANSAR. In total, 6 North Sea case studies showed a positive result, where a swell peak was visible and the peak matched spectral data from wave buoys. SAR image cross spectra from Portugal, but also from the North Sea showed an elongation in range direction. This was caused by smoothing of the rectangular shaped pixels. Case studies from the Portuguese coast showed the best results, where SAR cross-spectra agreed well with buoy measurements.

Further improvements include the removal of non-linear contribution from cross-spectra, mapping of wave buoy measurements on the quasi-linear swell spectrum and calculating the full MTF. This thesis showed it is possible to measure low-frequency waves in the North Sea using Sentinel-1 Synthetic Aperture Radar. SAR images lead to a better understanding of the movements of swells and provide additional information for marine activities. A combination of wave buoy data, Sentinel-1 SAR data and OCEANSAR data showed measuring swell waves is possible with this state-of-the-art remote sensing technique.

Nomenclature

List of Acronyms

DFT	Discrete Fourier Transform
DN	Digital Number
DTAR	Distributed Target Ambiguity Ratio
ECMWF	European Centre for Medium-Range Weather Forecasts
ENVISAT ASAR	Envisat Advanced SAR
ESA	European Space Agency
FFT	Fast Fourier Transform
FM	Frequency Modulation
IFFT	Inverse Fast Fourier Transform
IW	Interferometric Wide Swath
L1B	Level 1B
L2	Level 2
LUT	Look Up Table
MTF	Modulation Transfer Function
NED	Netherlands
NS	North Sea
OASIS	Ocean ATI-SAR SImulator
OCEANSAR	Ocean SAR simulator (see: OASIS)
OSW	Ocean Swell Wave algorithm
POR	Portugal
PRF	Pulse Repetition Frequency
RADAR	Radio Detection and Ranging
RAR	Real Aperture Radar
RWS	Rijkswaterstaat
S-1	Sentinel-1 (constellation)
S-1A	Sentinel-1 A (satellite)
S-1B	Sentinel 1-B (satellite)
S1TBX	Sentinel-1 Toolbox
SAR	Synthetic Aperture Radar
SLC	Single Look Complex
SNAP	Sentinel Application Platform
SNR	Signal to Noise Ratio
SWAN	Simulating Waves Nearshore
TFD	Time-Frequency Domain
TOPSAR	Terrain Observation with Progressive Scans SAR
VH	Vertical transmit, Horizontal receive (polarization)
VV	Vertical transmit, Vertical receive (polarization)

Glossary

Azimuth	Direction parallel to the flight direction of the satellite. For Sentinel-1 radar images this is the y-axis.
Azimuth cut-off	Destructive imaging effect for waves traveling in azimuth direction, which limits the maximum wave length observed by SAR. Shows a linear relation with wind speed and wave height.
Bragg scattering	The main imaging mechanism of the ocean by SAR. Ocean waves with the same wave length as the radar interact constructively and return a backscattered signal.
Bragg waves	Ocean waves with approximately the same wave length as the radar sensor. For a C-band radar (6 cm) these are small capillary-gravity waves on the ocean.
Calibration	Also known as radiometric calibration, derivation of radar cross section using known LUT from the Digital Numbers of the original SAR image.
Cross-spectrum	A method show correlations between two SAR sub-looks.
Demodulation	Centering of the azimuth spectra around 0 Hz. The spectra are centered around the Doppler Centroid frequency after deramping.
Deramping	Removal of the frequency modulation which is caused by the steering of the satellite in TOPS mode (See TOPSAR).
Hydrodynamic modulation	An interaction between the orbital motions of Bragg scatterers and long ocean waves, which causes a local increase and decrease of the backscattered signal.
Imagette	A small subset of a radar image which is used during further processing. Instead of computing the ocean wave spectrum from an entire radar image, only a smaller imagette is used.
Interferometric Wide Swath	The Interferometric Wide swath mode is the main acquisition mode over land and coastal regions. IW mode captures three sub-swaths using Terrain Observation with Progressive Scans SAR (TOPSAR).
LUT	A table containing information used to process satellite data, usually delivered with the satellite product.
Polarization	Polarization refers to the orientation of the plane of the electric field (E), as opposed to the magnetic field (M).
Pulse Repetition Frequency	The number of pulses of a repeating signal in a specific time unit, normally measured in pulses per second .
Range	Direction perpendicular to the flight direction of the satellite. For Sentinel-1 radar images this is the x-axis.
Significant wave height	A characteristic wave height, defined as the mean of the highest one-third of the waves. Is also related to visual estimations of the wave height from marine traffic.
Single Look Complex	Single Look Complex (SLC) products consist of focused SAR data, georeferenced using orbit and attitude data from the satellite, and provided in slant-range geometry.
Speckle	Constructive and destructive interference of radar signal, which results in a black and white "grainy" appearance of radar images.
Swath	The area illuminated by a radar in range direction. S-1 SLC images consist of three separate sub-swaths.
Swell waves	Ocean gravity waves which have out run their local source. Typical for swell are long periods and evenly long crested waves. Also known as low-frequency waves.
Synthetic Aperture Radar	A satellite based radar system which uses a synthetic aperture to achieve a high resolution in along track direction.
Tilt modulation	Geometric effect which describes the variation in energy due to a different incidence angle of Bragg scattering elements along oceanic waves.
TOPSAR	A SAR technique used during the Sentinel-1 IW mode. With this mode the radar antenna is electronically steered in azimuth direction during the imaging process.
Variance density spectrum	A method to visualize the distribution of energy of ocean waves along different frequencies.
Velocity bunching	Constructive imaging effect for waves traveling in azimuth direction due to the imaging mechanism of SAR in azimuth.

List of Symbols

Radar:

i		Real, in-phase part of a complex number
q		Quadrature part of a complex number
j		Complex operator
M	[m^2/m^2]	Magnitude (or intensity) of a complex number
ϕ	[rad]	Phase of a complex number
θ	[deg]	Incidence angle
ω_r	[rad/s]	Steering rate of the antenna
v	[m/s]	Satellite velocity
T_{B1}	[s]	Measurement time
Δa	[m]	Azimuth resolution
Δr	[m]	Range resolution
Δr_{grd}	[m]	Ground range resolution
L_{sa}	[m]	Length of the synthetic aperture
β	[Hz]	Pulse bandwidth
c	[m/s]	Speed of light
λ_r	[m]	Radar wavelength
λ_s	[m]	Sea surface wavelength
λ_c	[m]	Azimuth cut-off wave length
θ	[deg]	Incidence angle
ψ		Wave number spectrum
ζ	[m]	Sea surface elevation
σ_i^0	[-]	Radiometric backscatter
A_i	[-]	SigmaNought(i)
DN_i	[-]	Digital Number
$\phi(\eta,\tau)$	[-]	Deramping phase term
k_t	[Hz/s]	Doppler centroid rate in the focused TOPS SLC data
τ	[s]	Range time
η	[s]	Azimuth time
η_{ref}	[s]	Reference azimuth time
k_a	[Hz/s]	Doppler FM rate
k_s	[Hz/s]	Doppler Centroid rate introduced by the scanning of the antenna
k_Ψ	[rad/s]	Antenna Steering rate
α	[-]	Conversion factor for scaling the raw time rate
v_s	[m/s]	Satellite velocity computed at mid-burst time η_{mid} by interpolation
η_{mid}	[s]	Mid burst zero Doppler azimuth time
λ	[m]	Radar wavelength
η	[s]	Zero Doppler azimuth time
NL_{burst}	[-]	Number of lines within a burst (same for all burst)
Δt_s	[s]	Azimuth Time interval between two SLC lines
ΔF	[Hz]	Azimuth frequency band width
η_{ref}	[s]	Reference time
η_c	[s]	Beam centre crossing time
$f_{\eta c}$	[Hz]	Doppler Centroid frequency
f_0	[Hz]	Sine wave frequency
I_c		Complex SLC image
μ		Mean intensity
$\hat{\sigma}$		Normalized variance
β_s		Skewness
β_k		Kurtosis
$\hat{x}(f)$		Fourier transform of image

Ocean waves:

θ	[deg]	Direction
σ	[deg]	Spreading
ω	[rad/s]	Angular Frequency
g	[m/s^2]	Gravitational acceleration
k	[1/m]	Wave number
kx	[1/m]	Wave number in x-direction
ky	[1/m]	Wave number in y-direction
d	[m]	Water depth
L	[m]	Wave length
T	[s]	Wave period
a	[m]	Wave amplitude
$Hm0$	[m]	Significant wave height
$HE10$	[m]	Swell wave height
$U10$	[m/s]	Wind speed
Δf	[Hz]	Frequency bin size
$E_{tot}(f)$	[m^2/Hz]	Variance density spectrum per frequency
$E_{tot}(\omega)$	[m^2/rad]	Variance density spectrum per radial frequency
$E_{tot}(k)$	[m^2/1/m]	Variance density spectrum per wave number
J	[m]	Jacobian
α		Fenton parameter
β		Fenton parameter
s		Spreading parameter
α_0		Mean wave direction
γ		Skewness

List of Figures

1

Introduction

1.1. Research motivation

Swell waves are a dream for surfers and a nightmare for marine traffic. Swells are wind-generated waves which originate from distant storms and have outrun their local wind field. Near the coast swell waves start shoaling; the wave height increases and the wave length decreases. Long crested swell waves with a long period are the perfect conditions for local surfers.

However, low-frequency swell waves pose large problems for marine traffic. When the wave length of a wave reaches the same size as a vessel, parametric roll resonance [24] [25] creates huge ship motions and is known to cause several incidents each year. Other problems occur when swell waves enter ports, where they create motions on moored ships. Wave conditions are also important for the construction and maintenance of offshore wind farms: wave conditions determine the weather windows for maintenance activities [64].

The North Sea is located along the coast of Northern Europe, between Scandinavia, Germany, The Netherlands, Belgium and Great Britain. The North Sea is an important water mass for marine traffic, with ports such as the Port of Rotterdam, Antwerp and Hamburg. Its shipping lanes are among the busiest in the world [8]. There is also an increased interest in the construction of large offshore wind farms in the North Sea since recent years. It becomes obvious that in order to perform marine activities safely, ocean conditions in the North Sea need to be measured using all available technology.

1.2. Ocean waves

While important for many different reasons, it is actually quite difficult to measure the full two-dimensional wave spectrum. In-situ measurements (by pitch-and-roll buoys) only measure mean direction and mean spreading per frequency, the two-dimensional wave-number spectrum can only be calculated using a spreading function [34].

Another source capable of estimating the full two-dimensional wave spectrum are wave models. Unfortunately these models have especially problems with forecasting low-frequency swell waves, which still remains the most poorly predicted part of the sea state [3] [17]. Willis et al. [67] showed extreme swell conditions after Hurricane Bill were under-predicted by a local SWAN model, leading to problems for marine traffic as well as posing a threat to public safety. Van Vledder et al. [65] summarizes the main inaccuracies in numerical models: white capping dissipation, non-linear interactions and bottom friction make accurate predictions difficult.

Earlier observations of swell movement across the earth oceans [7] were made with spectral analysis of ocean waves along the Pacific [57]. Miles [50] assumed a quasi-laminar theory to explain the growth of waves due to wind. Despite the relevance and applicability of Miles's theory, it is criticized for neglecting the effects of turbulence on the wave induced motion [10]. Although swells are known to move freely across the oceans, several processes are known to decay swell height. Among others are depth induced dissipation and the wind stress modulation that decay swell height, depending on wind speed and direction [4]. Conventional observations techniques do not adequately measure the full two dimensional wave spectrum, which stresses the importance of other observation techniques. The solution is using a state-of-the-art remote sensing technique from Sentinel-1: Synthetic Aperture Radar.

1.3. Synthetic Aperture Radar

Synthetic Aperture Radar (SAR) has been known to provide operational sea-state information for many years. Radar sensors measure wind and wave information which is used by ocean modeling forecast communities. [18]. Using SAR it is possible to retrieve the full two-dimensional swell part of the wave spectrum. Sentinel-1 is one of the most recent satellite platforms where this technique is applied. Over the open oceans, Sentinel-1 operates in Wave Mode and measures direction, propagation and dissipation of swell [39]. However, Traon et al. [62] mentions future research on SAR ocean wave imaging during extreme sea states is also wanted. Drinkwater et al. [18] mentions that other applications of swell wave data would include the assimilation of ocean data in numerical models [66] to improve operational forecasts. SAR images could provide additional information on low-frequency motions in numerical wave models as well as reduce errors in these models [14]. As Collard et al. [14] mentions, the use of SAR images for deriving ocean waves in coastal areas has been extremely limited. This brings us to the main problem of this thesis; to what extent Sentinel-1 SAR imagery are capable of sensing low-frequency swell waves in the North Sea.

1.4. Aim of this research

The objectives of this research are to increase understanding on the applicability of SAR in the North Sea and to use SAR to observe low-frequency waves. SAR imagery and retrieved wave spectra from these images, will provide additional information on the low-frequency swell waves, which could help validate model predictions. This thesis answers the following research question:

To what extent can we observe swell waves in the North Sea using Sentinel-1 Synthetic Aperture Radar?

Sub-questions that will help answering the main question are:

1. *For which conditions can the Sentinel-1 SAR observe low frequency swell waves in the North Sea?*

   The North Sea has a predominant wind-wave climate, the average wind speed lies between 4 and 16 m/s depending on season [12]. Literature showed that different hydrodynamic and meteorological conditions impact radar image quality. A higher wind speed or wave height is known to distort the SAR image trough a process called velocity bunching. It is important to know to what extent this effect occurs when observing SAR images in the North Sea.

2. *Can the ocean swell wave algorithm be applied to Interferometric Wide Swath (IW) images of the North Sea?*

   The retrieval of ocean wave spectra from SAR has been possible for several decades. One of the first derivations was by Hasselmann and Hasselmann [30] who described the SAR image spectra as a function of the underlying ocean wave field. The Sentinel-1 satellite uses a more advanced form of this derivation in its Wave Mode, which is used to derive wave spectra when operating over the open oceans. Over land and in coastal regions, the satellite operates in a different (Interferometric Wide Swath) IW-mode. It is not yet known whether the algorithm will work on this different set of radar images.

3. *Can SAR images be simulated using ocean wave spectra and can we apply the swell algorithm on simulated images?*

   The results from measuring swell waves with SAR radar images will need to be verified and validated. Since a strong wind speed and a high wave height are known to complicate the retrieval of ocean wave spectra from SAR images .One way of validating the results is by simulating radar images from wave buoy data. This is possible using OCEANSAR simulator, a tool which allows the simulation of radar images. By using a simulated SAR image, we can check if the SAR sensor is working properly and if the retrieval algorithm works. Simulated images might provide extra information, that is lost during SAR processing. We want to see what additional information a simulated SAR image is able to provide.

4. *Can we assess spatial variations in the ocean wave field using Synthetic Aperture Radar images?*

   A single Interferometric Wide Swath SAR image has a size of 250 km. The ocean swell spectral transform is applied on a smaller imagette within the SAR image. This allows us to retrieve the ocean swell spectrum at multiple locations simultaneously. With multiple ocean spectra measured from a single SAR image we can now observe whether there are spatial variations, such as differences in wave height or direction, within the ocean wave field. This could provide information on different processes, such as swell dissipation or refraction.

1.5. Outline and reader

Chapter 1 contains an introduction to the topic of SAR and waves and presents the aim of this research. Chapter 2 presents a brief introduction in radar signal processing. In Chapter 3, the materials and method are presented, including the SAR cross-spectral algorithm. The results are presented in Chapter 4 and at last in Chapter 5 and Chapter 6 the conclusions and recommendations are discussed.

2

Radar

2.1. Introduction

It is important to first understand how a radar works, before algorithms which measures ocean spectra from SAR images are discussed. Furthermore, several processes will affect the image quality and influence the retrieval of wave data. This chapter first discusses the process through which a SAR image is created and next the different processes which influence this image.

Over the past decades, several satellite missions have been launched containing a radar instrument. One of the recent missions is the Sentinel-1 (S-1) constellation, which consist of two satellites; Sentinel-1A (S-1A) and Sentinel-1B (S-1B) and has an active microwave instrument which operates at a C-band 5.405 GHz (˜5 cm) frequency [1]. both satellites are identical and operate with a 180 ° orbital phasing difference. Over the Netherlands, the S-1 mission has a repeat cycle of 6 days [61].

In the essence, a radar (Radio Detection And Ranging) consists of a transmitter, which sends a microwave signal to an object and an antenna which measures the backscatter from this object. The method of actively illuminating parts of the surface is called an active microwave remote sensing technique. Backscatter is the portion of the signal which is returned to the radar antenna, the intensity of the backscatter and time-delay to the surface (phase) are measured by the radar [21]. The strength of the backscattered signal depends on the angle of incidence, surface roughness and other properties later explained in this chapter.

Since both the intensity and phase information is needed, S-1 Single Look Complex (SLC) images are used. An SLC image contains per pixel both the intensity and phase information. This information is stored in a single imaginary number, a concept further explained in the box "Complex Imagery".

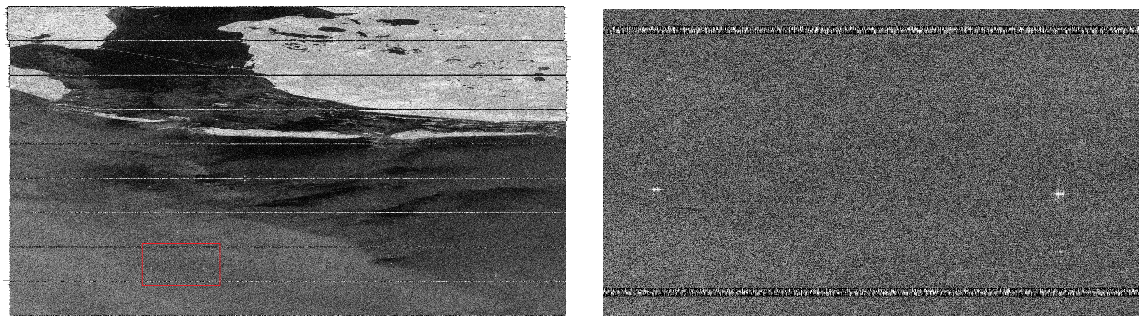

Figure 2.1: Example of a single SLC intensity image. Right shows a sub-swath of the SLC image, right shows a smaller subset with the black demarcation area between bursts.

[1] https://sentinel.esa.int/web/sentinel/technical-guides/sentinel-1-sar/sar-instrument

Complex imagery
Sentinel-1 Single Look Complex images are stored in complex notation: $slc = i + jq$, where i represents the real, in-phase part of the signal and q the complex, quadrature part. Complex numbers are often expressed in polar form: $Me^{j\phi}$, where the magnitude (or intensity) M and phase ϕ are expressed by:

$$M = |slc| = \sqrt{i^2 + q^2} \tag{2.1}$$

$$\phi = \tan^{-1}\left(\frac{q}{i}\right) \tag{2.2}$$

The magnitude is the intensity or power of the image and is measured in radar cross section normalized by unit area [m^2/m^2] and it is also often scaled to decibel, e.g. $c_{db} = 10 * 10log(slc)$. The phase represents a rotation around the Real and Imaginary axis, as shown in Figure 2.2 [2].

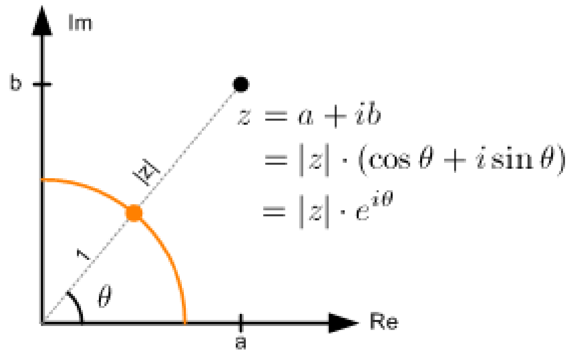

Figure 2.2: Polar form of a complex number, showing the absolute value (z) and phase (θ).

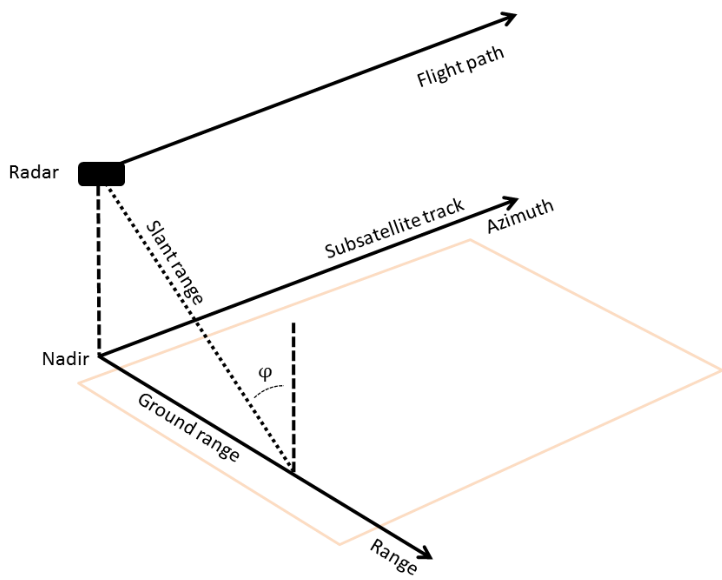

Figure 2.3: Imaging geometry for an air-borne (or space-borne) platform.

[2]http://www.songho.ca/math/euler/euler.html

2.2. Geometry

In order to understand how a SAR system operates, we first look at the measuring geometry of the satellite itself. The Sentinel-1 SAR is a side-looking radar, which is looking to the right compared to the satellite flight direction. In Figure 2.3 we can see the typical geometry for this type of side-looking platform. The radar is represented by a black box, azimuth is the direction parallel to the flight path of the satellite, range is the direction perpendicular to the flight path. The point directly beneath the satellite is called nadir. We can distinguish different distances in range direction. Slant range refers to the distance between the radar and a target on the surface. Ground range refers to the absolute horizontal distance along the earth surface corresponding to a point measured in slant range. The incidence angle θ in Figure 2.3, is the angle between a radar beam and the ground surface.

2.3. Radar

Now that the viewing geometry is established, it is time to look at Real Aperture Radar or RAR. RAR is in the essence the same as SAR, but is more easily explained. An example of a RAR system would by the side looking radar on Sentinel-3. The resolution of a radar depends on the microwave radiation and geometrical effects. An excellent example is provided by *NRCAN Fundamentals of Remote Sensing* [3].

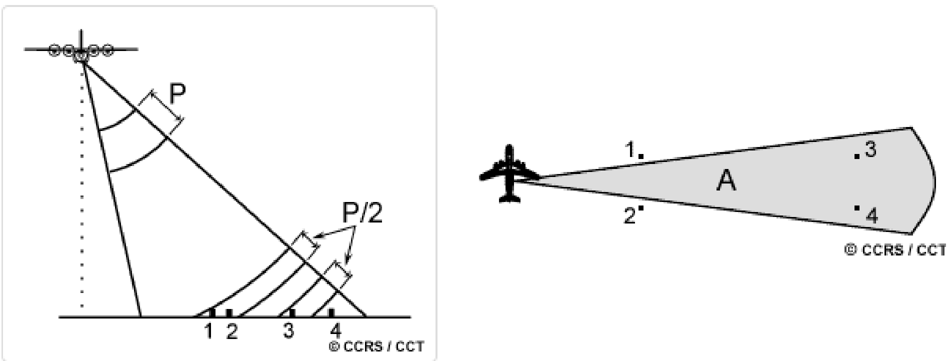

Figure 2.4: Imaging of a RAR system in range direction (left) and azimuth direction (right), showing the Pulse width (P) and the beam width (A).

In the case of a RAR, the image is formed using the transmission of a single pulse and the backscattered signal. The resolution depends in range direction on the length of the pulse and in azimuth direction on the width of the pulse beam, as shown in Figure 2.4. As we can see in Figure 2.4, the resolution in range depends on the length of the pulse (P). When the distance between two targets is greater than half of the pulse length, these two targets can be resolved. In this example target 1 and 2 will not be separable from one another, while target 3 and 4 are. Since the resolution depends on the pulse length, we observe a constant resolution in *slant range*, see Figure 2.3. The resolution in ground range is different, since it depends on the incidence angle of the satellite. The incidence angle changes with increasing range, which means the ground range resolution becomes smaller.

The azimuth resolution of a RAR sensor depends on the angular width and slant range distance of the microwave beam. In the example of Figure 2.4, the azimuth resolution becomes larger as the beam-width (A) increases. This means that target 1 and 2 would be separable from one another, while target 3 and 4 are not. The beam width of a radar is proportional to the size of the antenna. A larger antenna length (or aperture) would lead to a narrower beam and better resolution. The antenna length for space-borne platforms is limited, combined with a very long slant range distance (1000s of kilometres), this puts a restriction on the fine azimuth resolution which has to be achieved. This is where the concept of a Synthetic Aperture comes in place.

[3] http://www.nrcan.gc.ca/node/9309

2.4. Synthetic Aperture

In order to overcome the problems from a Real Aperture Radar, a special processing technique makes it possible to simulate a long antenna (and thus aperture), this is the concept of a Synthetic Aperture Radar (SAR). An example of a SAR acquisition is shown in Figure 2.5, source *NCAR*. When the satellite is at point 1, a target (A) enters the microwave beam and the backscattered signal from each pulse is recorded [48]. As the satellite moves forward, it continuously records the return signal from this target, until point 3, where the target leaves the satellite microwave beam. During this period the individual signals are combined and through signal processing a synthetic aperture is constructed [36]. The length of the Synthetic Aperture is now determined by the time the object was illuminated by the satellite beam. In the previous section we observed the resolution in azimuth *decreased* with increasing range. This effect is now *compensated* by the longer illumination time from the satellite beam. The result is a uniform, fine resolution in azimuth direction.

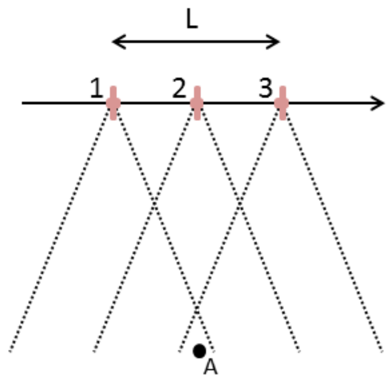

Figure 2.5: SAR processing).

2.5. TOPSAR

Although SAR is the conventional technique which is used by space-borne platforms to create a radar image, several modes exist to further enhance the image quality. For the Sentinel-1 mission this is the TOPSAR mode, which was first developed by De Zan and Monti Guarnieri [16]. Typical for the TOPSAR mode is steering of the SAR antenna in azimuth direction during the acquisition of a radar image, this process can be seen in Figure 2.6. Due to the steering of the antenna problems with scalloping and azimuth varying ambiguities are avoided [49], the result of TOPSAR is a nearly uniform Signal-to-Noise Ratio (SNR) and Distributed Target Ambiguity Ratio (DTAR). One of the side effects of steering of the antenna is the introduction of an additional antenna pattern. This antenna pattern needs te be removed, before it is possible to further process TOPSAR radar images. The removal of this antenna pattern is called *deramping* [54] and is further explained in Chapter 3.

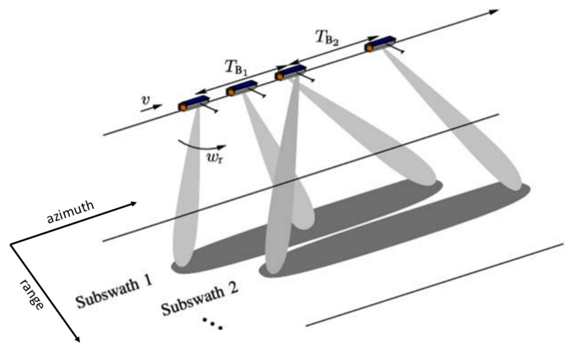

Figure 2.6: Acquisition geometry of the TOPSAR imaging mode where ω_r is the steering rate of the antenna, v the velocity of the satellite and T_{B1} measurement time, see Meta et al. [49]

2.6. Resolution

From the previous section we found that different processes determine the resolution in azimuth and range direction. We are now going to see how this is applied in practice for the S-1 satellites. The azimuth resolution Δa is determined by length of the synthetic aperture L_{sa}, where:

$$\Delta a = \frac{L_{sa}}{2} \tag{2.3}$$

And the length of the aperture is equivalent to the distance travelled by the platform during the acquisition time of the radar image.

The resolution of the radar in slant range depends on the pulse length (P). We can also express the length of the pulse in terms of the pulse frequency or bandwidth. We can now define the range resolution Δr with the pulse bandwidth β and the speed of light c , which is calculated with Equation 2.4 [36]. Sentinel-1 operates in IW mode with a chirp bandwidth between 56.50 and 42.80 MHz. Using Equation 2.4 this would result in a range resolution of 2.65 to 3.5 m.

$$\Delta r = \frac{c}{2\beta} \tag{2.4}$$

The range resolution is also affected by slant-range scale distortion, which warps the image due to the view angle of the radar. This effect occurs due to the fact that the radar is measuring the distance to features in slant range, as opposed to the true horizontal distance, an example of this effect is given in Figure 2.7.

The ground range geometry can be calculated using:

$$\Delta r_{grd} = \Delta r(1/\sin\theta) \tag{2.5}$$

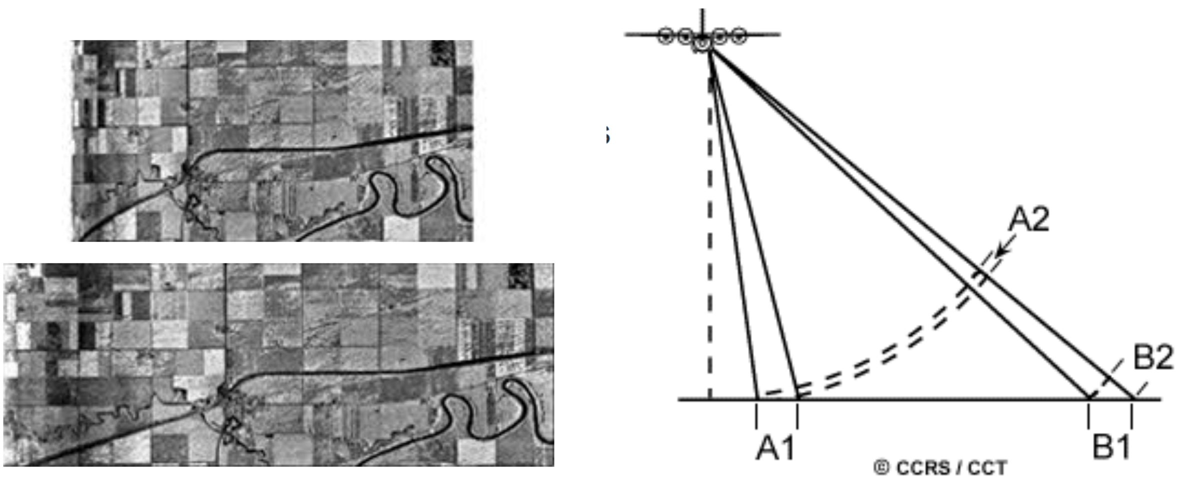

Figure 2.7: Effect of the slant range geometry. In the left figure, the top image is folded, this is a result of the look angle, which is shown on the figure on the right. With a constant spacing of an area, the measured area A2 is smaller than B2 (copyright: CCRS/ CCT).

Now that we have discussed the imaging geometry of a SAR system, the method through which a SAR image is constructed, it is time to look at image distortions. Unfortunately a radar image is not 'perfect', several processes distort the radar image and affect the radar backscatter. This will be the topic of the next section.

2.7. Radar image distortions

A radar image is affected by a number of processes which affect the returned backscatter; speckle, the surface roughness, local incidence angle, corner reflections, antenna patterns, moisture and the radar polarization. In this section we look at these different processes, which will help understanding the different processes seen on radar images.

Speckle Speckle is the grainy "salt and pepper" interference present at SAR images. It is caused by constructive and destructive interference of the radar. It results from differences of radiometric backscatter within a resolution cell. As an example, a single grain of grass provides a different scatter compared to a field of grass, which results in differences. Processing filters, such as Refined Lee [44] and multi-looking provide options to reduce the amount of speckle.

Surface roughness The amount of radiometric backscatter is depends on how smooth or rough a surface is. When the surface is smooth, incident energy is reflected away from the sensor and only a small amount returned to the radar. A rough surface scatters the incident energy in all directions and a large proportion is returned to the antenna.

Incidence angle The angle of the direction of the platform with the surface also plays an important role. Two factors play a role, the local incidence angle, which is the angle between the beam from the platform and the local surface and the angle between the flight direction and measured geometries. A steeper angle will result in a stronger backscatter, whereas the surface will appear smoother when the angle of incidence increases.

Corner reflector A corner reflector is typically an object with a smooth surface and consists of several corners. The corners reflect the incident radiation, through a double bounce and a very large portion is reflected back. Small corner reflectors are often present on marine platforms, such as ships and buoys, but are also present in city centres, where incident energy is reflected by buildings.

Antenna pattern SAR images typically show a stronger return in the centre portion of a swath, an effect known as the antenna pattern. Combined with the fact that SAR images show decreasing return energy with increasing range distance, result in an image with varying intensity across the range. In post processing it is possible to apply a correction for this difference in brightness.

Polarization The polarization of the radar refers to the orientation of the electric field, being either Horizontally (H) or Vertically (V) oriented. Sentinel-1 SLC images are available in both VV polarization (vertical transmit, vertical receive) and VH polarization (vertical transmit, horizontal receive). VV images typically show stronger backscatter [21], [48], which makes wave detection easier and is therefore used during this thesis.

Other effects, such as relief displacement and lay over shadows also affect the creation of a SAR image in mountainous areas, this is thought to play a minor role over the oceans On land other processes which affect the backscatter is the moisture of the land.

2.8. Imaging of the ocean

The concept through which ocean waves are observed by radars is fairly well understood [32] and has been studied for several decades. This section discusses the processes which influence the imaging of the ocean using SAR. When a radar wave is sent to the surface of the ocean, the main mechanism which influences the radiometric backscatter is resonant Bragg scattering, as schematized in Figure 2.8 .

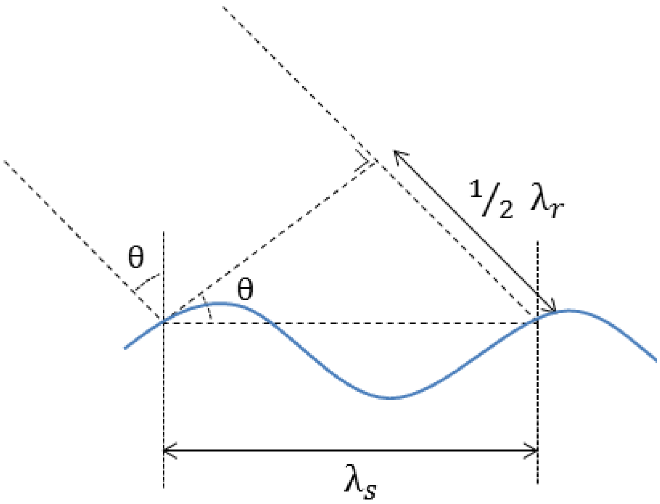

Figure 2.8: Schematization of Bragg scattering. When the wave length of the radiation is about half the wave length of the Bragg waves, a strong backscatter is returned.

Bragg scattering occurs when structures on the ocean surface have the same length as the wavelength from the radar and is a function of the incidence angle and the wave length of the transmitted radar.

$$\lambda_s = \frac{\lambda_r}{2sin(\theta)} \tag{2.6}$$

With:

λ_r	[m]	radar wavelength
λ_s	[m]	sea surface wavelength
θ	deg	incidence angle

Ocean structures which cause Bragg scattering are the small ripples generated by wind. These gravity-capillary waves have a wave length (~10 cm) which falls in the same range as the wave length of the S-1 C-band radar (~ 6 cm). While Bragg scattering is the main source of scattering for the oceans, the Bragg scattered energy is influenced by longer ocean waves. This interaction between the capillary Bragg waves and longer gravity waves is the so called modulation [37], a concept also known as the two-scale approximation Jackson and Apel [36].

Attempts to write down this modulation using analytical expressions were first done by Hasselmann and Hasselmann [30] and Jacobsen and Høgda [37]. This expression, which transfers information of the ocean using a SAR point of view is also known as the Modulation Transfer Function (MTF). Because of the different imaging mechanisms in range and azimuth direction, both a RAR and a SAR MTF exist. The three main processes which influence the modulation of Bragg scatterers are *tilt modulation*, *hydrodynamic modulation* and *velocity bunching* these effects are further explained below. Other oceanic processes which are not further explained but also affect the Bragg scattering, are currents, eddies and internal waves.

Tilt modulation Tilt modulation is caused by a change in local incidence angle due to the passing of a longer wave, see Figure 2.9. When a long wave passes a field of short Bragg waves the tilt (slope) of the longer wave affects the returned backscatter. The long waves change the orientation of the short Bragg waves which changes the returned intensity of the scatter [37].

Hydrodynamic modulation Hydrodynamic modulation is a result of the motion of individual fluid particles within a wave, also known as orbital velocities. At some locations along a long wave, individual fluid particles tend to move towards each other (compression), while at other locations they diverge, as shown in Figure 2.9. A process comparable to the movement of an accordion. Areas where the fluid particles are compressed show an increase in Bragg scattering, while areas which diverge, show a decrease in scattering. Convergence typically happens at the waves crest, while divergence happens at the through. Both tilt and hydrodynamic modulation show the strongest effect when the surface gravity waves are travelling in range direction, perpendicular to the flight direction of the platform [11].

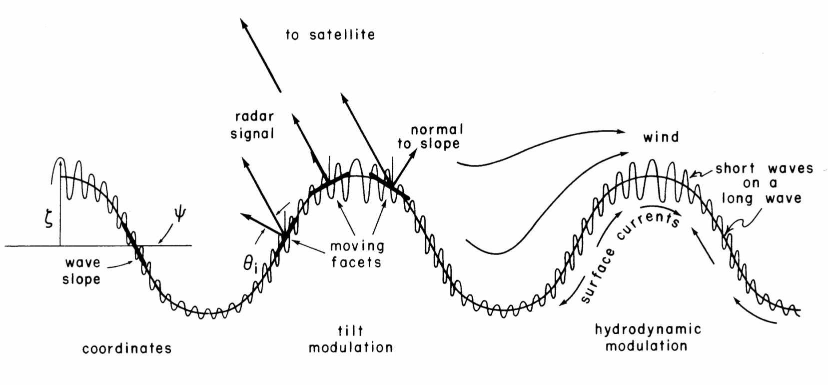

Figure 2.9: Tilt and Hydrodynamic modulation. Longer waves change the orientation or slope with the platform, while hydrodynamic modulation distributes energy of the shorter wave field. Symbols include local incidence angle, θ , wave-number spectrum ψ and sea surface elevation ζ. [after Stewart 1985] [36].

Velocity bunching Velocity bunching is an effect which occurs due to the relative motion of waves, compared to the motion of the satellite. In the ideal case the SAR imaging process assumes a stationary surface, when observing ocean waves a stationary scene is obviously not possible. Velocity bunching is described as an apparent bunching (increase) and decrease in the intensity of the backscatter when waves are moving in azimuth (along track) direction due to the wave orbital velocities [37]. Although Alpers [1] was one of the first to observe this a shifts the peak of the SAR image spectrum as a result of velocity bunching, Hasselmann and Hasselmann [30] was the first to derive a closed derivation for the non-linear ocean-SAR spectral transformation. The velocity bunching effect can result in a highly non-linear transformation of wave patterns into an image, which means the spectrum of the image has different shape from the ocean wave spectrum [5].

Azimuth cut-off As we saw in the previous paragraph, movement of waves in azimuth direction results in a constructive mechanism called velocity bunching which locally increases the radiometric backscatter. However, the SAR measures a scene during a certain integration time, when ocean waves are moving during this integration time there is a higher chance of misregistrations [40]. This loss of resolution in azimuth direction, caused by the short SAR acquisition time puts a limit on the maximum observable wave length , known as the azimuth cut-off wave length ([38], [41]). The azimuth cut-off λ_c depends on random motions of the ocean, which in advance are related to the wind speed U, wave height Hs and development of the sea state [27]. The function between the azimuth cut-off and the sea state is known and empirical relations which relate wind speed and wave height to the azimuth cut-off wave length, are established for Sentinel-1 [35] Shao et al. [56]. Using the SAR image cross-spectra it is possible to estimate the azimuth cut-off wave length, which is further explained in Chapter 3.

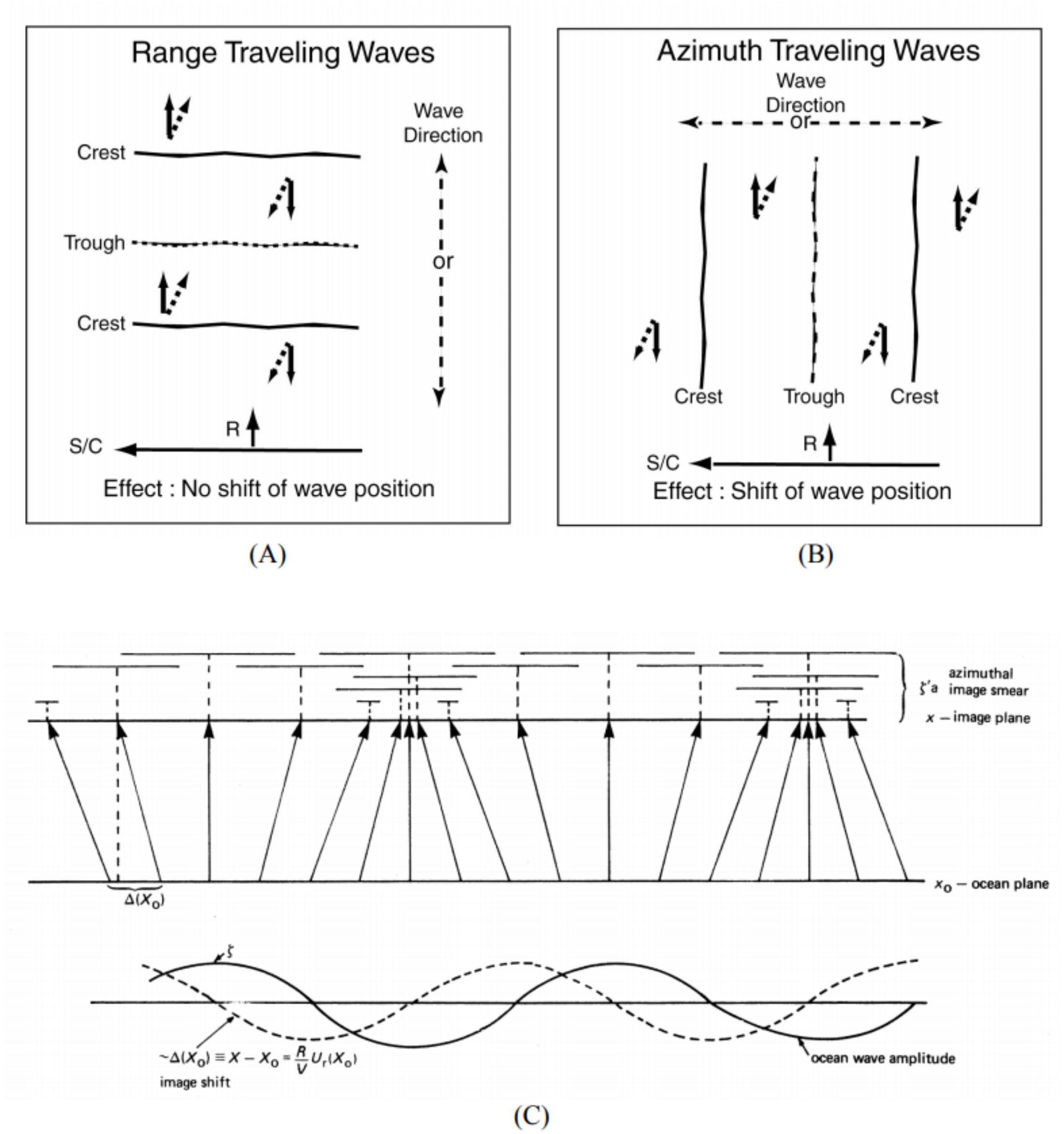

Figure 2.10: A) shows range travelling waves and B) azimuth travelling waves. C) shows the related shift and bunching when waves travel in azimuth direction

3

Materials and Method

In this chapter the materials and method are presented. The materials consist of different sources of data, measurement devices, but also computer software used during this thesis. The second section, Method, explains how this data and software was used to achieve our results. The appendixes provide additional information on the data and algorithms which are used.

3.1. Materials

This chapter covers the materials used during this thesis, which is composed of different sources of data, computer software and programming modules. Most of the processing of data was performed in Python. The resulting python scripts can be found on-line or are available on request.

3.1.1. Buoy data

The reason to use wave buoy data was: (i) to select SAR data with certain hydrodynamic conditions, (ii) to validate the results of our method and (iii) as input to simulate SAR images. Since we are interested in the spatial distribution of ocean waves 2D spectra are used. 2D spectra are characterized by a value for the energy density, direction θ and spreading σ, after one can recreate the 2D spectrum using a spreading function. In the North Sea, the K13 Alpha, Platform A12 and IJgeul munitiestort buoy provide 2D spectral information and were subsequently used during this research. Figure 3.1 indicates the location of these three buoys, the data was provided by Rijkswaterstaat (RWS).

Additionally wave buoy data along the Portuguese coast, near Nazaré, was used. Portugal was selected as a validation study to test of the proposed methodology works. The coast of Portugal and more specifically Nazaré is famous for their exceptionally large swell waves with long wave lengths [15], which would be easier to detect by SAR compared to the smaller North Sea swell waves. Figure 3.1 indicates the location of the Monican 1 and Monican 2 wave buoys, both situated along the Portuguese coast. While both wave buoys are indicated on this figure, only wave data from the Monican 1 buoy was used during this research due to the more off shore position. Wave buoy data from Portugal was provided by Instituto Hidrográfico. An overview of the Portuguese, as well as the North Sea wave buoys, is provided in Appendix A.

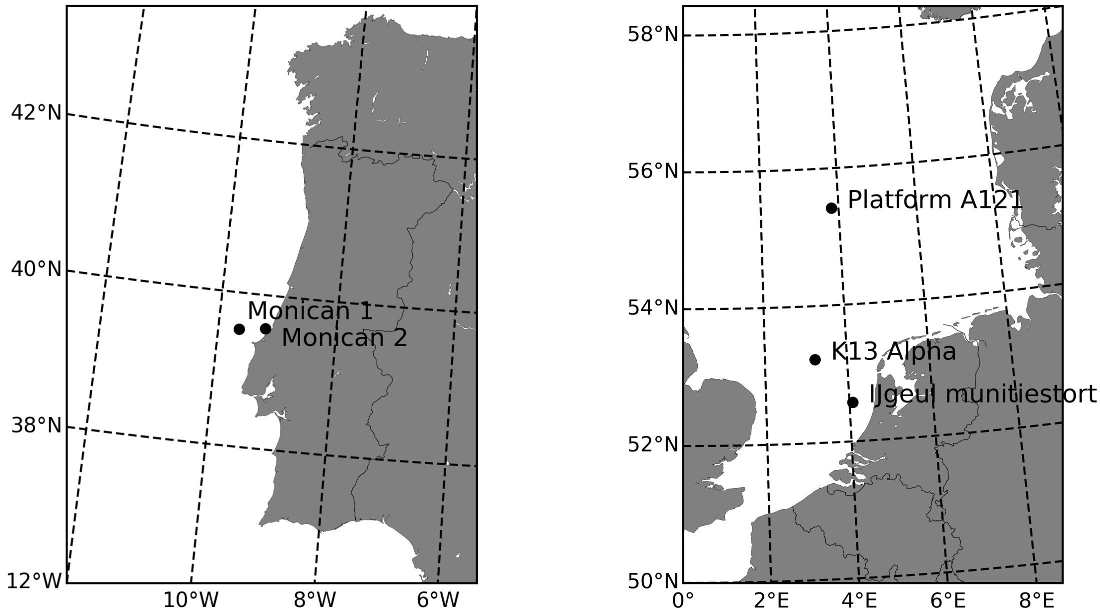

Figure 3.1: Wave buoy locations near the Portuguese coast (left) and in the North Sea (right).

3.1.2. SAR data

As mentioned in the previous Chapter, Sentinel-1 SLC IW images with VV polarization are used during this thesis, with a 2.3 m by 13 m resolution in slant range. Single Look Complex, since we need both the intensity as well as the phase information, which is stored in complex notation. Interferometric Wide Swath mode, since this is the main operating mode of Sentinel-1 over the North Sea and Portugal and VV polarization due to the increased backscatter of the signal over oceans.

Sentinel-1 has an overpass repeat cycle of 6 days, which means for both locations, several hundreds of S-1 SAR images are available. It is not efficient to analyze all the radar images, which meant a selection is made from this dataset. Three SAR images for the Portugal coast where selected randomly as long as they showed clear lines of increased backscatter on the SAR intensity image. SAR images from the North Sea where selected by analyzing a time series of wave data at the K13 buoy.

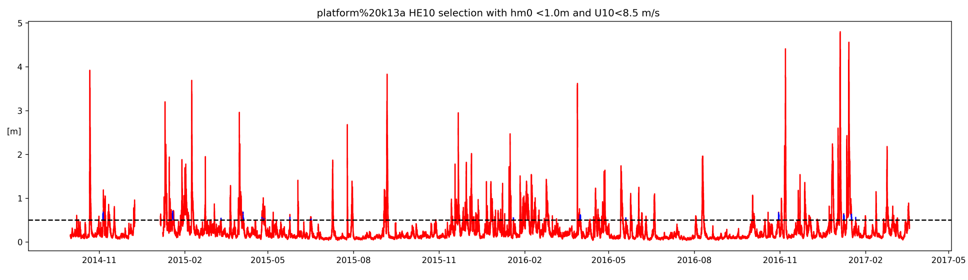

Figure 3.2: Swell HE10 wave height with selected events in blue, corresponding to an azimuth cut-off wave length of 135 m at the K13 alpha buoy.

What determines if it is possible to observe a wave with radar, is the wave length of the waves. The radar has a fixed resolution, so when the wave length becomes too small, individual wave crests will no longer be observable from one another. The wave length depends on the water depth and wave period and can de described using the dispersion relation Equation A.12. Figure 3.3 shows how the wave length decreases when waves travel from deep water (off-shore) to shallow water (near-shore), lines are plotted for different wave periods.

$$\omega^2 = gk\tanh(kd) \quad \text{or} \quad L = \frac{gT^2}{2\pi}\tanh\left(\frac{2\pi d}{L}\right) \tag{3.1}$$

with:

ω	[rad/s]	Angular Frequency
g	[m/s^2]	Gravitational acceleration
k	[1/m]	Wave number
d	[m]	Water depth
L	[m]	Wave length
T	[s]	Wave period

From the previous Chapter we also found that the SAR has a limit in waves detectable in azimuth direction due to velocity bunching effect, this limit is called the azimuth cut-off wave length. This cut off wave length depends on the significant wave height and wind speed. The function between the azimuth cut-off, significant wave height and wind speed is described in Johnson and Collard [39] [35] and a graph of this relation is shown in Figure 3.3.

As mentioned in the introduction, the interest of this thesis is the low-frequency part of the ocean spectrum, which was described as waves with a period longer than 10 seconds. From Figure 3.3 (left), we see that waves with a period of 10 seconds at a water depth of 20 m have a wave length of approximately 130 m. We can now see for which hydrodynamic conditions an azimuth cut-off wave length of 130 m is found in Figure 3.3 (right). for this specific cut-off wave length we find a linear relation with a significant wave height between $0.7m < Hm0 < 1.2m$ and a wind speed between $0.5m/s < U10 < 9m/s$.

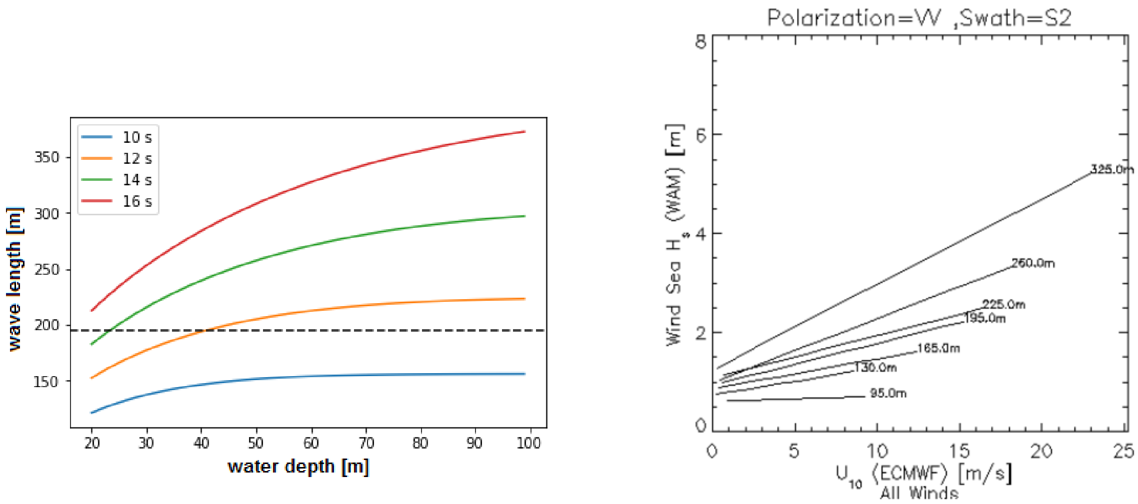

Figure 3.3: Left image shows water depth over wave length for different wave periods. Dashed line shows an azimuth cut-off wave length of 195 m. The right image shows the empirical relation between the azimuth cut-off wave length, wave height and wind speed [35] [39].

In Figure 3.2 we can see the results of a time series analysis using this information using data from the K13 buoy. When $HE10 < 0.5m$, $Hm0 < 1.0m$ and $U_{10} < 8.5m/s$ a *'swell event'* was created, indicated in blue on Figure 3.2 .

The final step was a check to see if a satellite image was available during the *'swell events'*. This check was performed using the Python based 'sentinelsat' package. This package uses a GeoJSON object, which describes a geographic area to see if there is a satellite image available in this area. A GeoJSON object was constructed around the K13 buoy (see Appendix A), and when a satellite image was available within 24 hours of a *'swell events'* and was positioned within the geographic area, it was selected as suitable for this thesis.

The result was a list of 11 SAR images over the North Sea, which met the proposed criteria. A list of these images is presented in Appendix A.

3.1.3. Copernicus Open Access Hub

S-1 SAR images are downloaded from the Copernicus Open Access Hub [1], which is an ESA maintained website and allows access to Sentinel products. The website was accessed using the Python module '*sentinelsat*', the SAR images are downloaded using a list of satellite products, which is available in Appendix A.

3.1.4. SNAP

SNAP (Sentinel Application Platform) is an open source architecture developed under ESA contracts, for the scientific exploitation of Sentinel satellite data [68]. SNAP was used during this research to visualize SLC intensity images. For example Figure 2.1 was created using SNAP. SNAP has a Toolbox (S1TBX) with several built-in features to processing Sentinel-1 SAR data, the S1TBX contains tools to filter, geo-reference and batch process level-1 data. However, this thesis uses a specific processing scheme which was not available in SNAP, combined with the increased data volume of the Sentinel-1 mission compared to previous missions [52], it was decided to process the data in Python.

3.1.5. OCEANSAR

OCEANSAR [2], previously known as OASIS: Ocean ATI-SAR SImulator [9], is a Python-based package which simulates SAR images over the oceans. It contains routines to calculate time-varying (Lagrangian) ocean surfaces by applying linear wave theory and calculates directional wave spectra. OCEANSAR uses spectral wave data as input to simulate backscattering of the ocean surface resulting in a SAR image of the ocean [47].One of the applications of a SAR simulator is performance evaluation of SAR instruments [9].

[1] https://scihub.copernicus.eu/
[2] https://github.com/pakodekker/oceansar

3.2. Method

An overview of the method used during this research is found in Figure 3.4. The figure shows how the three different sources of data are used. The final result of this method is to derive ocean wave spectra from SAR images and compare this results with buoy measurements. The method consists of a pre-processing step, a processing step and a validation part.

1. **Pre-processing:** Calibration, deramping and demodulation of S-1 SAR images.
2. **Processing:** Retrieving cross-spectra from SAR data.
3. **Validation:** Comparing the different cross-spectra with wave buoy spectra.

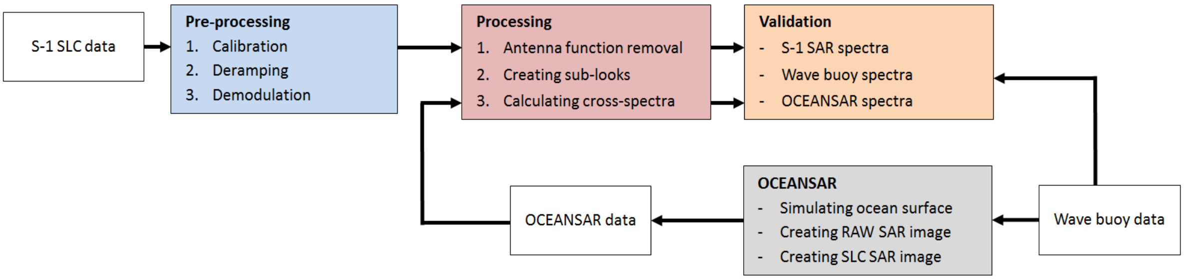

Figure 3.4: An overview of the method used during this thesis. White boxes indicate input of data. Colored boxes indicate different parts of the method.

3.2.1. Pre-processing

Before we can calculate the cross-spectrum from Sentinel-1 SAR images, there are several pre-processing steps which need to be performed. Please note that these steps are only necessary for the Sentinel-1 data and not for the OCEANSAR data. Pre-processing of the S-1 data consists of three steps: calibration, deramping and demodulation of the data, as shown in Figure 3.5 . How each of these processing steps are performed is explained in this section. The implementation of these steps can be found in the Python script *preprocessing.py*.

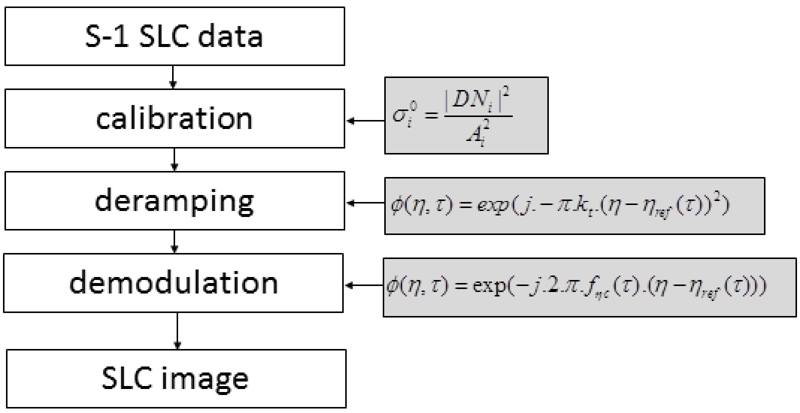

Figure 3.5: Different steps performed during pre-processing of the Sentinel-1 data. The mathematical description of each step is indicated in gray.

Calibration
Calibration of a SAR image is the conversion of pixel values (also known as Digital Numbers), to radiometric backscatter. Without calibration, the interpretation of a radar image is meaningless. Calibration is performed using an area from which the radiometric backscatter is known: a rain-forest , for example, has a specific radiometric backscatter. Using these known value's it is possible to calibrate the radar image. The information to calibrate radar images is provided in several Look-Up Tables (LUTs), which are included in the Sentinel-1 SLC products. Bi-linear interpolation is applied on pixels which fall in between the points in the LUT. The LUTs apply a range-dependent gain including the absolute calibration constant [22].

The radiometric calibration is applied using the following equation:

$$\sigma_i^0 = \frac{|DN_i|^2}{A_i^2} \tag{3.2}$$

with:

σ_i^0	[-]	Radiometric backscatter
A_i	[-]	SigmaNought(i)
DN_i	[-]	Digital Number

During the first steps, calibration of S-1 SLC data was performed using SNAP, however this led to significant memory usage and calibration using SNAP took a significant amount of time. To overcome these two problems, calibration was implemented in Python. The S-1 SLC product was loaded in Python using the OSgeo GDAL library and the SLC image was constructed by combining the in-phase and quadrature part. Calibration was performed using Equation 3.2, where Digital Numbers are pixel values from the original SLC image and sigmaNought(i) are calibration constants provided by the LUT. The phase information from the SLC image is preserved, which means the new, calibrated SLC image is constructed using: $slc_{cal} = \sqrt{\sigma^0} * e^{i\theta}$, with phase values θ from the original SLC image. The array contains data from a single sub-swath of an SLC image and is stored on the drive for further processing steps. In Figure 3.6 a comparison between calibration in SNAP and using Python is shown, as also discussed on the Step forum [3]. Table 3.1 shows the computed image statistics from calibration in Python and SNAP.

	Mean	**Variance**	**Skewness**	**Kurtosis**
SNAP:	0.0178287786	1.326905989	657.559826	4023.84215
Python:	0.0178286673	1.326906561	657.562957	4023.85589

Table 3.1: Computed image statistics of calibration performed using Python and SNAP.

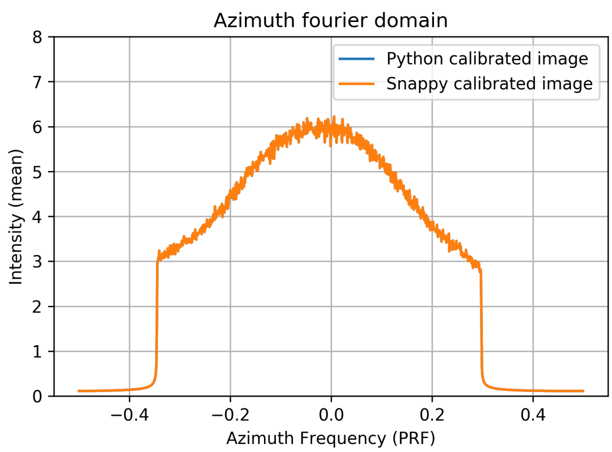

Figure 3.6: Comparison of the azimuth Fourier domain between a SAR image calibrated using SNAP and a Python implementation. There are small differences between the two calibration methods , however they are not visible.

[3]http://forum.step.esa.int/t/snappy-error-memory-is-cached/7066/5

Deramping

As mentioned in chapter 2, Sentinel-1 SLC images during IW mode are captured using TOPSAR. Characteristic for TOPSAR is electronic steering of the satellite antenna in azimuth direction. As a result an additional antenna pattern is observed in the data [26] which is mathematically described as a a quadratic phase term. The process of removing this antenna pattern is called *deramping*. An algorithm which describes the process of deramping Sentinel-1 data is described by Miranda [51]. In Figure 3.7 we see an example of an SLC image with and without deramping. The middle image shows the Time/Frequency Domain (TFD) and the pattern resulting from steering of the antenna. The right image shows the TFD after deramping, where the data is no longer shifted. Further in the section is explained how signal processing in the Frequency domain works.

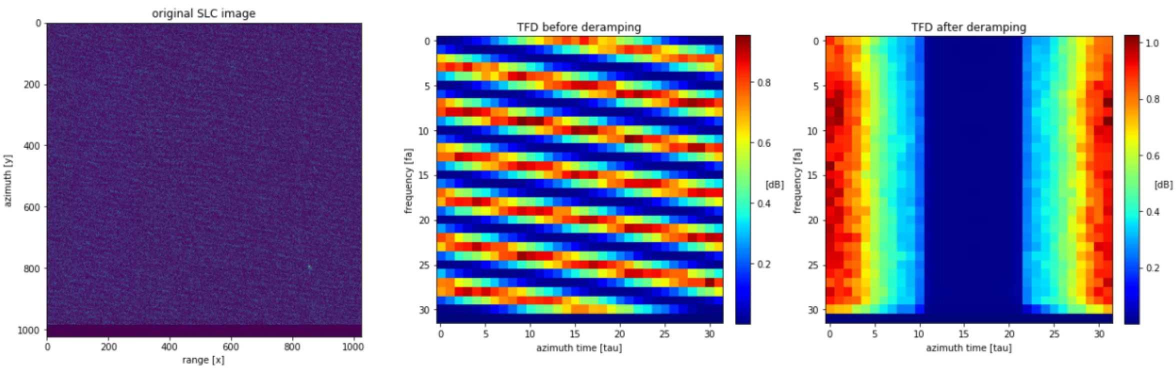

Figure 3.7: Time/Frequency Domain before and after deramping

Deramping of the SAR images was performed in Python and an implementation of the algorithm is found in the Python script *preprocessing.py*. The information needed for deramping was read from the annotation file of the SLC products. In the next part of the section we will discus the different parts of the deramping algorithm and the mathematical expressions which describe this process. A simplistic version is provided in this section, for the complete overview of the deramping algorithm we would refer to [26] and [51].

The spectral components of the SLC are moved to low-pass band (deramped) by a multiplication in azimuth time domain with a chirp signal defined as:

$$\phi(\eta,\tau) = exp(j.-\pi.k_t.(\eta-\eta_{ref}(\tau))^2) \tag{3.3}$$

with:

$\phi(\eta,\tau)$	[-]	deramping phase term
k_t	[Hz/s]	Doppler centroid rate in the focused TOPS SLC data
τ	[s]	range time
η	[s]	azimuth time
η_{ref}	[s]	Reference azimuth time

where k_t is defined as following:

$$k_t(\tau) = \frac{k_a(\tau).k_s}{k_a(\tau)-k_s} = \frac{k_s}{\alpha} \tag{3.4}$$

with:

k_a	[Hz/s]	Doppler FM rate
k_s	[Hz/s]	Doppler Centroid rate introduced by the scanning of the antenna k_Ψ [Hz/s]
k_Ψ	[rad/s]	Antenna Steering rate
α	[-]	Conversion factor for scaling the raw time rate

kt is obtained by scaling the RAW time rate (ks) with the conversion factor (α) between focused and raw time such that:

$$\alpha = 1 - \frac{k_s}{k_a(\tau)} \tag{3.5}$$

ka is the classical azimuth FM rate which is always negative. The azimuth FM rate is provided as a sequence of range polynomial regularly updated with azimuth time η. For deramping the ith burst, it is recommended to use closest polynomial to η_{mid} of the ith burst. The Doppler rate introduced by the antenna steering is given by:

$$k_s \approx \frac{2v_s}{\lambda} \tag{3.6}$$

with:

k_s	[Hz/s]	Doppler Centroid rate introduced by the scanning of the antenna
v_s	[m/s]	Satellite velocity computed at mid-burst time η_{mid} by interpolation
η_{mid}	[s]	Mid burst zero Doppler azimuth time
λ	[m]	radar wavelength

η is the zero-Doppler azimuth time interval centered in the middle of the burst, i.e.

$$\eta = \left[-\frac{NL_{burst}}{2}\Delta t_s, \frac{NL_{burst}}{2}\Delta t_s\right] \tag{3.7}$$

with:

η	[s]	zero Doppler azimuth time
NL_{burst}	[-]	Number of lines within a burst (same for all burst)
Δt_s	[s]	Azimuth Time interval between two SLC lines

The reference time is given by:

$$\eta_{ref}(\tau) = \eta_c(\tau) - \eta c(0) \tag{3.8}$$

and:

$$\eta_c(\tau) = \frac{f_{\eta c}(\tau)}{k_a(\tau)} \tag{3.9}$$

with:

η_{ref}	[s]	Reference time
η_c	[s]	Beam centre crossing time
$f_{\eta c}$	[Hz]	Doppler Centroid frequency

The deramped SLC image is constructed using the phase term ϕ from Equation 3.3 with the following expression:

$$slc_{deramped} = slc_{original} \quad e^{i\phi} \tag{3.10}$$

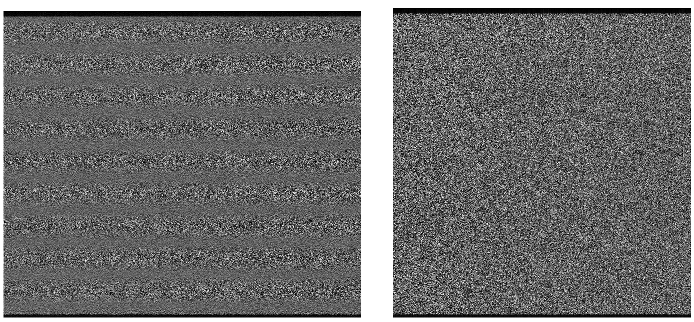

Figure 3.8: The left image shows the imaginary part of an calibrated SLC image. The middle image shows the same image after deramping is applied. The right image shows the phase which was applied to deramp the image.

Demodulation
Demodulation is defined as the process by which the original information bearing signal, i.e. the modulation is extracted from the incoming overall received signal. During the pre-processing of the S-1 SLC data, demodulation was removing the frequency shift from the deramped SLC images. In Figure 3.9 we see the mean frequency spectrum over azimuth. The peak of the spectrum is not centered around the '*zero*' frequency, but the Doppler centroid frequency. After demodulation, the peak of the spectrum would be shifted so it is centered around the zero Doppler frequency.

We can apply demodulation is applied, by adding an additional term to the function was which previously used for deramping, Equation 3.3 :

$$\phi(\eta,\tau) = exp(j.-\pi.k_t.(\eta-\eta_{ref}(\tau))^2 - j.2.\pi.f_{\eta c}(\tau).(\eta-\eta_{ref}(\tau))) \tag{3.11}$$

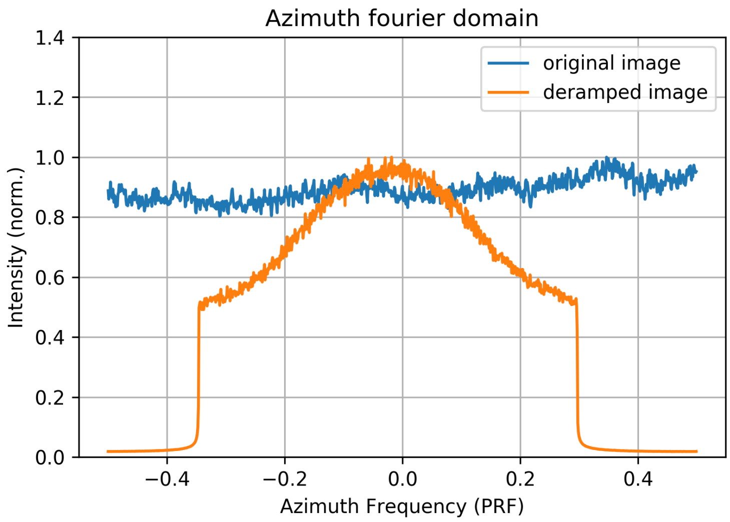

Figure 3.9: Azimuth Fourier domain, resulting from a Fast Fourier Transform in the azimuth direction. Here the mean azimuth profile is shown across range before and after deramping.

3.2.2. Processing

The main part of processing the SAR data is calculating the ocean wave spectrum from SAR images. For Sentinel-1 this is operationally done when the Satellite flies over the open oceans and operates in Wave Mode. For this specific mode, an algorithm was developed to compute the ocean spectrum from SAR imagettes. This algorithm, also known as the S-1 Ocean Swell Algorithm (OSW) is described in Johnson and Collard [39] and is partially implemented during this thesis. For more information on the complete process of SAR imaging ocean waves we refer to [11] and [21].

The algorithm consists of two steps: 1) splitting a SAR image in multiple sub-looks and calculating the cross-spectrum between different looks and 2) calculate the ocean wave spectrum from the SAR cross-spectrum using the Modulation Transfer Function (MTF), both steps will be further explained in the next paragraph. It was partially implemented, in the sense that only the first part was done during this research, Figure 3.10 shows the processing steps.

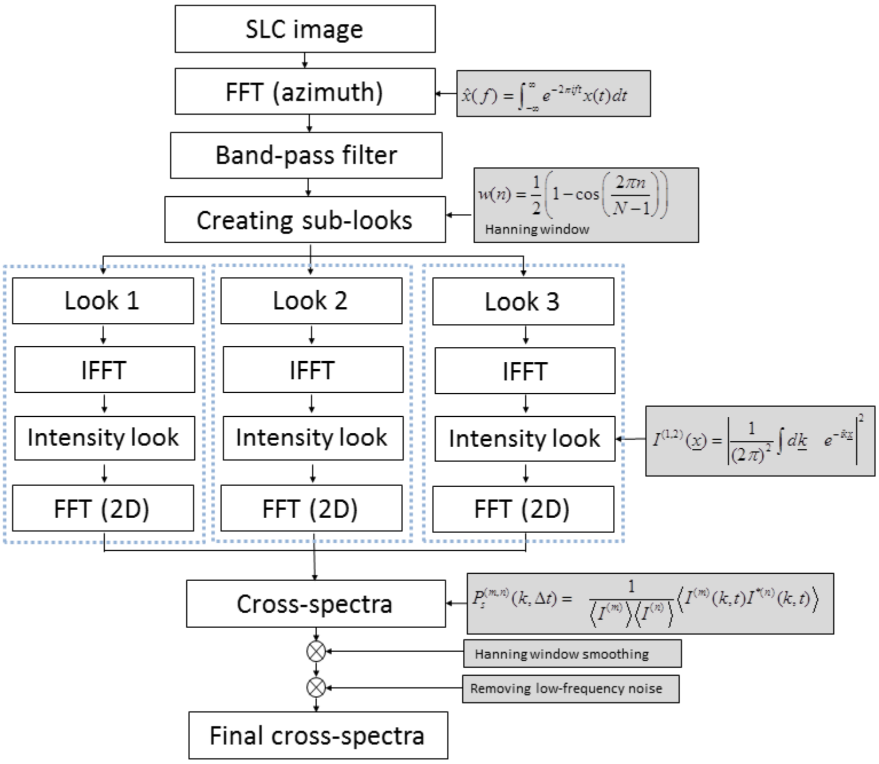

Figure 3.10: A schematic overview of the different processing steps, showing how a single SLC imagette is processed and cross-spectra are calculated.

Step 1: *Calculating the cross-spectrum*
The main step from this part of the algorithm is splitting an image in multiple sub-looks which are separated in time and calculating the cross-spectrum between these sub-looks. The cross-spectral method was first introduced by Engen and Johnsen [20], the major advantage of this method is that it allows us to determine the direction of the waves. An example of how this works is visualized in Figure 3.11. This figure shows the top view (2D) of an ocean surface. In this hypothetical example we have deep water ans swell waves with a 12 s period (0.083 Hz frequency) and a wave length (L) of approximately 210 m. The direction of the waves is not known, the waves could either be coming from the North-West or the South-East direction. A result of this ambiguity, is when the image spectrum is computed, two *positive* peaks will be observed: a peak at +0.083 Hz and a second peak at -0.083 Hz. This problem is known as the 180 ° ambiguity.

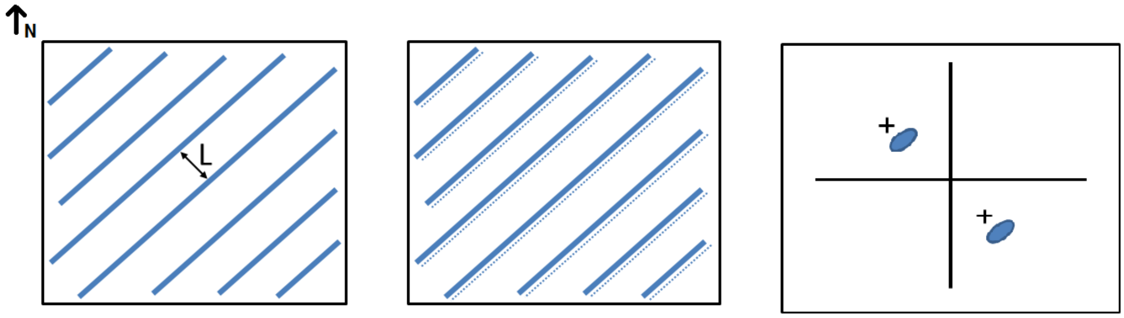

Figure 3.11: Top view of the ocean surface, where blue lines indicate wave crests of swell waves, dashed lines are swell waves from a different sub-look a small time frame later. The right image shows a schematic cross-spectrum which would result from this image.

The way the SAR sensors records a radar image allows us to solve this 180 ° ambiguity. A single SAR image is recorded in several seconds time. Since we are talking of several seconds, it means that during the acquisition of a single SAR image, the waves on the ocean surface will have moved. What we now are going to do is using this aspect of SAR to our advantage. Using some processing techniques we can split a single SAR image in multiple sub-looks, each separated in time. This is illustrated in Figure 3.11, where the blue dashed lines indicate the location of swell waves a short time-step later. When we now calculate the cross-spectrum between these two looks, we can again observe two peaks: a peak at +0.083 Hz and a second peak at -0.083 Hz. The major difference now is that one peak will be *positive*, while the second peak is *negative*. This difference is caused by a phase-shift, induced by the movement of the waves on the ocean. The positive peak indicates the direction where the waves are heading to, hence we have solved the 180 ° ambiguity. ESA [21] mentions, using the cross-spectra method the use of an a priori spectrum is no longer needed. However a limitation of this method is poor azimuth resolution and limited knowledge of the behavior of the transfer function for various sea and wind conditions. The process of splitting an image in sub-looks and calculating the cross-spectra will be explained in more detail in the sections below.

Step 2: *Calculating the ocean wave spectrum*
The previous chapter introduced the different modulations which affect the imaging process of the ocean surface using SAR: velocity bunching, tilt modulation and hydrodynamic modulation. These different modulations are described with the Modulation Transfer Function (MTF). The first closed formulation of the MTF was provided by Hasselmann and Hasselmann [30] in their seminal paper which was later reformulated by Krogstad et al. [41] [42]. The MTF describes how the radiometric backscatter, resulting from capillary waves, is modulated by the longer waves and other processes. With this expression it becomes possible to relate a SAR image spectrum to the ocean wave spectrum.

In [39] we can see how this step of calculating the ocean wave spectrum is performed for the Sentinel-1 Wave Mode. This part of the algorithm (also known as the Spectral Inversion Unit) was found to depend on external auxiliary data, such as ECMWF model output and L2 processor parameters. Especially the latter were not available which is why this part of the algorithm was not implemented during this thesis.

Complex signals and spectral analysis
In this short example, we investigate the Frequency domain resulting from a complex signal. First we take a look at Eulers identities, two formulations which provide the relation between a real cosine or sine wave and complex exponentials, [46]. Euler stated that:

$$\cos(2\pi f_0 t) = \frac{e^{j2\pi f_0 t}}{2} + \frac{e^{-j2\pi f_0 t}}{2} \tag{3.12}$$

$$\sin(2\pi f_0 t) = \frac{j\ e^{j2\pi f_0 t}}{2} - \frac{j\ e^{-j2\pi f_0 t}}{2} \tag{3.13}$$

Eulers identities provide a description of a complex signal, when viewed in the frequency-domain. An example is given in Figure 3.12, showing a single cosine and sine wave and their depiction in the frequency domain. It becomes obvious that a cosine wave results in two peaks of the same magnitude on the real plane and a sine wave results in two peaks with opposing magnitude in the complex plane.

$$y(t) = A_0 + \sum_{k=1}^{\frac{N}{2}} \left(A_k \cos 2\pi k \frac{t}{T} + B_k \sin 2\pi k \frac{t}{T} \right) \tag{3.14}$$

When we are looking at a complex signal resulting from a SAR image, we can describe the signal as the summation of a number of harmonic waves, according the the Fourier analysis. Using a Discrete Fourier Transform (DFT) it is now possible to present the signal in frequency domain, where every frequency is plotted on the frequency axis with their corresponding magnitude.

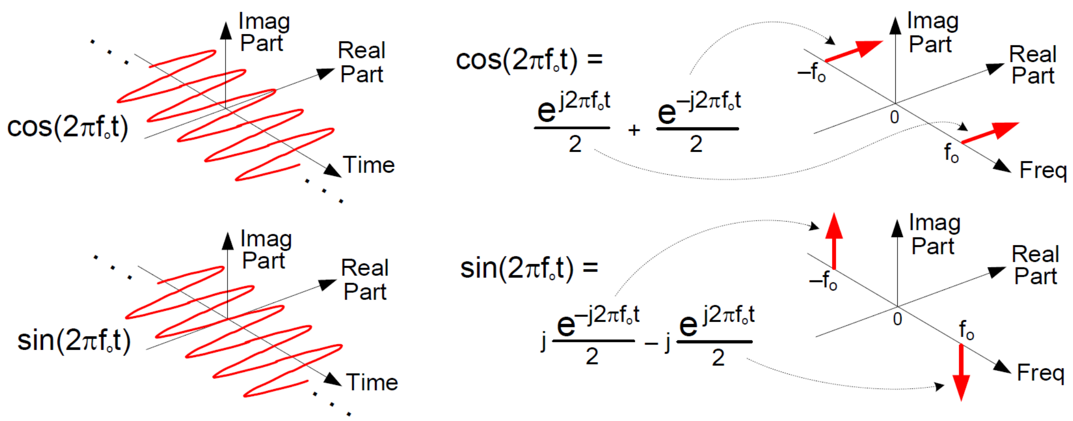

Figure 3.12: Complex frequency domain representation of a cosine and sine wave [46]

Algorithm implementation
The algorithm to calculate cross-spectra between SAR images was implemented in Python and can be found in the script *processing.py*. The algorithm first checks if a validation wave buoy, is located within the sub-swath. If this is the case the sub-swath is separated in a number of smaller imagettes with a size of 1024 x 1024 pixels, as shown in Figure 3.14. A case study from the Portuguese coast from 2014-11-25 was used as an example during the description of the method, a single imagette from this case study is shown in Figure 3.13.

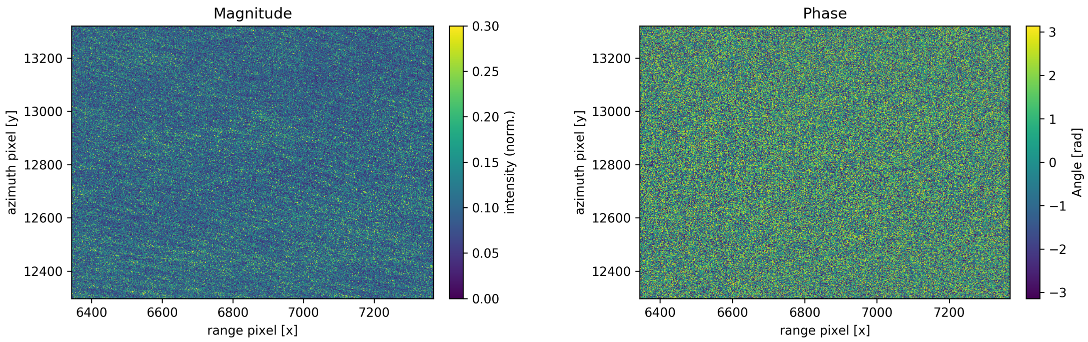

Figure 3.13: 1024 x 1024 imagette of an SLC image, with range pixel [x] from 6344 to 7368 and azimuth pixel [y] from 12297 to 13321. The left image shows the magnitude M and right image the phase $/theta$.

Image statistics
The next step is a check to see if the imagette does not cover land, or if there is an anomaly present in the imagette. This is done by calculating several image statistics from the complex image I_c. These statistics are the mean intensity μ, normalized variance $\hat{\sigma}$, skewness β_s and kurtosis β_k are shown in Equation 3.15 to Equation 3.18. If the variance has a value between $1.0 < \sigma < 1.5$ an imagette is processed, as shown in Figure 3.14.

$$\mu = \langle |I_c|^2 \rangle \tag{3.15}$$

$$\hat{\sigma} = \frac{1}{\mu^2} \langle \left(|I_c|^2 - \mu \right) \rangle \tag{3.16}$$

$$\beta_s = \frac{\langle \left(|I_c|^2 - \mu \right)^3 \rangle^2}{\langle \left(|I_c|^2 - \mu \right)^2 \rangle^3} \tag{3.17}$$

$$\beta_k = \frac{\langle \left(|I_c|^2 - \mu \right)^4 \rangle}{\langle \left(|I_c|^2 - \mu \right)^2 \rangle^2} \tag{3.18}$$

where < > denotes spatial averaging over the image subset.

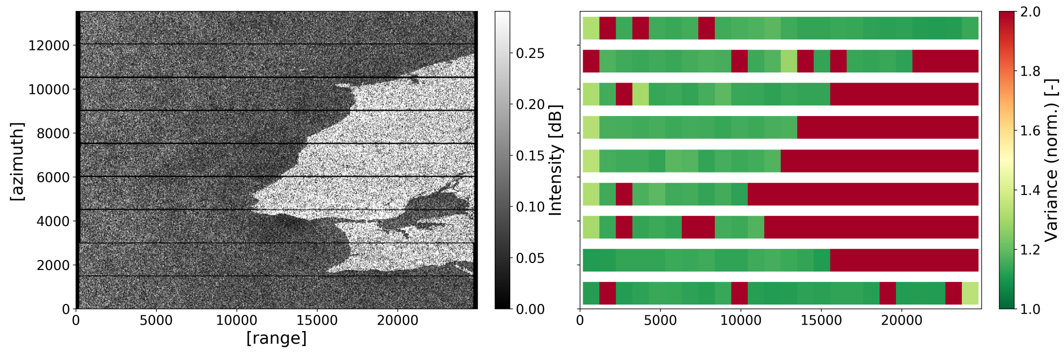

Figure 3.14: Left image shows a single SLC image sub-swath. Right shows the computed variance per imagette. Imagettes colored red were not processed.

Frequency domain

The processing of radar images is called Pulse-Doppler signal processing. In this section we will provide the reader with a very short introduction into this topic. The most important characteristics of Doppler signal processing are: 1) radar images are stored in complex notation, which means each sample has an amplitude and a phase value and 2) the radar image is stored in Time domain which, using an FFT (Fast Fourier Transform) , is transformed to Frequency domain.

An image stored in time domain, has samples which are separated in time. This is shown in Figure 3.15, where on the x-axis Range samples are shown and on the y-axis the different pulses. SLC imagettes, e.g. Figure 3.13 are stored in time domain. When we now apply an FFT on the image in time domain, the image is transformed to Frequency Domain. In frequency domain, the range samples (interval) are the same as in time domain, however we now observe a spectrum of frequencies along each sample interval.

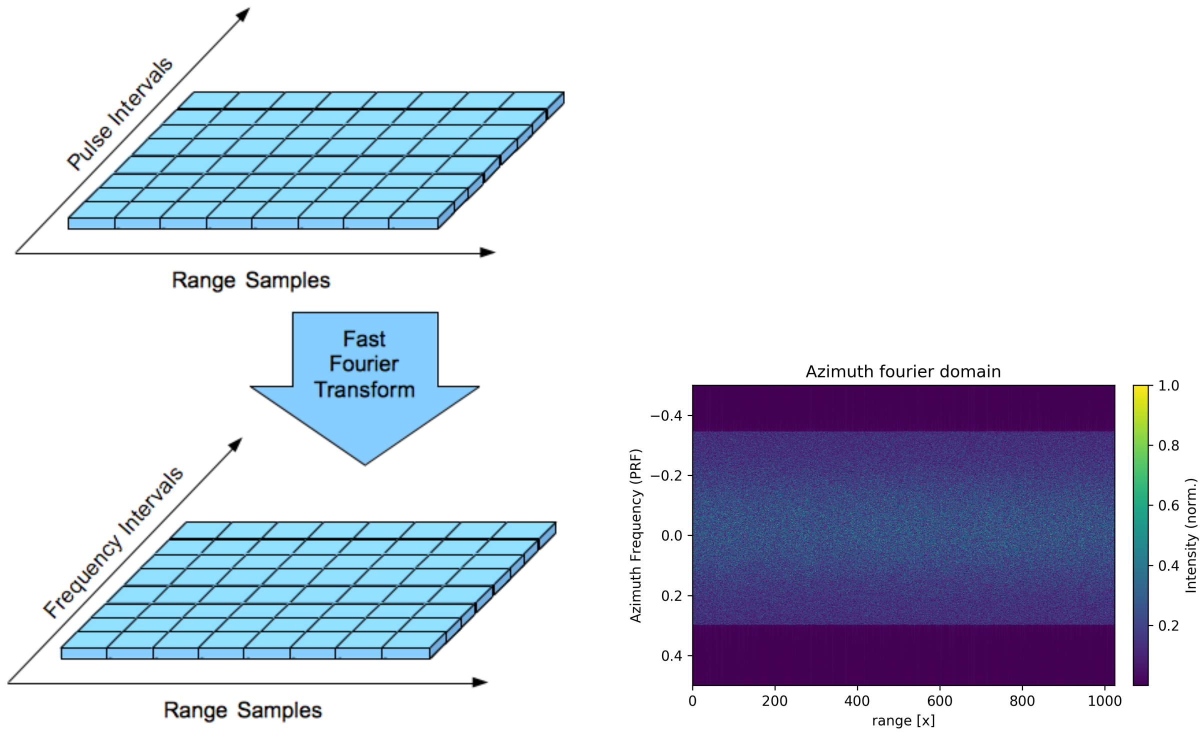

Figure 3.15: Left image shows Doppler processing of an image. The Range Sample axis represents individual samples taken in between each transmit pulse. The Fast Fourier Transform process converts time-domain samples into frequency domain spectra (from [4]). The right image shows the frequency domain of an SLC imagette.

The Fast Fourier Transform works fastest when a power of 2^n is used, which is also the reason why imagettes of 1024 pixels were used during the implementation of this algorithm. The Fourier transform of an image can mathematically be described with:

$$\hat{x}(f) = \int_{-\infty}^{\infty} e^{-2\pi i f t} x(t) dt \tag{3.19}$$

[4] https://en.wikipedia.org/wiki/Pulse-Doppler_signal_processing

Band-pass filter
We can now process the radar image in frequency domain. Figure 3.16 shows the Frequency domain resulting from a FFT in azimuth direction. The right image shows the 2D view, with an azimuth frequency spectrum per range interval [x]. The left image shows the mean azimuth profile, which is computed by taking the mean of the 2D image in range direction. This profile can be interpreted as a side-view of the 2D image. The frequency in Figure 3.16 is displayed in terms of Pulse Repetition Frequency (PRF). The PRF is equal to $PRF = 1/\tau$. Where τ is the azimuth time interval. Sentinel-1 has an azimuth time interval of $\tau = 0.0020556s$, resulting in a PRF of 486.5 Hz. In the example of Figure 3.16 a value of 0.2 corresponds with a frequency of $f_{az} = 0.2 * 486.5 = 97.3 H_z$.

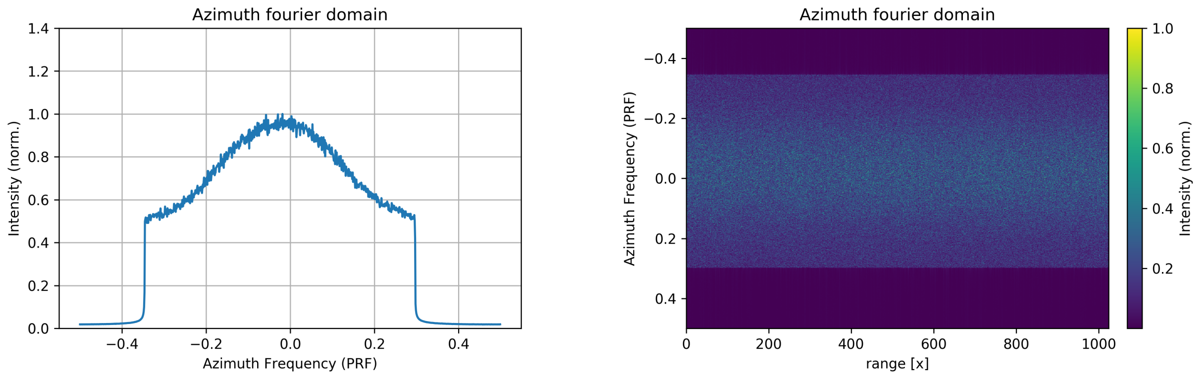

Figure 3.16: Mean intensity of the azimuth frequency domain (top) and a azimuth frequency along range (bottom), with intensity normalized and frequency displayed in terms of the Pulse Repetition Frequency (PRF).

This mean profile shows a sinc window function with a cut-off frequency of approximately 0.3 PRF. This window function is a result of the deramping which was applied during pre-processing. This window function must be removed before we can create individual sub-looks. Removal of the signal is done by fitting a sine curve to the azimuth profile using a least squares optimization [5], fitting of the sine function is shown in Figure 3.17. The magnitude of the original profile is divided by the magnitude of the fitted profile, resulting in a rectangular profile in the Fourier domain, see Figure 3.17.

Removing the window function is performed using the following expression:

$$I_{c,new} = \frac{M_{or}}{M_{fit}} e^{i\theta_{or}} \tag{3.20}$$

Where M is the magnitude of the original and fitted signal and θ is the phase of the original image.

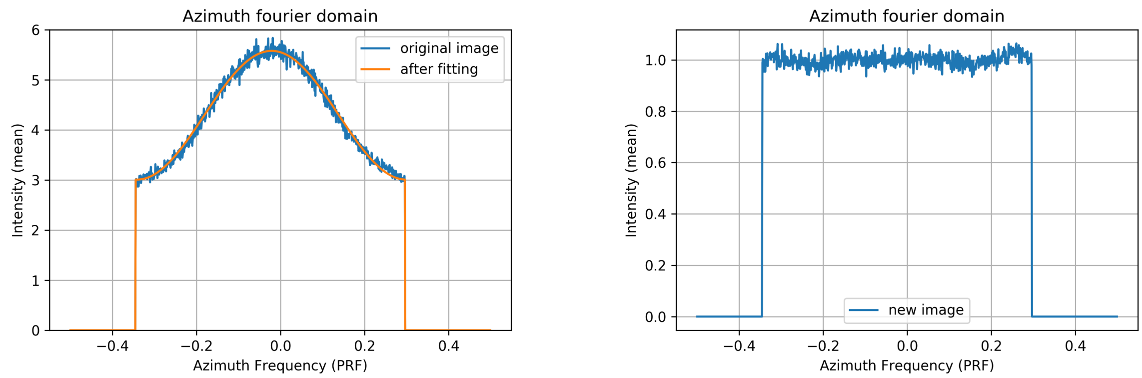

Figure 3.17: Fitted profile to the mean azimuth spectrum (left) and resulting azimuth profile after dividing the original profile with the fitted profile (right).

[5]https://docs.scipy.org/doc/scipy/reference/generated/scipy.optimize.leastsq.html

Creating sub-looks

The next step is creating different sub-looks from the rectangular azimuth profile. This is possible due to a special characteristic of the azimuth Frequency domain: with increasing the frequency interval we observe the image also a time interval later, since time and frequency are interchangeable in this domain. We are now going to define three sub-looks using a Hamming window with a different frequency (hence time) interval. In Figure 3.18 we see how this is done. The left image again shows the mean azimuth Fourier domain. On the right image we see what a sub-look looks across range direction.

The size N of the hamming window of an individual sub-look is equal to a third of the Doppler bandwidth from the original image, for this example that would correspond to a filter width of $\Delta F = 0.21 PRF$ in azimuth. In range direction only one look is used with a length equal to the size of the imagette (1024 pixels). The time delay between consecutive sub-looks is 0.45 seconds and 0.9 seconds for the first and the third look.

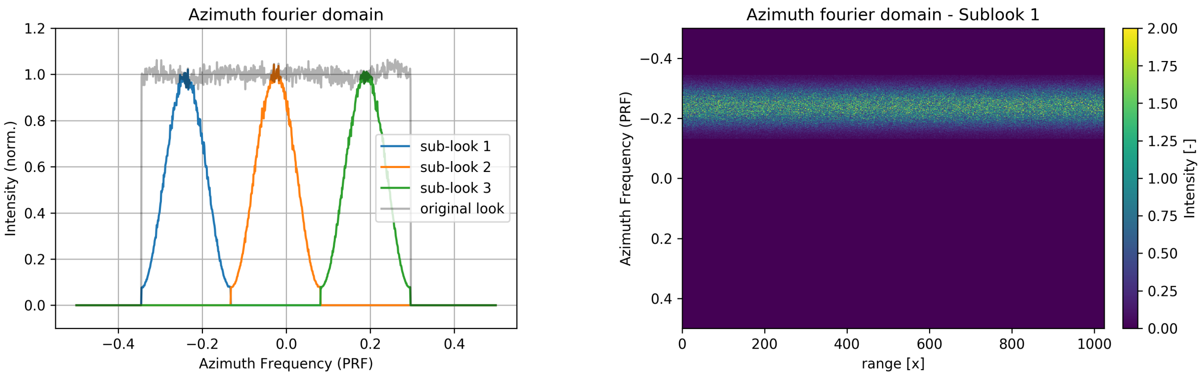

Figure 3.18: Three different sub looks are created by applying a hamming window on the signal with a different azimuth bandwidth.

The three sub-looks are transformed back to the spatial domain by computing the inverse FFT of the azimuth image. Next an intensity image is created from each separate sub-look as defined by:

$$I^{(m)}(\underline{x}) = \left| \frac{1}{(2\pi)^2} \int d\underline{k} \quad I_c(k,t) \quad e^{-ik\underline{x}} \right|^2 \tag{3.21}$$

with m = [1, 2, 3]

For this test the intensity images of individual sub-looks are:

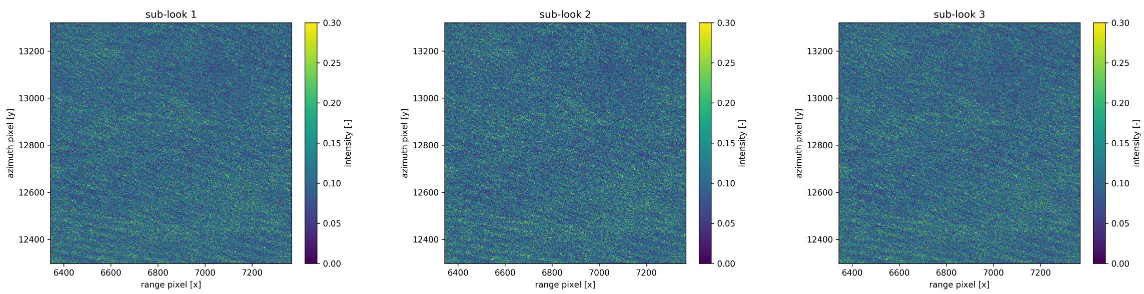

Figure 3.19: Three intensity images from different sub-looks of an SLC image.

Cross-spectra

Now that three sub-looks have been obtained from a single SAR image, we can calculate the cross-spectrum between those. First a 2D FFT is applied on the intensity image of each sub-look, next we multiply one 2D FFT with the complex conjugate of the other sub-look 2D FFT, which is shown in Equation 3.22. What now happens is the following: when both sub-looks have a peak at a certain wave number k, e.g. 0.0025 1/m (which would correspond to deep water swell with a wave length of 400 m and period of 16 s) the cross-spectrum between the two sub-looks will also show a peak at $k = 0.0025$ 1/m . The cross-spectrum consists of a real and imaginary part, as is shown in Figure 3.20.

What happens when the cross-spectrum between sub-looks is constructed is also explained by Vachon and West [63]: *"Since the displacement of the wave energy between looks appears as a phase shift of the corresponding wavenumber component, the energy is automatically registered when the individual look Fourier transforms are detected (the phase is lost) and the peak spectral contrast may be increased. "*

The co- and cross-spectra are computed from the individual look images as follows:

$$P_s^{(m,n)}(k, \Delta t) = \frac{1}{\langle I^{(m)} \rangle \langle I^{(n)} \rangle} \langle I^{(m)} \left(k, \frac{t}{2}\right) I^{*(n)} \left(k, -\frac{t}{2}\right) \rangle \tag{3.22}$$

With:

$\langle I^{(m)} \rangle$	= mean image intensity
$I^{(m)} \left(k, \frac{t}{2}\right)$	= Fourier transform of the intensity image, as specified in Equation 3.21
$\Delta t = \frac{t}{2} - (-\frac{t}{2})$	= look separation time between look intensity images

An asterisk (*) in Equation 3.22 denotes the complex conjugate of the image and < > denotes smoothing of the computed spectra. The window function applied for smoothing is a Hamming window, with 9 points set as the output window.

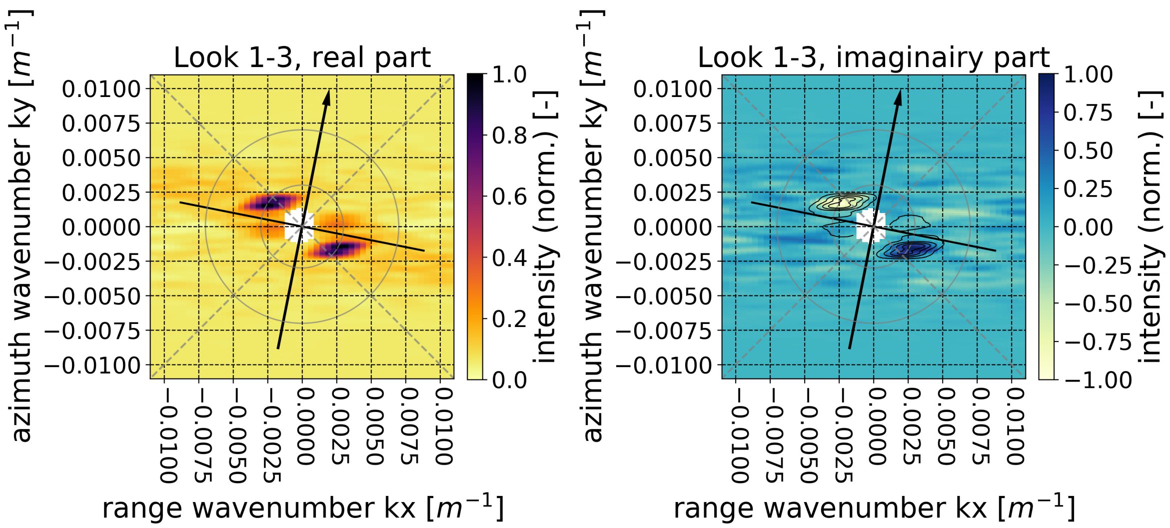

Figure 3.20: The real and imaginary part of the cross-spectrum between look 1 and look 3. The black arrow indicates North.

Cross spectrum of two complex images
This elucidation explains the mathematical background of the cross spectrum between two images. First we write the complex representation of a fourier timeseries, according to [28]. Note that $x(t)$ and $y(t)$ are 1-D time series, altough the same approach applies to 2D time series as well.

$$x = \bar{x} + \sum_{kN2}^{N2} F_x(k) y = \bar{y} + \sum_{N2}^{N2} F_y(k) \tag{3.23}$$

where:

$$F_x(k) = C_{xk} e^{i(\frac{2\pi kt}{T})} e^{i\theta_{xk}} = \frac{1}{2}(A_{xk} - iB_{xk}) e^{i(\frac{2\pi kt}{T})} \tag{3.24}$$

$$F_y(k) = C_{yk} e^{i(\frac{2\pi kt}{T})} e^{i\theta_{yk}} = \frac{1}{2}(A_{yk} - iB_{yk}) e^{i(\frac{2\pi kt}{T})} \tag{3.25}$$

In terms of these complex Fourier transformations, we can now define the complex cross spectra. A superscript asterisk indicates the complex conjugate.
We can write the complex cross spectrum $F_{xy}(k)$ between two time series $x(t)$ and $y(t)$ as

$$F_x(k) F_y^*(k) = \frac{1}{2}(A_{xk} - iB_{xk}) e^{i(\frac{2\pi kt}{T})} \frac{1}{2}(A_{yk} - iB_{yk}) e^{-i(\frac{2\pi kt}{T})} \tag{3.26}$$

In complex notation we can write the cross spectrum as:

$$F_{xy}(k) = C_{xk} C_{yk} e^{i(\theta_{xk} - \theta_{yk})} \tag{3.27}$$

$$= C_{xk} C_{yk} (\cos(\theta_{xk} - \theta_{yk}) + i \sin(\theta_{xk} - \theta_{yk})) \tag{3.28}$$

The cospectrum is the real, in-phase, part of the signal and the quadrature spectrum is the complex, out-of-phase signal. If we combine this definition with the describtion of Eulers identity, Figure 3.12, it becomes easier to "understand" a computed cross-spectrum from two SAR sublooks.
The cospectrum shows the real part of the spectrum and is described by a cosine wave and a magnitude. For a given value, we will see a positive magnitude at opposing frequencies. The complex part of the cross spectrum shows both negative and positive magnitudes for opposing frequencies, since it is described by the quadrature spectrum. The term $\theta_{xk} - \theta_{yk}$ denotes the phase difference.

The 180 degree ambiguity
As mentioned in previous sections, we use the cross-spectral method to resolve the 180 degree ambiguity, knowing in which directions waves are moving towards to. The imaginary part of the SAR image cross spectrum is used to remove the 180 degree ambiguity, where the cross spectrum with the longest time separation is used [6]. A positive peak of the imaginary cross spectrum indicates the direction where wave are moving towards to. In this case the cross spectrum between individual looks 1 and 3 are used. The underlying assumption is that a longer time separation between consecutive images makes it easier to resolve direction. The left image in Figure 3.20 shows the imaginary part of the cross-spectrum. A positive peak is observed at South-West direction, which means this is the direction the waves are heading to.

3.2.3. Validation

The final step is validation of the computed S-1 SAR cross-spectra. Validation is performed using wave buoy spectra and by calculating the cross-spectra from simulated SAR images. In this section the different processing steps of validation data are presented and how the data was configured.

Wave buoy data

The wave buoy data was provided with a value for three parameters: the energy density, direction and a spreading. From theses three parameters the 2D ocean wave spectrum is constructed using a spreading function. Additionally, the wave buoy data is provided in frequency bins in Polar coordinates while the SAR spectra are in Cartesian coordinates. Therefor the wave buoy spectra were transformed from frequency-direction to wave number kx-ky domain[60], a further elaborated can be found in Appendix B .

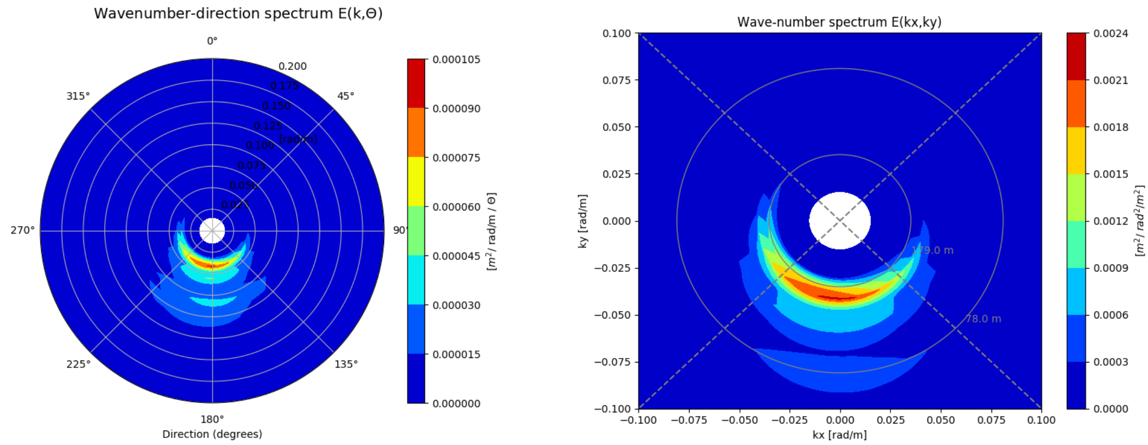

Figure 3.21: Transformation from a 2D wave buoy spectrum in polar form to Cartesian coordinate system.

In order to compare buoy data with cross-spectra from SAR data, wave buoy data was rotated to match the frame of reference of the S-1 satellite. The heading of the satellite is calculated from the satellite metadata. For an ascending pass in the North Sea the heading is on average 11.2 degrees. The direction varies per sub-swath, where the first sub-swath has a heading of around 10.2 degrees and the last sub-swath around 12.2. Figure 3.22 shows the different heading of an ascending and descending pass, in this case the average rotation was -11 degrees in clockwise direction for an ascending pass and -169 degrees for a descending pass.

Figure 3.22: Overview of two SAR images in SNAP. Left image shows a descending pass, the right image shows an ascending pass.

OCEANSAR data

The OCEANSAR simulator uses wave buoy data as input to generate an ocean surface. buoy data was retrieved from the Monican wave buoys in Portugal and the K13 and AUK buoy in the North Sea. A simulation from OCEANSAR follows the following steps:

1. generation of an ocean surface using spectral wave data
2. generation of a RAW radar image
3. generation of a processed radar image.

The resulting output of the OCEANSAR simulator is comparable to a stripmap Sentinel-1 image. The resolution is approximately 15 m in azimuth and 5 m in range.

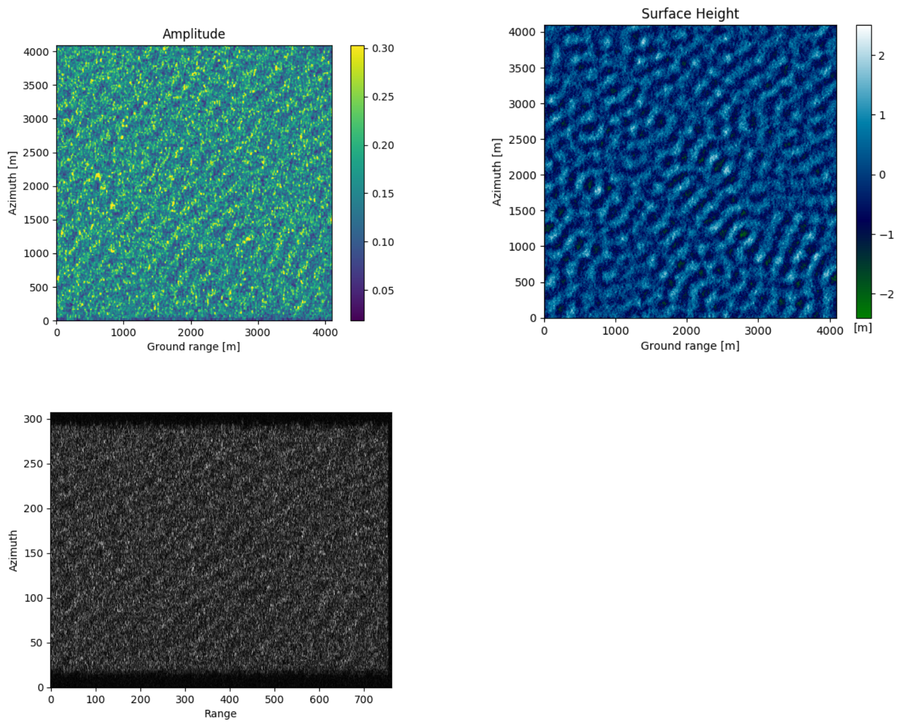

Figure 3.23: Output from OCEANSAR using buoy data from the Monican 1 buoy on 25-11-2014 19:00. Top left image shows the intensity image, top right shows the simulated ocean surface and the bottom image shows the computed intensity of a resulting SLC image.

Processing buoy data

The OCEANSAR module uses wave buoy data to simulate the ocean surface. Since we are using the same algorithm to process OCEANSAR data, as well as S-1 SAR data, the OCEANSAR images had to be oriented in the same direction, with the same axis as the sentinel-1 data. Additionally, in the OCEANSAR frame of reference, the direction of the waves is the direction where waves are heading towards to. Wave buoy data is provided with a direction where waves are coming from, which means the data needs to be mirrored.

1. The buoy data is rotated so the x axis matches the x axis of the SAR data by adding the heading of the satellite to the direction of the waves.
2. The data is mirrored along both axes to provide data where the direction is the direction where waves are heading towards to.

An example wave data file is available in Appendix A, as well as a configuration file needed to configure a single OCEANSAR run. Parameters which were adjusted for each file are:

path	path where the OCEANSAR output is stored
heading	heading of the satellite, defined as East of North
buoy_data_file	location and filename of the wave data file
year	year of the case study
month	month of the case study
day	day of the case study
hour	our of the case study
minute	minute of the case study

4 Results

This chapter is a summary of the results from 14 case studies and a discussion of the results. In Appendix B a full report of these case studies can be found. Images of cross-spectra are shown in Cartesian coordinates, with wavenumber k_x in the x-direction and k_y in y-direction. North direction is indicated with a black arrow.

4.1. Cross-spectra from Sentinel-1 SLC images

A total of 11 case studies were analyzed in the North Sea and 3 case studies along the Portuguese coast. The method used to select test cases was presented in the previous chapter: possible presence of swell waves and a low-wind speed. Out of the 11 SAR images, 6 SAR cross-spectra showed a positive result, in which a swell peak was visible and the peak matched spectral data from wave buoys.

Table 4.1 shows the results and conditions for different case studies, with $Hm0$ the significant wave height, $HE10$ swell wave height, Tp peak period, Dir direction of the waves, $U10$ wind speed and $U-dir$ direction of the wind. Spectrum quality is expressed a scale ranging from bad (- -) to excellent (+ +). Excellent quality indicates a clear swell peak is observed on the SAR cross-spectra, with the peak matching buoy measurements. This is most likely observed during high swell wave height HE10 conditions and long peak period Tp.

Each SLC sub-swath was divided in 1024x1024 imagettes, only a single imagette per sub-swath was processed, Table 4.1 indicates the position of the processed imagette. Some information, e.g. the wave direction or swell wave height was only available for either North Sea case studies or Portuguese case studies.

Table 4.1: Overview of the results, case studies 1-11 are from the North Sea and 12-14 from Portugal.

Case study	Date	Hm0 [m]	HE10 [m]	Tp [s]	Dir [deg]	U10 [m/s]	U-dir [deg]	Spectrum quality SAR	Spectrum quality OSAR	SAR Imagette [azimuth,range]
North Sea										
1	26-04-2015	1,11	0,6	11,1		4,02	345,6	+	+	7, 18
2	19-05-2016	0,71	0,36	11,1		8,24	193,9	-	+	8, 18
3	01-10-2016	1,12	0,22	5,0		2,75	159,6	-	-	1, 16
4	30-10-2016	1,04	0,62	11,1		0,82	320,4	++	++	7, 9
5	31-10-2016	0,72	0,31	11,1		2,46	197,5	+	+	2, 8
6	29-11-2016	0,75	0,24	10,0		7,14	261,6	--	--	6, 15
7	10-12-2016	0,82	0,27	5,6		6,71	240,8	+-	-	7, 15
8	08-01-2017	0,89	0,48	14,2		3,32	222,1	+	+	7, 13
9	09-01-2017	2,13	0,3	6,3		13,37	216,5	--	--	7, 9
10	16-01-2017	0,94	0,58	14,3		3,73	134,3	+	+	6, 13
11	21-01-2017	0,79	0,34	11,1		5,16	100,6	--	+	7, 5
Portugal										
12	25-11-2014	2,05		17,28	316,7	5,05	294,7	++	++	8, 10
13	24-01-2015	1,72		10,88	346,6	8,43	25,8	+	+	8, 9
14	27-10-2015	4,92		15,84	312,1	7,97	238,3	++	++	2, 3

North Sea

In Figure 4.1 we can see the results from three case studies in the North Sea. These three case studies showed a positive result, where a swell peak is observed on the SAR image, matching wave buoy measurements, see Table 4.1. Case study 4 shows waves with a wave number k_y of around 0.005 1/m, coming from Northern direction. From this example we can also observe the different orientation between ascending pass (case studies 4 and 10) and a descending pass (case study 5).

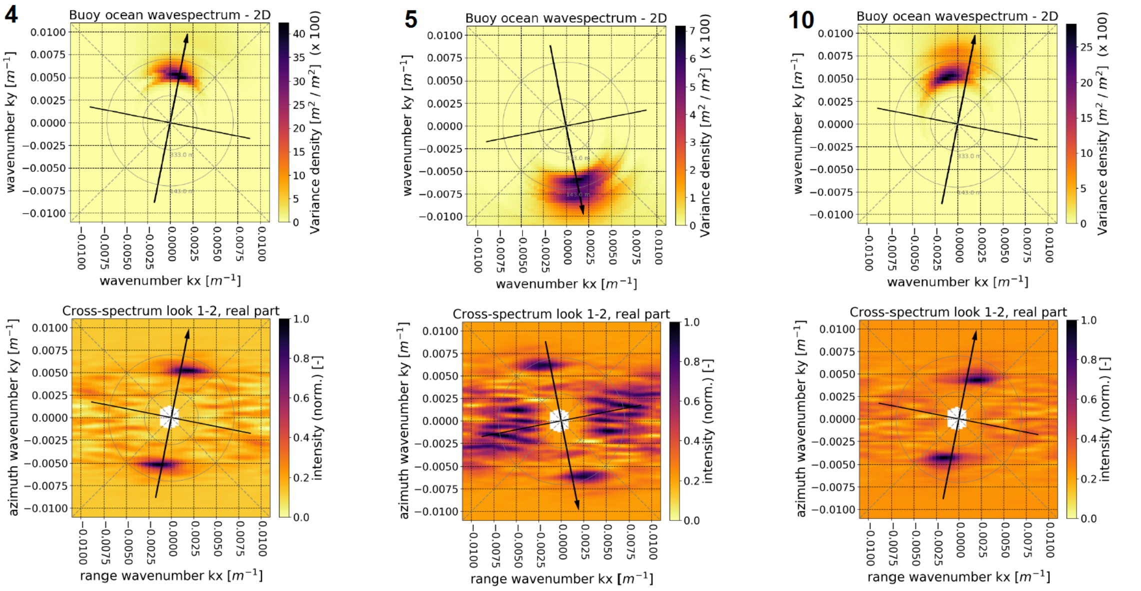

Figure 4.1: Results from case studies from the North Sea, top images show wave buoy spectra, bottom images retrieved SAR cross-spectra. From left to right images are shown from case study 4, 5 and 10. These case studies had a positive result where a swell peak is visible on SAR cross-spectra.

Also of interest is case study 10 with an exceptionally long period swell of 14.29 s on buoy measurements. Using the dispersion relation we can determine the corresponding wave length, which is around 220 m at a water depth of 30 m. From Figure 4.1 we find a swell peak around $kx = -0.00211/m$ and $ky = 0.00431/m$ resulting in $k = 0.00431/m$ or a wavelength of $233m$, which confirms that the SAR observations are almost similar to the buoy measurements. Another interesting observation is a change in direction of the swell peak along different SAR imagettes, probably due to refraction of the longer wave lengths.

In chapter 2 we found that a SAR cross-spectrum consists of two parts: a non-linear part (which can be attributed to wind-sea) and a quasi-linear part (which can be attributed to swell). The S-1 cross-spectra in Figure 4.1 show the different parts. Case studies 4 and 8 (see Appendix B) show a clear quasi-linear swell peak. For these case studies a low wind speed U10 < 3 m/s was observed and a long period of respectively 11 and 14 seconds, respectively. Case study 5 shows a swell peak with additional "background noise", this is caused by a lower signal to noise ratio. The swell wave height decreased to 0.3 m during this case study, with an increase in wind speed it becomes more difficult to detect the swell spectrum, hence an increase in "background noise".

Portuguese coast

Three cases were tested along the Portuguese coast, resulting cross-spectra are shown in Figure 4.2. The Portuguese coast is exposed to waves coming from South-West to North-West direction and is known for its exceptionally large swell [55]. This was also observed during case studies 14 and 12, with a wave height of 4.92 m (15 s period) and 2.05 m (17.3 s period) respectively. Field observations of local surfers during case study 12 reported even larger swell. Corresponding wave lengths are between 300 m and 400 m.

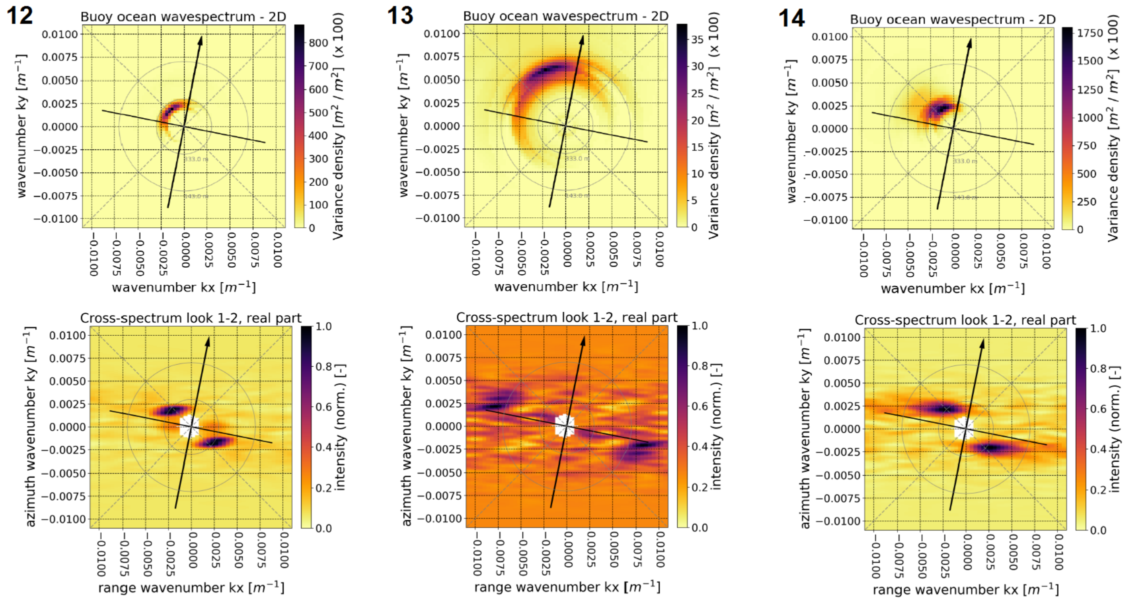

Figure 4.2: Results from case studies along the Portuguese coast, top images show the wave buoy spectra, bottom images retrieved SAR cross-spectra. From left to right images are shown from case study 12, 13 and 14. Case studies from Portugal had the best result where a distinct swell peak is visible on SAR cross-spectra.

Case study 13 shows a lower significant wave height (1.7 m) and a shorter period (11 s) lower than the other Portuguese case studies, which resulted in a more distinct non-linear part of the cross-spectrum. There also seems to be a difference in direction between buoy measurements and cross-spectra, this was observed in multiple imagettes on the SAR image. Another observation is refraction of waves approaching the coast. Imagettes from Figure B.46 which are close to the coast show a change in direction of the swell peak compared with buoy measurements, the spectral peak is shifted in range direction. This change in direction is for example, visible on imagettes [3, 12] and [4, 14].

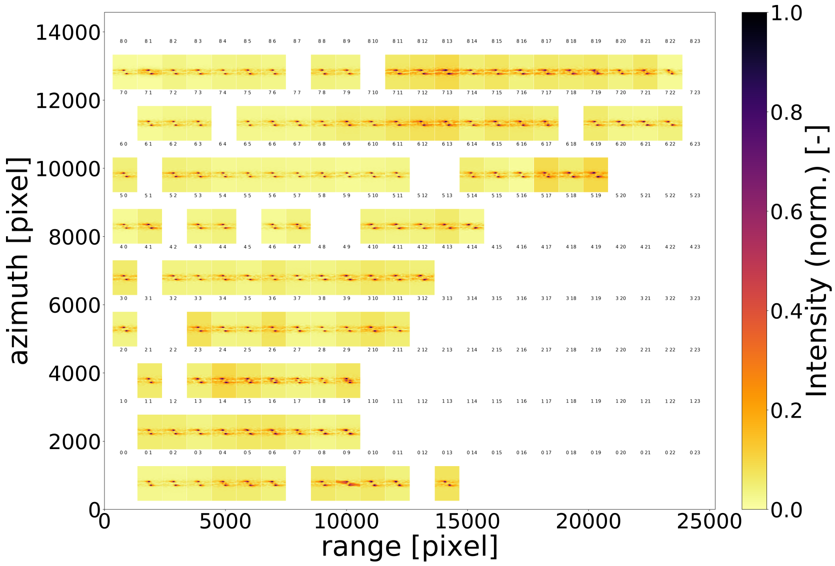

Figure 4.3: Cross spectra between sub-look 1 and sub-look 3 for different imagettes. Imagettes closest to the coast are located on the right and show a different direction.

4.2. Effect of hydrodynamic conditions

In Figure 4.1 the results are shown for case studies during low wind conditions ($U10 < 5.0m/s$) and medium to high swell conditions ($HE10 > 0.5m$). In the North Sea, these conditions led to the best result in terms of spectral quality. Figure 4.4 shows the opposite result; in case study 2, 6 and 11 swell cannot be observed. This can be attributed to two reasons. The swell wave height was low during these conditions, between 0.2 and 0.4 m and the wind speed was larger, between 5 and 8 m/s, this combination made it impossible to retrieve a swell spectrum.

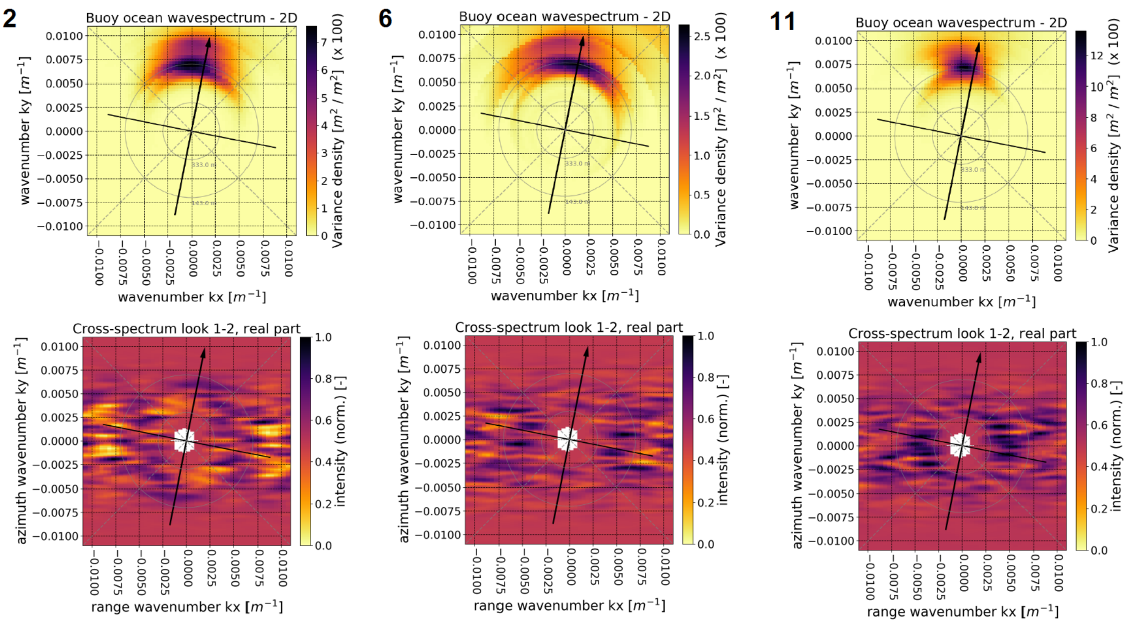

Figure 4.4: Results from case studies from the North Sea, top image show the wave buoy spectra, bottom images SAR cross-spectra. From left to right images are shown from case study 2, 6 and 11. All three case studies had a negative result; due to hydrodynamic conditions a swell peak could not be observed from the SAR cross-spectra.

Another interesting feature is observed for case study 5 in Table 4.1: an increased in Bragg scattering due to the presence of wind-generated capillary waves. As explained in Chapter 2, the main scattering mechanism for SAR is Bragg scattering of capillary waves. A large part of the SLC sub-swath shows non-linear features. The shape and appearance of these streaks indicate that they are trails resulting from marine activity (see Figure 4.5), an effect also described by Collard et al. [13]. Wave buoy observations showed a very low wind-speed during this day, combined with the observations of the shipping trails, it indicates that there are almost no capillary wind-waves present during the acquisition of this radar image. The radar image does show an area with increased backscatter, this is probably due to the presence of a wind gust. This area did show a swell-peak that matched the buoy measurements from Figure 4.1.

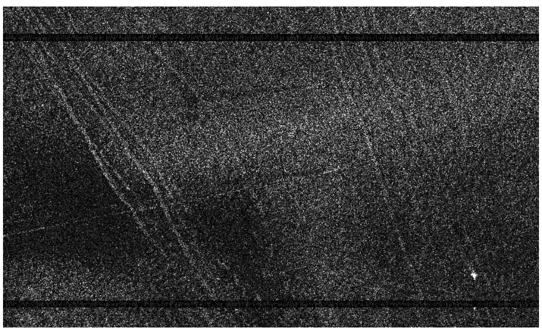

Figure 4.5: Close-up made in SNAP of the SAR SLC image on 2016-10-31. Several streaks are visible on the intensity image as a result of marine activity.

4.3. Ascending vs descending pass

Out of the total of 14 analysed case studies, 2 case studies contained a descending pass. Unfortunately, both case studies showed low-amplitude swell conditions(HE10 between 0.2 and 0.3 m) on buoy observations which made retrieval of the ocean wave spectrum difficult. Still around 10 imagettes from each SAR image showed a swell peak which matched buoy observations. Figure 4.6 shows the SAR image spectrum of the case study on 2016-10-31, both buoy spectra, SAR spectra and OCEANSAR spectra match fairly well, with corresponding wave numbers and direction. Descending passes have a different angle of incidence compared to ascending passes. In the North Sea, swell waves are expected to mainly originate from Northern direction, which means the incident direction is different: approximately -11 degrees for an ascending pass and -169 degrees for a descending pass. Case studies 4 and 5 provide a good comparison between two different passes. In both cases waves were coming from North direction and observing a swell peak was possible in both cases. Case study 5 did show a larger non-linear contribution, however this can be explained by the lower swell wave height (0.3 m) observed on this day.

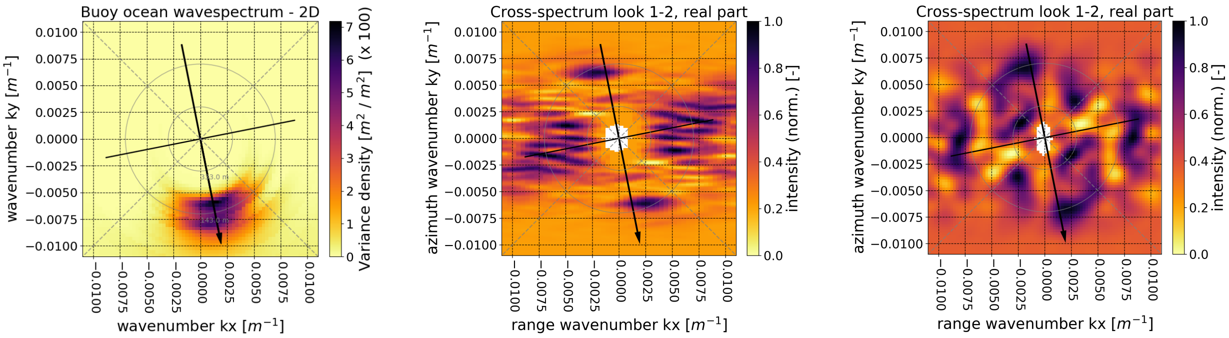

Figure 4.6: K13-alpha buoy spectra (left), SAR cross-spectra (middle) and OCEANSAR cross-spectra (right) from case study 5 (31 October 2016).

4.4. Solving the directional ambiguity

SAR cross spectra show a 180 degree ambiguity. Bao and Alpers [6] proposed this ambiguity can be resolved using the imaginary part of the cross spectrum. When a swell peak on the real part of the spectrum matches a positive peak on the imaginary part of the spectrum, this is the direction where the waves are heading to. Figure 4.7 shows the imaginary part of the cross-spectrum of case study 12, which shows a positive peak at kx = + 0.0025 1/m and ky= - 0.0025 1/m. This would indicate this is the direction where the waves are heading to, according to buoy data from that day, this is indeed the correct direction.

For case studies in the North Sea it was much more difficult to resolve the 180 degree ambiguity. In Figure 4.7 we find for the North Sea cross spectra a swell peak at ky = + - 0.005 1/m. The real part of the spectrum shows a clear peak, however this is not visible for the imaginary part. With some difficulty we could distinguish a positive peak at ky = -0.005 1/m, which would match buoy observations, however this is debatable. An explanation is provided by Collard et al. [13], who mentions the ambiguity removal process is difficult due to the low Signal-To-Noise Ratio (SNR), which is a side effect of very low winds. It becomes difficult for the cross-spectral technique to resolve the propagation direction since the wave-induced backscatter intensity modulation is corrupted.

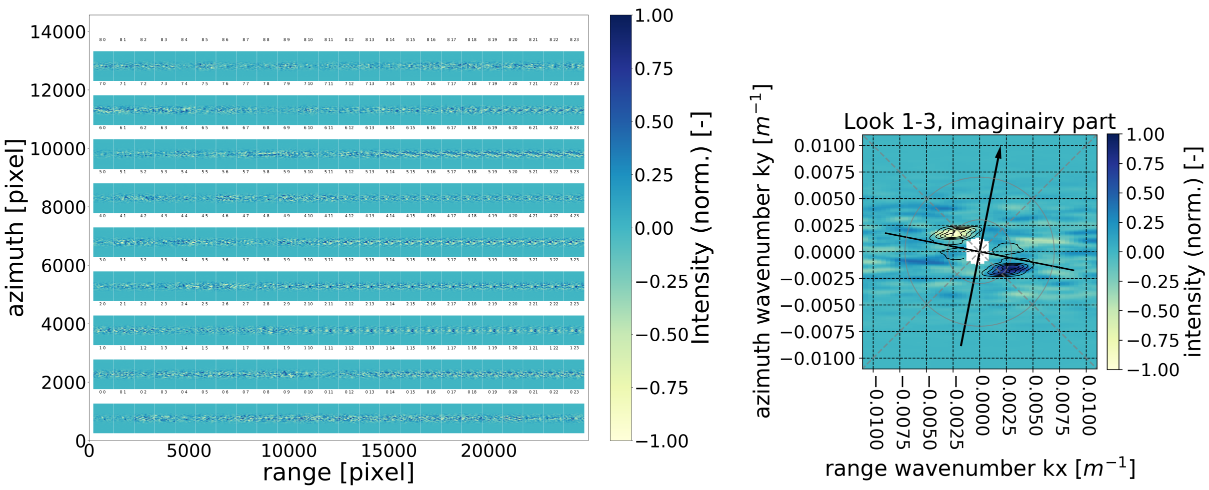

Figure 4.7: Imaginary SAR cross-spectra from case study 12 in Portugal. Left image shows imaginary part of the cross-spectrum for different imagettes. The right image shows a close-up of imagette [8,10]

4.5. Cross-spectra from OCEANSAR

This thesis shows one of the first attempts to use spectral wave buoy data as input for the OCEANSAR simulator. Using wave buoy data as input for OCEANSAR worked quite well. Several case studies showed a swell peak on the OCEANSAR image cross spectrum, which matched buoy observations. Cases where no peak was observed typically showed stronger wind speeds or low amplitude swell. Figure 4.8 shows case study 4 with a positive result, however the direction of the OCEANSAR spectrum is slightly shifted in anti-clockwise direction. This shift can be attributed to the random generated ocean surface from OCEANSAR. The ocean surface is generated with a random factor, as a result the direction of the waves can sometimes be slightly different compared to the buoy data.

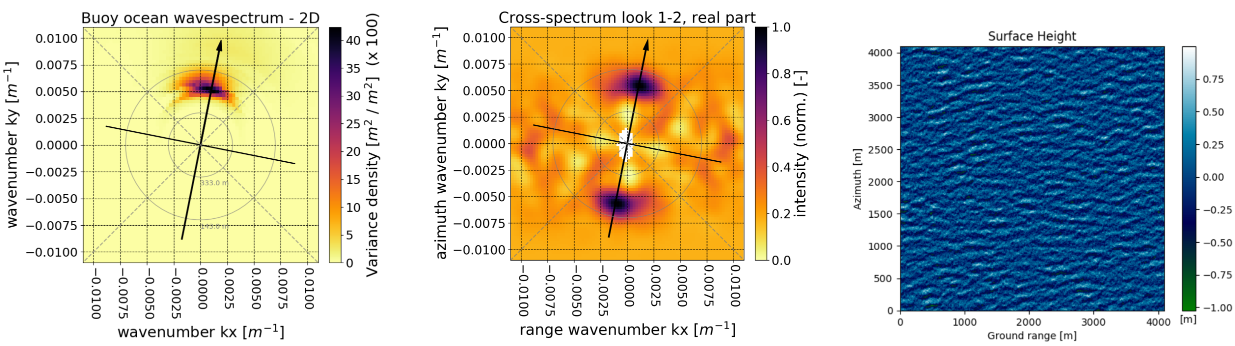

Figure 4.8: K13-alpha buoy spectra (left) and OCEANSAR image spectra (middle) from 30 October 2016.And simulated ocean surface (right). OCEANSAR spectra shows significant spreading compared to buoy spectra.

Directional spreading:

Another observation from OCEANSAR cross-spectra is an increased directional spreading compared to S1-SAR spectra, this effect is for example observed during case study 2, 10 and 11 in Figure 4.9. This is probably caused by the spreading function used to construct 2D spectra. Swell waves typically are long crested, coming from a single direction. This effect is also known as frequency dispersion. Due to this effect at a far away location only waves from a single direction are observed. This is why we see "perfect" waves along coasts. Due to sheltering of the North Sea by Great Britain and Norway, we would expect swell only from a direction of 330 degrees to 360 degrees reach the Dutch coast, while the cross-spectra show more spreading than possible.

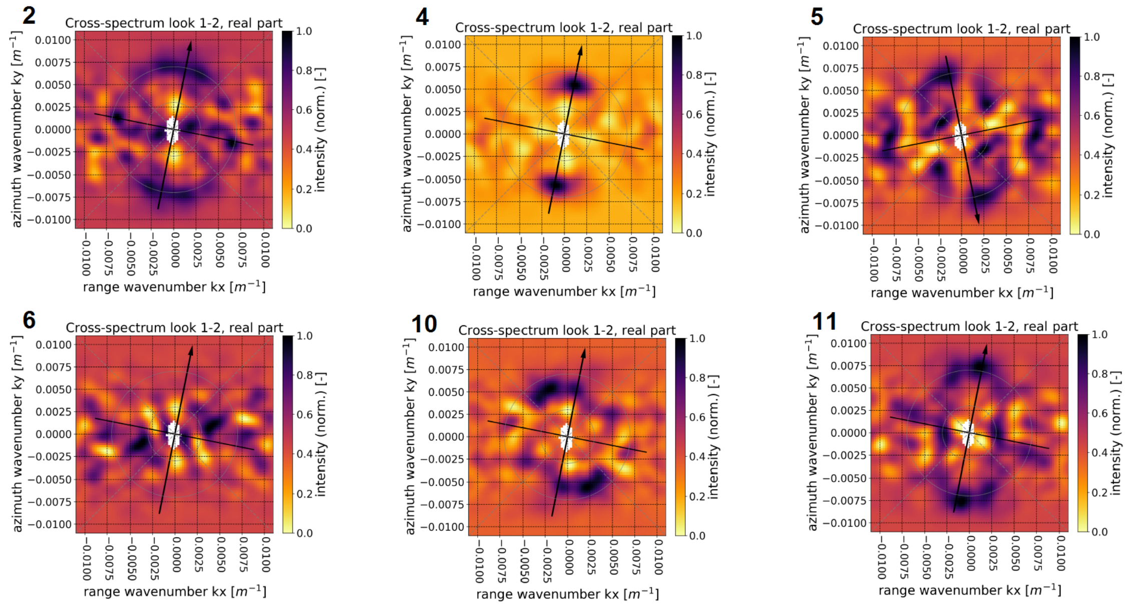

Figure 4.9: Cross-spectra from SAR images which were simulated by OCEANSAR using wave buoy data. Cross-spectra of case study 2, 4, 5, 6, 10 and 11 are shown.

Directional ambiguity:

From the imaginary part of the cross-spectrum we can determine the direction of the waves, this is also possible for OCEANSAR imagettes, as shown in Figure 4.10. From Figure 4.10 we observe that the waves are heading in north-westerly direction. This is the opposite of wave buoy measurements and SAR cross spectra, which show waves coming from North-West. This is probably the result of different reference frames, wave buoys indicate the direction of the waves with the direction where waves are coming from, while OCEANSAR indicates the direction where the waves are heading to. As a result this processing error was made.

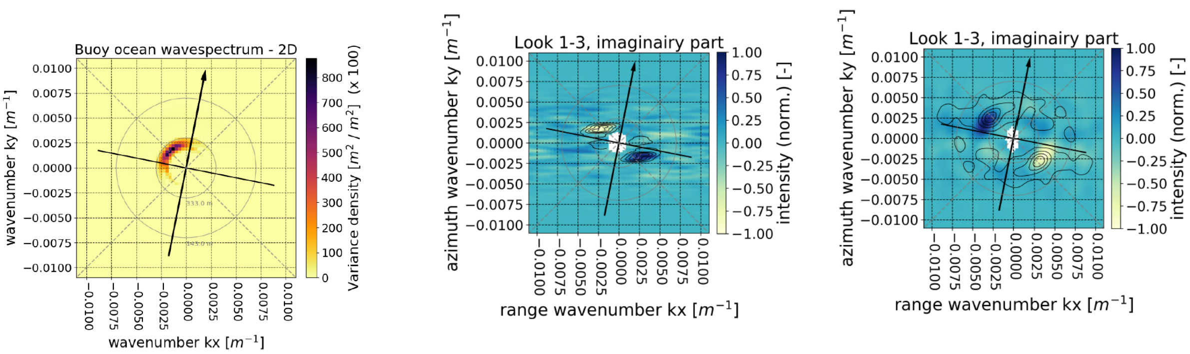

Figure 4.10: Imaginary part of the cross-spectrum, from case study 12. The right image shows cross-spectrum from an OCEANSAR imagette, middle image shows the cross-spectrum from a S-1 imagette. Contour lines are resulting from the real part of the cross-spectra. The left image shows reference wave buoy measurements.

4.6. Spectral smoothing

SAR image cross spectra from the Portuguese coast (e.g. case study 14 in Figure 4.2), but also from the North Sea (case study 10 in Figure 4.2) show an elongation in range direction. This effect is caused by a combination of pixel size and smoothing of the spectra. Smoothing was originally applied to reduce the effect of "noise" on the SAR cross-spectra and create a more distinct swell peak, however these results indicate that smoothing of the cross-spectra also has some drawbacks. SAR SLC images have rectangular pixels which are 13 m in azimuth and 2.3 m in range, SAR cross-spectra show 6 times more smoothing in range direction as a result. This effect is for example visible during case stud 14, where swell would come from a single direction, but is now elongated in range.

OCEANSAR smoothing:

This effect of an elongation due to smoothing was also visible on OCEANSAR spectra, only less distinct due to the different pixel size (15m in azimuth and 5 m in range), see Figure 4.9. Figure 4.11 shows results of case study 12, with a different smoothing window of 3 pixels, as well as cross-spectra separately processed by Paco Lopez Dekker. The different smoothing window shows a better resemblance with wave buoy spectra compared to a smoothing window of 9, which is shown in Figure 4.10. The separately processed cross-spectra shows less background noise in the SAR cross-spectra, the swell peaks of both cross-spectra are located at a similar direction. The occurrence of less background noise is the result of a different processing scheme as used during this thesis.

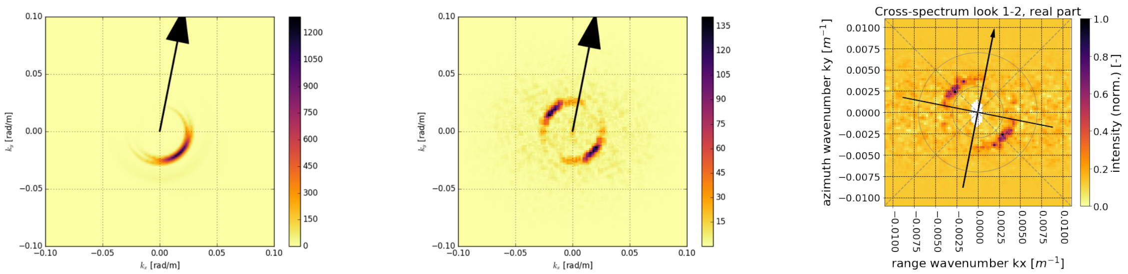

Figure 4.11: A test case to validate the OCEANSAR results with separate processing.

5
Conclusions

1. *Can the ocean swell wave algorithm be applied to Interferometric Wide Swath (IW) images of the North Sea?*
   The SAR image cross-spectrum can be divided into two parts, a quasi-linear part and a non-linear part. The quasi-linear part is a result of modulation by longer (low-frequency) swell waves. The non-linear part is contributed to the wind sea. Typical inversion schemes first evaluate the non-linear (wind sea) part of the spectrum and remove this part from the cross-spectra by subtraction [14]. The remaining quasi-linear swell spectrum can now analytically be solved using the modulation transfer function (MTF) and azimuth cut-off wave length. This theory is the underlying retrieval scheme for the Sentinel-1 Ocean Swell Wave (OSW) algorithm, which was implemented during this thesis.

   It was possible to implement the first part of the OSW algorithm, the Spectral Estimation Unit (see Appendix B), in which the SAR image cross-spectra and cross-variance functions are calculated. These are the SAR image cross-spectra which are evaluated during this thesis and shown in chapter 4. The second part of the OSW algorithm consist of the Spectral Inversion Unit. In this part of the algorithm, the non-linear (wind sea) part of the cross-spectrum is removed, azimuth cut-off wave length is calculated and the MTF is used to analytically solve the quasi-linear part of the cross-spectrum.

   This second part of the algorithm was not applied due to time limitations and missing information. It uses ECMWF wind information to remove the non-linear contribution. Additionally, the MTF is described using Look-Up-Tables (LUT), which are not publicly available. Technically it is possible to obtain ECMWF wind data manually and describe the MTF, implementing the MTF was out of the scope of this Msc. thesis.

   Several case studies were analysed in the North Sea and along the Portuguese Coast. For 6 of the SAR images in the North Sea a quasi-linear swell peak was observed, matching with spectral wave buoy observations. Observations showed swell pre-dominantly coming from NNW direction. All case studies in the North Sea showed a spectral peak, which matched buoy observations.

   To conclude this section, from the results we find that indeed, it is possible to apply (part of) the OSW algorithm. For the retrieval of the ocean wave spectrum from a SAR image spectrum, several additional steps need to be performed: removing of the non-linear part of the spectrum, determining modulation transfer functions and calculating the azimuth cut-off wave length.

2. *For which conditions can the Sentinel-1 SAR observe low frequency swell waves in the North Sea?*
   Results of the case studies showed the main parameters influencing capabilities of cross-spectral retrieval were swell wave height and wind speed. When the wind speed was lower than 5.0 m/s and the swell wave height higher than 0.5 m, a swell peak could be observed on the SAR image cross spectra. Exceptions were observed though, case studies showed spectral retrieval was possible at several imagettes with swell of only 0.3 m .

   While low wind speed led to a higher quality cross-spectrum, it was found that an absence of wind, in combination with a low swell height would lead to a reduction in quality of cross-spectra. One of the case studies (2016-10-31) was acquired on a date with low wind conditions. Streaks, absent during other cases, are visible on the SAR image caused by shipping trails or currents, which reduced spectrum quality. The reduction in spectral quality is also explained by the absence of Bragg waves. A different part of the SLC image showed an increase in Bragg scattering due to the presence of wind-generated capillary waves.

3. *Can SAR images be simulated using ocean wave spectra and can we apply the swell algorithm on simulated images?*
It is possible to use buoy measurements as input of OCEANSAR and to apply the OSW algorithm on simulated SAR images. Results from case studies showed corresponding swell peaks between buoy measurement, SAR image cross-spectra and OCEANSAR cross-spectra.

   Several differences were observed, SAR spectra showed an elongation in the range direction, a result of the different pixel resolution in range and azimuth direction. S-1 SAR images have rectangular pixels with a size of 2.3 m in range and 13 m in azimuth direction. Smoothing of the spectrum is applied using a window with a defined number of pixels. As a result, more smoothing is applied in range direction, compared to azimuth direction. The OCEANSAR simulator has a pixel size of 5 m in range and 15 m in azimuth, as a result the image cross-spectra showed less elongation in range direction.

   The OCEANSAR image cross-spectra showed more directional spreading compared to S1-SAR spectra, this effect is visible on the image cross spectra from 2015-04-26 and 2016-10-31. This increase in spreading can be attributed to the spreading function selected to process the buoy data. During this research the spreading function proposed by Longuet-Higgins et al. [45] and Hasselman et al. [29] was used, which might lead to a wider function compared to the real situation. Poorly predicted spreading by numerical models is also shown by Stopa et al. [58].

   Another observation was that simulated ocean surfaces from the OCEANSAR simulator did not show the perfect uni-directional long-crested swell, which one would expect in a swell climate without wind waves. This was observed during the test case in Portugal from 2014-11-25, the simulated ocean surface does not show the perfect long-crested swell, but seems to impose small variations. This effect would lead to a different calculated image cross-spectrum.

4. *Can we asses spatial variations in the ocean wave field using Synthetic Aperture Radar images?*
SAR imagery provides the unique possibility to observe waves on a large spatial scale and multiple locations. Where buoy measurements provide wave data at a single point, a single SAR image provides spectral information on 200 imagettes, as shown during this thesis. Herbers et al. [33] have found that here is limited dissipation of small-amplitude swell across a continental shelf. High energy swell are more strongly attenuated, mostly due to bottom boundary processes. Hasselmann and Olbers [31] found dissipation of swell waves in the North Sea did not agree with existing formulations of bottom friction attenuation. Dissipation of swell waves also shows relationship with friction at the air-sea interface, due to white-capping and wave-wave interactions [2].

   If we want to relate observations of swell on SAR cross spectra with dissipation of those waves, we can draw a first set of conclusions. Low-amplitude swell is only limited dissipated on a shallow continental shelf, with the absence of wind [33]. Buoy observations from the case studies in the North Sea showed the swell wave height rarely exceeded 0.6 m, with an average value between 0.3 m and 0.5 m. This is considered low- amplitude swell, which would indicate bottom dissipation only plays a minor role during these cases. Due to the pixel resolution of 13 x 2.3 m of Sentinel-1 SAR images and the interference of speckle, it becomes almost impossible to observe white caps. It is possible though to measure wind speed from SAR images, which could provide an indirect link. While it was not possible to retrieve information on dissipation, SAR image cross-spectra did show a change in direction when approaching the coast, caused by depth-induced refraction of waves.

   To conclude this section, the main research question has been answered as it is possible to measure low-frequency waves in the North Sea using Synthetic Aperture Radar. SAR images lead to a better understanding of the movements of swells and provide additional information for marine activities. A combination of wave buoy data, Sentinel-1 SAR data and OCEANSAR data showed measuring swell waves is possible with this state-of-the-art remote sensing technique.

6
Recommendations

This thesis shows a promising start to measure swell waves in the North Sea, however there is much work to be done to fully benefit of this new stream of data. Results are promising, but further research is needed to fully implement the spectral retrieval algorithm. Further improvements would include the removal of non-linear contribution from cross-spectra, mapping of wave buoy measurements on quasi-linear swell spectrum, determine the effect of the look angle on the quality and intensity of the SAR spectrum. If there are further studies into the effect of white-capping, it is advised to look into remote sensing using optical sensors. The recommendations are described below.

Further implementing the spectral retrieval algorithm:
One step for future research is the implementation of the second part of the OSW algorithm, the Spectral Inversion Unit [39]. Most important steps performed in this part of the algorithm are: 1) Estimation of the Cut-Off wavelengths and Spectral resolution. 2) Estimation of wind speed and wave height using known relation with the azimuth cut-off wave length. 3) removing the non-linear part of the cross-spectrum and 4) computation of the MTF and spectral inversion. In order to perform these steps, additional information is needed. For the estimation of wind speed and wave height, ECMWF model data is needed. The modulation transfer function is described in Auxiliary files which can be downloaded from https://qc.sentinel1.eo.esa.int/. Sentinel-1_IPF_Auxiliary_Product_Specification describes these auxiliary files. Also, bathymetry data is needed during the spectral transformation to a frequency spectra, this could be provided by the available bathymetry used in the SWAN ZUNO model.

Changing sub-look width:
During this thesis, the SAR image was divided in three sub-looks. The width of each sub-look was determined as one-third of the Doppler Bandwidth ,the width of the signal in Azimuth Fourier domain. However, auxiliary data from Johnson and Collard [39], section 7 Table 3, showed different values for several sub-look parameters: the frequency separation between neighbor looks $\Delta f = 0.27 f_{PRF}[Hz]$, the Azimuth look filter width $f_y = 0.25 f_{PRF}[Hz]$ and Range look filter width $f_x = 0.78 f_{sl}[Hz]$, where PRF is the Pulse Repetition Frequency and SF the Sampling Frequency. In the implementation in this thesis no look filter was used in range direction.

Monte Carlo simulations for error estimation:
This thesis did not look into the accuracy of the retrieval algorithm. One way of checking the accuracy of the results is by using Monte Carlo simulations. The OCEANSAR simulator was now used to process different case studies, however we can also use the same case study and process this specific case study multiple times. When we make a small change e.g. in direction during each processing run and run the simulation many times, we can estimate what the average error or accuracy is.

Detrending and bright target removal:
The North Sea is known for having extremely busy shipping routes. Due to the shape and material of large marine vessels, they locally cause a very strong backscatter intensity, also known as a Bright Target. Additionally, during low-wind conditions, low-frequency (no-wave) signatures are visible on the complex images. This was observed during the case study on 2016-10-3 e.g. After the calibration step is applied and before creating different sub-looks is a step where these signatures are removed. Johnson and Collard [39] describes how detrending and bright target removal works. Detrending is performed by generating a low-pass filter of the intensity image and than reassigning the intensity image with the mean image intensity μ_I

$$I_{LP} = lowpass(\| I_c^2 \|, w_x, w_y) \tag{6.1}$$

The detrended SLC image is given by:

$$I_c := I_c \sqrt{\frac{\mu_I}{I_{LP}}} \tag{6.2}$$

According to Johnson and Collard [39] a bright target removal uses a threshold for the normalized variance to determine if a pixel contains a bright target. If this is the case, pixels values are set to equal values of the low pass filtered image, the phase remains unchanged.

$$I_c(x_i, y_i) = \sqrt{I_{LP}(x_i, y_i)} e^{j\Phi(x_i, y_i)} \tag{6.3}$$

where
(x_i, y_i) bright target pixel (range, azimuth)
Φ phase of the original complex image

Changing imagette size:
A choice was made during this thesis to use imagettes sized 1024 x 1024 pixels, due to the Fourier Transform operating best on a data set of a multiple of 2. This resulted in pixels which were approximately 13 m in azimuth direction and 2.3 m in range direction, corresponding to an image of 13 by 2.3 km. OCEANSAR was set to calculate an image with pixels of 15 m in azimuth and 5 m in range. The image size was 4 x 4 km. Cross spectra from OCEANSAR showed good similarities with SAR cross-spectra, which would indicate that indeed using a smaller imagette size would still yield good results. One factor to take into account, is that reducing the imagette size reduces the azimuth band width, which was used to create multi-looks. This means the look separation time between consecutive sub-looks becomes shorter. If the look separation time is too short, it is no longer possible to retrieve directional information. a solution could be to use a single larger imagette to resolve the direction and smaller imagettes for a larger grid.

Improving OCEANSAR results:
The pixel resolution of the OCEANSAR simulator depends in azimuth on the length of the synthetic aperture and in range on the pulse bandwidth.For the settings of OCEANSAR during this thesis, this resulted in a pixel resolution of 15 m in azimuth and 5 m in range. By playing with this settings, changing the aperture length for example, one might achieve the same resolution as the S-1 IW SLC images. Using the same resolution for both OCEANSAR and SAR images would result in a better comparison.

Azimuth cut-off wave length:
As explained in chapter 2, the azimuth cut-off wave length is an important parameter within SAR processing of the ocean. This cut-off wave length determines the wave length which can be resolved using the cross-spectral method. In literature, e.g., is is mentioned that the azimuth cut-off wave length is estimated from the cross-variance profile. The azimuth cut-off can be estimated from the profile containing the maximum pixel values in azimuth direction [59]. Figure 6.1 shows the cross-variance profile and an example of estimating the azimuth cut-off wave length from this profile.

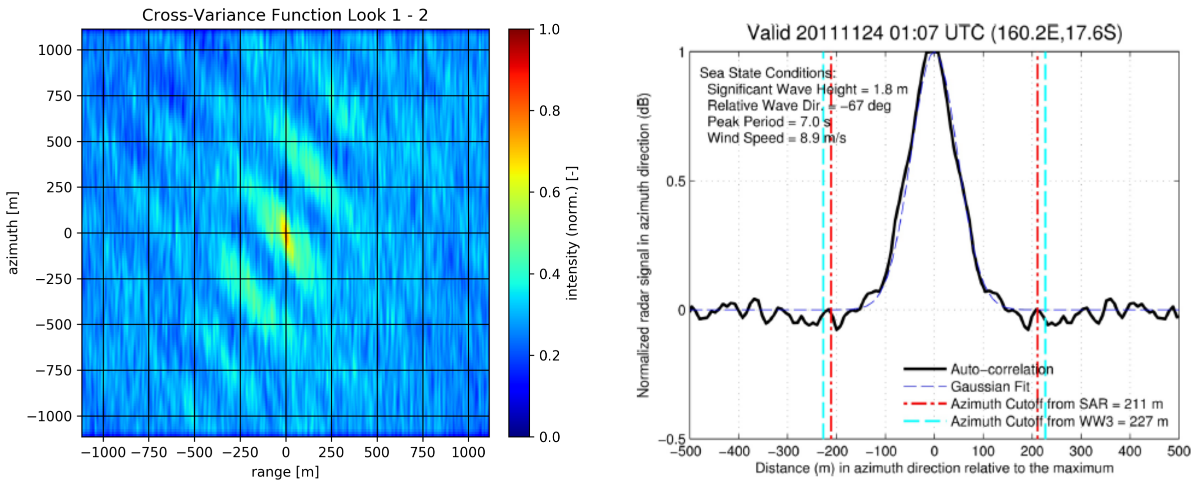

Figure 6.1: The cross-variance function resulting from an IFFT of a cross spectra (left). An example on how the azimuth cut-off wave length is estimated from the azimuth profile using a Gaussian function, from Stopa et al. [59] (right) .

The cross variance is calculated by taking the inverse FFT of the image cross-spectra. By plotting the profile at zero range, an azimuth profile os obtained from which the azimuth cut-off is estimated.

The co- and cross-variance function which was used in Figure 6.1 is given as:

$$\rho_s^{(m,n)}(k, \Delta t) = \frac{1}{(2\pi)^2} \int d\underline{k} \quad P_s^{(m,n)}(k, \Delta t) \quad e^{-ik\underline{x}} \tag{6.4}$$

with n = [1, 2, 3] and m = [1, 2, 3] and $P_s^{(m,n)}(k, \Delta t)$ the computed cross-spectra.

Bibliography

[1] Alpers, W. [1983], 'Monte carlo simulations for studying the between ocean wave and synthetic aperture radar image spectra', *Journal of Geophysical Research: Oceans* **88**(C3), 1745–1759.

[2] Ardhuin, F., Chapron, B. and Collard, F. [2009], 'Observation of swell dissipation across oceans', *Geophysical Research Letters* **36**(6).

[3] Ardhuin, F., Collard, F., Chapron, B., Queffeulou, P., Filipot, J.-F. and Hamon, M. [2008], Spectral wave dissipation based on observations: a global validation, *in* 'Proceedings of Chinese-German Joint Symposium on Hydraulics and Ocean Engineering, Darmstadt, Germany', pp. 391–400.

[4] Ardhuin, F. and Jenkins, A. D. [2005], On the effect of wind and turbulence on ocean swell, *in* 'Proceedings of The Fifteenth (2005) International Offshore and Polar Engineering Conference', pp. 429–434.

[5] Ardhuin, F., Stopa, J., Chapron, B., Collard, F., Smith, M., Thomson, J., Doble, M., Blomquist, B., Persson, O., Collins, C. O. and Wadhams, P. [2017], 'Measuring ocean waves in sea ice using SAr imagery: a quasi-deterministic approach evaluated with sentinel-1 and in situ data', *Remote Sensing of Environment* **189**(Supplement C), 211 – 222.

[6] Bao, M. and Alpers, W. [1998], 'On the cross spectrum between individual-look synthetic aperture radar images of ocean waves', *IEEE Transactions on Geoscience and Remote Sensing* **36**(3), 922–932.

[7] Barber, N. F. and Ursell, F. [1948], 'The generation and propagation of ocean waves and swell. i. wave periods and velocities', *Philosophical Transactions of the Royal Society of London A: Mathematical, Physical and Engineering Sciences* **240**(824), 527–560.

[8] Barry, M., Elema, I. and van der Molen, P. [2006], Governing the North Sea in the Netherlands: Administering marine spaces: international issues, *in* 'Frederiksberg, Denmark: International Federation of Surveyor, chapter 5s', pp. 5–17.

[9] Boerner, T., Marull-Paretas, G., Baumgartner, S., Lopez-Dekker, P., Sauer, S., Krieger, G. and D'Addio, S. [2014], Ati and gmti performance analysis of post-sentinel-1 sar systems based on simulations using oasis, *in* 'EUSAR 2014; 10th European Conference on Synthetic Aperture Radar', pp. 1–4.

[10] Cavaleri, L., Alves, J.-H., Ardhuin, F., Babanin, A., Banner, M., Belibassakis, K., Benoit, M., Donelan, M., Groeneweg, J., Herbers, T., Hwang, P., Janssen, P., Janssen, T., Lavrenov, I., Magne, R., Monbaliu, J., Onorato, M., Polnikov, V., Resio, D., Rogers, W., Sheremet, A., Smith, J. M., Tolman, H., van Vledder, G., Wolf, J. and Young, I. [2007], 'Wave modelling – the state of the art', *Progress in Oceanography* **75**(4), 603 – 674.

[11] Chapron, B., Johnsen, H. and Garello, R. [2001], 'Wave and wind retrieval from SAR images of the ocean', *Ann. Telecommun.* **56**, 682–699.

[12] Coelingh, J., van Wijk, A., Cleijne, J. and Pleune, R. [1992], 'Description of the north sea wind climate for wind energy applications', *Journal of Wind Engineering and Industrial Aerodynamics* **39**(1), 221 – 232.

[13] Collard, F., Ardhuin, F. and Chapron, B. [2005], 'Extraction of coastal ocean wave fields from SAR images', *IEEE Journal of Oceanic Engineering* **30**(3), 526–533.

[14] Collard, F., Johnsen, H., Lotfi, A. and Chapron, B. [2013], Wave Mode Processing Algorithms, Product Validation and Assimilation Wave Retrievals and Applications, *in* 'SeaSAR 2012', Vol. 709 of *ESA Special Publication*, p. 8.

[15] Cunha, P. P. and Gouveia, M. P. [2015], *The Nazaré coast, the submarine canyon and the giant waves - a synthesis*, Universidade de Coimbra.

[16] De Zan, F. and Monti Guarnieri, A. M. [2006], 'Topsar: Terrain observation by progressive scans', *IEEE Transactions on Geoscience and Remote Sensing* **44**(9), 2352–2360.

[17] Delpey, M. T., Ardhuin, F., Collard, F. and Chapron, B. [2010], 'Space - time structure of long ocean swell fields', *J. Geophys. Res.* **115**(C12037), 1–16.

[18] Drinkwater, M., Bonekamp, H., Bontempi, P., Chapron, B., Donlon, C., Fellous, J.-L., DiGiacomo, P., Harrison, E., LeTraon, P.-Y. and Wilson, S. [2009], Status and outlook for the space component of an integrated ocean observing system, *in* 'Proceedings of OceanObs'09: Sustained Ocean Observations and Information for Society', Vol. 1, p. 17.

[19] Eckart, C. [1952], The propagation of gravity waves from deep to shallow water, *in* 'Gravity Waves', p. 165.

[20] Engen, G. and Johnsen, H. [1995], 'SAR-ocean wave inversion using image cross spectra', *IEEE Transactions on Geoscience and Remote Sensing* **33**(4), 1047–1056.

[21] ESA [2007], *Envisat ASAR Product Handbook*, issue. 2.2 edn.

[22] ESA [2015], *Sentinel-1 Product Specification*, issue 3.1, 08/10/2015 edn.

[23] Fenton, J. D. [1988], 'The numerical solution of steady water wave problems', *Computers and Geosciences* **14**, 357–368.

[24] Froude, W. [1861], 'On the rolling of ships', *Transactions of the Institution of Naval Architects* **2**, 180–227.

[25] Galeazzi, R., Blanke, M. and Poulsen, N. K. [2012], Detection of parametric roll for ships, *in* T. I. Fossen and H. Nijmeijer, eds, 'Parametric Resonance in Dynamical Systems', Springer New York, New York, NY, pp. 17–43.

[26] Grandin, R. [2015], Interferometric Processing of SLC Sentinel-1 TOPS Data, *in* 'Fringe2015: Advances in the Science and Applications of SAR Interferometry and Sentinel-1 InSAR Workshop', p. 116.

[27] Grieco, G., Lin, W., Migliaccio, M., Nirchio, F. and Portabella, M. [2016], 'Dependency of the sentinel-1 azimuth wavelength cut-off on significant wave height and wind speed', *International Journal of Remote Sensing* **37**(21), 5086–5104.

[28] Hartman, D. [2016], *ATM 552 Lecture Notes Review of Statistics*.

[29] Hasselman, D. E., Dunckel, M. and Ewing, J. A. [1980], 'Directional wave spectra observed during JONSWAP 1973', *J. Phys. Oceanogr.* **10**, 1264–1280.

[30] Hasselmann, K. and Hasselmann, S. [1991], 'On the nonlinear mapping of an ocean wave spectrum into a synthetic aperture radar image spectrum and its inversion', *Journal of Geophysical Research: Oceans* **96**(C6), 10713–10729.

[31] Hasselmann, K. and Olbers, D. [1973], 'Measurements of wind-wave growth and swell decay during the joint north sea wave project (JONSWAP)', *Ergänzung zur Deut. Hydrogr. Z., Reihe A (8)* **12**, 1–95.

[32] Hasselmann, K., Raney, R. K., Plant, W. J., Alpers, W., Shuchman, R. A., Lyzenga, D. R., Rufenach, C. L. and Tucker, M. J. [1985], 'Theory of synthetic aperture radar ocean imaging: A MARSEN view', *Journal of Geophysical Research: Oceans* **90**(C3), 4659–4686.

[33] Herbers, T. H. C., Hendrickson, E. J. and O'Reilly, W. C. [2000], 'Propagation of swell across a wide continental shelf', *Journal of Geophysical Research: Oceans* **105**(C8), 19729–19737.

[34] Holthuijsen, L. H. [2007], *Waves in Oceanic and Coastal Waters*, Cambridge University Press.

[35] Husson, R., Mouche, A., Chapron, B., Johnsen, H., Collard, F., Vincent, P., Guitton, G., Longepe, N., Hajduch, G., Quilfen, Y. and Gaultier, L. [2016], Taking advantage of sentinel-1 acquisition modes to improve ocean sea state retrieval., *in* 'IAGRASS 2016', pp. 3886–3889.

[36] Jackson, C. R. and Apel, J. R. [2004], *Synthetic Aperture Radar Marine User's manual*, National Oceanic and Atmospheric Administration.

[37] Jacobsen, S. and Høgda, K. A. [1994], 'Estimation of the real aperture radar modulation transfer function directly from synthetic aperture radar ocean wave image spectra without a priori knowledge of the ocean wave height spectrum', *Journal of Geophysical Research: Oceans* **99**(C7), 14291–14302.

[38] Johnsen, H., Høgda, K. A., Guneriussen, T. and Pedersen, J. P. [1991], 'Azimuth smearing in synthetic aperture radar ocean image spectra from the norwegian continental shelf experiment of 1988', *Journal of Geophysical Research: Oceans* **96**(C6), 10443–10452.

[39] Johnson, H. and Collard, F. [2010], 'Sentinel-1 ocean swell wave spectra (osw) algorithm definition', *Norut report ISSN 1890-5226* .

[40] Kerbaol, V., Chapron, B. and Vachon, P. W. [1998], 'Analysis of ers-1/2 synthetic aperture radar wave mode imagettes', *Journal of Geophysical Research: Oceans* **103**(C4), 7833–7846.

[41] Krogstad, H. E., Samset, O. and Vachon, P. W. [1994], 'Generalizations of the non linear ocean SAR transform and a simplified SAR inversion algorithm', *Atmosphere Ocean* **32**(1), 61–82.

[42] Krogstad, H. E. and Schyberg, H. [1991], On Hasselmann's Nonlinear Ocean-SAR transformation, *in* 'Geoscience and Remote Sensing Symposium, 1991. IGARSS '91. Remote Sensing: Global Monitoring for Earth Management., International', Vol. 2, pp. 841–846.

[43] Kuik, A. J., van Vledder, G. P. and Holthuijsen, L. H. [1988], 'A Method for the Routine Analysis of Pitch-and-Roll Buoy Wave Data', *Journal of Physical Oceanography* **18**, 1020–1034.

[44] Lee, J.-S. [1981], 'Refined filtering of image noise using local statistics', *CComput. Graph. Image Process/* **15**(2), 380–389.

[45] Longuet-Higgins, M., Cartwright, D. E. and Smith, N. D. [1963], 'Observations of the directional spectrum of sea waves using the motion of a flotation buoy', *Ocean Wave Spectra* pp. 111–136.

[46] Lyons, R. [2008], *Quadrature Signals: Complex, But Not Complicated*, Essay published on 1 November 2008.

[47] Marull-Paretas, G. [2013], Development of a multi-channel sar simulator for open-oceans: Oasis, Master's thesis, Escola Tècnica Superior d'Enginyeria de Telecomunicació de Barcelonas, Deutsches Zentrum für Luft- und Raumfahrt (DLR), Linder Höhe, 51147 Köln, Germany.

[48] Massonnet, D. and Souyris., J.-C. [2008], *Imaging with Synthetic Aperture Radar*, EPFL Press.

[49] Meta, A., Prats, P., Steinbrecher, U., Scheiber, R. and Mittermaye, J. [2007], First tops interferometry results with terrasar-x, *in* 'Proc. FRINGE, Frascati, Italy'.

[50] Miles, J. W. [1957], 'On the generation of surface waves by shear flows', *Journal of Fluid Mechanics* **3**, 185–204.

[51] Miranda, N. [2015], *Technical Note: Sentinel-1 TOPS-SLC-Deramping*, esa official documents edn.

[52] Naeimi, V., Elefante, S., Cao, S., Wagner, W., Dostalova, A. and Bauer-Marschallinger, B. [2016], Geophysical parameters retrieval from Sentinel-1 SAR Data: A case study for high performance computing at EODC, *in* 'Proceedings of the 24th High Performance Computing Symposium', HPC '16, pp. 10:1–10:8.

[53] Rijkswaterstaat [2005], *Golfverwerking - Bijlage bij de RWS Standaard*, Rijkswaterstaat Meetnet Infrastructuur (RMI) Versie 1.0.

[54] Rodriguez-Cassola, M., Prats-Iraola, P., Zan, F. D., Scheiber, R., Reigber, A., Geudtner, D. and Moreira, A. [2015], 'Doppler-related distortions in TOPS SAR images', *IEEE Transactions on Geoscience and Remote Sensing* **53**(1), 25–35.

[55] Rusu, E. and Soares, C. G. [2009], 'Numerical modelling to estimate the spatial distribution of the wave energy in the Portuguese nearshore', *Renewable Energy* **34**(6), 1501 – 1516.

[56] Shao, W., Zhang, Z., Li, X. and Li, H. [2016], 'Ocean wave parameters retrieval from sentinel-1 sar imagery', *Remote Sensing* **8**(9).

[57] Snodgrass, F. E., Groves, G. W., Hasselmann, K. F., Miller, G. R., Munk, W. H. and Powers, W. H. [1966], 'Propagation of ocean swell across the pacific', *Philosophical Transactions of the Royal Society of London A: Mathematical, Physical and Engineering Sciences* **259**(1103), 431–497.

[58] Stopa, J. E., Ardhuin, F., Babanin, A. and Zieger, S. [2016], 'Comparison and validation of physical wave parameterizations in spectral wave models', *Ocean Modelling* **103**, 2 – 17.

[59] Stopa, J. E., Ardhuin, F., Chapron, B. and Collard, F. [2015], 'Estimating wave orbital velocity through the azimuth cutoff from space-borne satellites', *Journal of Geophysical Research: Oceans* **120**(11), 7616–7634.

[60] Tolman, H. L. and Nooij, N. [1998], 'Modeling wind waves using wavenumber-direction spectra and a variable wavenumber grid', *The Global Atmosphere and Ocean System* **6**, 295–309.

[61] Torres, R., Snoeij, P., Geudtner, D., Bibby, D., Davidson, M., Attema, E., Potin, P., Rommen, B., Floury, N., Brown, M., Traver, I. N., Deghaye, P., Duesmann, B., Rosich, B., Miranda, N., Bruno, C., L'Abbate, M., Croci, R., Pietropaolo, A., Huchler, M. and Rostan, F. [2012], 'GMES sentinel-1 mission', *Remote Sensing of Environment* **120**, 9 – 24.

[62] Traon, P.-Y. L., Antoine, D., Bentamy, A., Bonekamp, H., Breivik, L., Chapron, B., Corlett, G., Dibarboure, G., DiGiacomo, P., Donlon, C., Faugère, Y., Font, J., Girard-Ardhuin, F., Gohin, F., Johannessen, J., Kamachi, M., Lagerloef, G., Lambin, J., Larnicol, G., Borgne, P. L., Leuliette, E., Lindstrom, E., Martin, M., Maturi, E., Miller, L., Mingsen, L., Morrow, R., Reul, N., Rio, M., Roquet, H., Santoleri, R. and Wilkin, J. [2015], 'Use of satellite observations for operational oceanography: recent achievements and future prospects', *Journal of Operational Oceanography* **8**(sup1), s12–s27.

[63] Vachon, P. W. and West, J. C. [1992], 'Spectral estimation techniques for multilook sar images of ocean waves', *IEEE Transactions on Geoscience and Remote Sensing* **30**(3), 568–577.

[64] Van Bussel, G. and Bierbooms, W. [2003], Analysis of different means of transport in the operation and maintenance strategy for the reference DOWEC offshore wind farm, *in* 'OWEMES offshore wind energy Seminar, 10-12 April 2003, Naples, Italy'.

[65] Van Vledder, G. P., Hulst, S. T. C. and McConochie, J. D. [2016], 'Source term balance in a severe storm in the Southern North Sea', *Ocean Dynamics* **66**(12), 1681–1697.

[66] Verlaan, M. and Heemink, A. [1996], 'Data assimilation schemes for non-linear shallow water flow models', *Transactions on Engineering Sciences* **9**, 1–10.

[67] Willis, M. C., Devaliere, E., Hanson, J., Hawkins, R., Lewitsky, J., King, D., Nicolini, T., Tjaden, S., Morgan, C., Schumann, S. and andand John Elardo, M. C. [2009], Implementing the swan wave model at three east coast national weather service offices, *in* '14th Symposium on Integrated Observing and Assimilation System for the Atmosphere, Oceans and Land Surface (IOAS-AOLS)'.

[68] Zuhlke, M., Fomferra, N., Brockmann, C., Peters, M., Veci, L., Malik, J. and Regner, P. [2015], SNAP (Sentinel Application Platform) and the ESA Sentinel 3 Toolbox, *in* 'Sentinel-3 for Science Workshop', Vol. 734, p. 21.

A

Auxiliary information and methodology

This Appendix provides additional information on case studies, as well as extra information on the proposed methodology. It consists of the following sections:

Auxiliary information:

- Download locations
- North Sea bathymetry
- Wave buoy locations
- Sentinel-1 SLC image information
- Hydrodynamic conditions

Methodology:

- Sentinel-1 Ocean Swell Wave Spectral retrieval algorithm
- OCEANSAR settings
- Wave buoy spectral partitioning
- Transformation from $f-\theta$ to $kx-ky$ spectrum.

Download locations

Sentinel-1 SAR imagery was downloaded from the Sentinel Scihub using a GeoJSON file, which describes a geographic bounding box. When (part of) a S-1 IW SLC image would fall within this bounding box and matched hydrodynamic criteria it was selected as a match. The selected bounding box is a square of 20km x 20km surrounding the K13 wave buoy, see Figure A.1

buoy	**Coordinates**
K13	3.0693230536779343, 53.1282854341859
	3.3687489463220657, 53.1282854341859
	3.3693782163291326, 53.3079485658141
	3.0686937836708674, 53.3079485658141

Table A.1: Coordinates of the bounding box surrounding the K13 wave buoy

Figure A.1: GeoJSON location, the top bounding box represents the K13 buoy, the lower box the IJ-geul munitiestort buoy.

North Sea Bathymetry

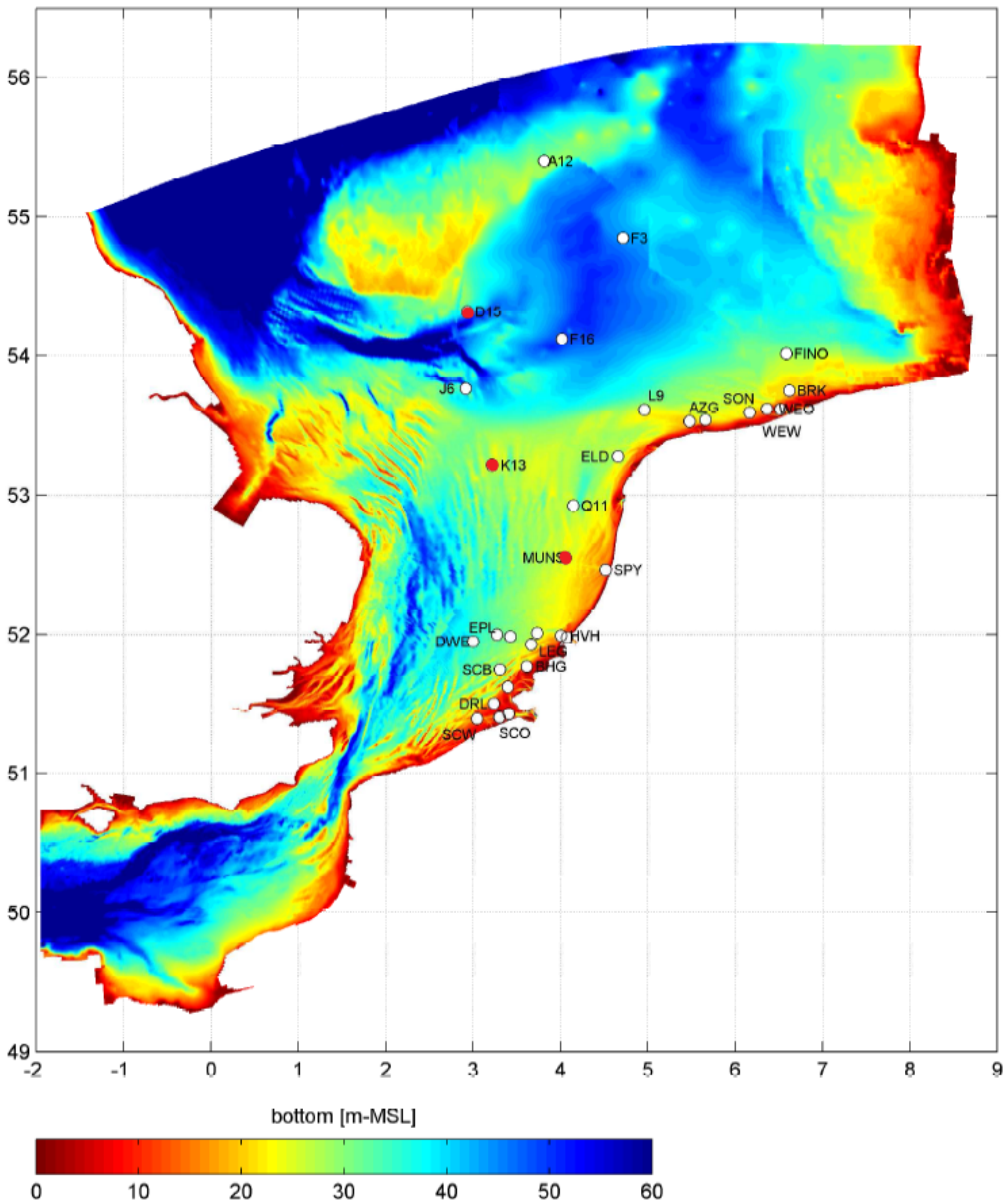

Figure A.2: North Sea bathymetry in meters below sea level. Domain and selection of output locations of the SWAN-ZUNO grid. Source: Deltares document no. 1209448-004-ZKS-0004, figure: B2.2.

Wave buoy locations

North Sea

Validation wave data in the North Sea was used from several different wave buoys.

buoy	**Coordinates**	**Usage**
K13-alpha	3.219036 53.2181172	Selecting data: wave data was used to make a selection of low-wind/high-swell events Location: buoy location used to select area where SAR images are downloaded from Validation: hydrodynamic conditions, such as wind and wave information from Matroos Spectral data: 1D and 2D wave spectra were used as validation of SAR spectra, before 2016-01-01
IJgeul munitiestort	4.079319 52.567568	Spectral data: 1D and 2D wave spectra were used as validation of SAR spectra between 2016-12-01 and 2016-12-31
A121 Aukfield	3.816671 55.416663	Spectral data: 1D and 2D wave spectra were used as validation of SAR spectra after 2016-12-31

Table A.2: Wave buoy and their use during this research.

	K13 Alpha	IJmuiden munitiestort	Monican 1	Monican 2
Type	WaveRider	WaveRider	OCEANOR	OCEANOR
Location	NED	NED	POR	POR
Coordinates				
Data provider	RWS	RWS	IH	IH
Units	cm^2	cm^2	m^2	m^2
Remarks				

Table A.3: Wave buoys used during this thesis. In Portugal OCEANOR WaveSense buoys were used, where data was provided by Instituto Hidrografico (IH). In the North Sea, Waverider buoys measured data, data was provided by Rijkswaterstaat (RWS)

Portugal

buoy	Coordinates	Usage
Monican 1	-9.648 39.522	Spectral data: 1D and 2D wave spectra were used as validation of SAR spectra Hydrodynamic conditions. Buoy data used to measure hydrodynamic conditions.
Monican 2	-9.208 39.569	Spectral wave data, if there was no buoy data available from Monican 1

Table A.4: Wave buoys in Portugal.

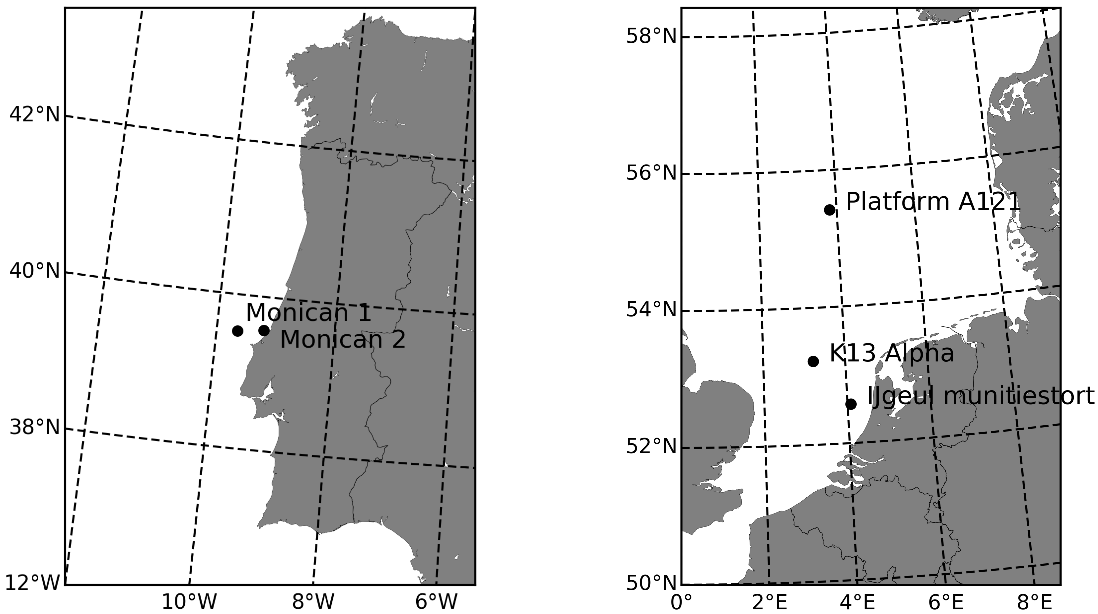

Figure A.3: Wave buoy locations near the Portugal coast (left) and the North Sea (right).

Sentinel-1 SLC auxiliary information

Additional information, such as:

- - List of satellite images
- - meta data
- - hydrodynamic conditions

Selected images

Portugal
S1A_IW_SLC__1SDV_20141125T183457_20141125T183524_003442_00405B_3F04
S1A_IW_SLC__1SDV_20150124T183456_20150124T183523_004317_005429_AB1E
S1A_IW_SLC__1SDV_20151027T183506_20151027T183534_008342_00BC5A_FFF0

North Sea
S1A_IW_SLC__1SDV_20150426T173313_20150426T173340_005658_00741A_8482
S1A_IW_SLC__1SDV_20160519T174144_20160519T174211_011331_01130E_67C7
S1B_IW_SLC__1SDV_20161001T060450_20161001T060517_002309_003E77_4C91
S1B_IW_SLC__1SDV_20161030T172453_20161030T172520_002739_004A26_0CD2
S1A_IW_SLC__1SDV_20161129T172515_20161129T172542_014160_016DE6_FF92
S1B_IW_SLC__1SDV_20170108T174048_20170108T174122_003760_006763_D13A
S1A_IW_SLC__1SDV_20170109T173346_20170109T173413_014758_01806B_C00F
S1A_IW_SLC__1SDV_20170116T172537_20170116T172604_014860_0183A6_43C2
S1A_IW_SLC__1SDV_20170121T173321_20170121T173348_014933_0185EA_24EF

Table A.5: An overview of Sentinel-1 A/B Interferometric Wide Swath (IW), Single Look Complex (SLC) images used during this thesis. Three images were selected along the Portugal coast and 11 images on the North Sea.

Satellite meta-data

File	date	swath	orbit	lat	lon	heading
S1A_20150426T173313	2015-04-26	IW2	Ascending	53.73	3.19	349.86
S1A_20160519T174119	2016-05-19	IW3	Ascending	53.02	2.59	350.88
S1B_20161001T060515	2016-10-01	IW1	Descending	53.273	3.440	11.167
S1B_20161030T172429	2016-10-30	IW1	Ascending	53.484	3.979	348.796
S1A_20161031T060557	2016-10-31	IW1	Descending	53.27	3.43	11.16
S1A_20161129T172515	2016-11-29	IW1	Ascending	53.648	3.932	348.79
S1B_20161210T173232	2016-12-10	IW2	Ascending	53.066	3.384	349.889
S1B_20170108T174048	2017-01-08	IW3	Ascending	53.602	2.432	350.866
S1A_20170109T173321	2017-01-09	IW2	Ascending	53.624	3.244	349.87
S1A_20170116T172512	2017-01-16	IW1	Ascending	53.649	3.931	348.79
S1A_20170121T173321	2017-01-21	IW2	Ascending	53.564	3.242	349.869

Table A.6: Meta data of Sentinel-1 images used during the North Sea test cases.

File	date	swath	orbit	lat	lon	heading
S1A_20141125T183457	2014-11-25	IW2	Ascending	38.9494	-9.479	349.998
S1A_20150124T183456	2015-01-24	IW2	Ascending	38.9497	-9.480	349.997
S1A_20151027T183506	2015-10-27	IW2	Ascending	39.115	-9.507	350.007

Table A.7: Meta data of Sentinel-1 images used during the Portugal test cases.

Hydrodynamic conditions

North Sea

Hydrodynamic conditions, source was the Platform K13-a buoy in the North Sea, obtained via the Matroos database. Sampling interval is every 10 minutes, points which fall in between are selected using nearest neighbour method.

File	hm0	swell hm0	period Tp	wind speed	wind dir [deg]
S1A_20150426T173313	1.1100 m	0.6000 m	11.1111	4.0200 m/s	345.6000
S1A_20160519T174119	0.7100 m	0.3600 m	11.1111 s	8.2400 m/s	193.9000
S1B_20161001T060515	1.1200 m	0.2200 m	5.0000 s	2.7500 m/s	159.6000
S1B_20161030T172429	1.0400 m	0.6200 m	11.1111 s	0.8200 m/s	320.4000
S1A_20161031T060557	0.7200 m	0.3100 m	11.1111 s	2.4600 m/s	197.5000
S1A_20161129T172515	0.7500 m	0.2400 m	10.0000 s	7.1400 m/s	261.6000
S1B_20161210T173232	0.8200 m	0.2700 m	5.5556 s	6.7100 m/s	240.8000
S1B_20170108T174048	0.8900 m	0.4800 m	14.2857 s	3.3200 m/s	222.1000
S1A_20170109T173321	2.1300 m	0.3000 m	6.2500 s	13.3700 m/s	216.5000
S1A_20170116T172512	0.9400 m	0.5800 m	14.285 s	3.7300 m/s	134.3000
S1A_20170121T173321	0.7900 m	0.3400 m	11.1111 s	5.1600 m/s	100.6000

Table A.8: Hydrodynamic conditions during SAR images taken from the North Sea.

Portugal

Hydrodynamic conditions near the Portugal coast were obtained using the Monican 1 wave buoy. Graphs of daily measurements were obtained via http://monican.hidrografico.pt/en/default/monican.php and can be viewed in Appendix Appendix C. Table A.9 shows an overview of the data retrieved from these daily graphs.

File	hm0	period Tp	wave dir. [deg]	wind speed	wind dir. [deg]
S1A_20141125T183457	2.05 m	17.28 s	316.7	5.05 m/s	294.7
S1A_20150124T183456	1.72 m	10.88 s	346.6	8.43 m/s	25.8
S1A_20151027T183506	4.92 m	15.84 s	312.1	7.97 m/s	238.3

Table A.9: Hydrodynamic conditions during SAR images taken from Portugal.

Methodology

This Appendix provides information on the used methodology and algorithms. It contains additional information on:

- Sentinel-1 Ocean Swell Wave Spectral retrieval algorithm
- OCEANSAR configuration file
- Wave buoy spectral partitioning
- Transformation from $f-\theta$ to $kx-ky$ spectrum.

Sentinel-1 L2 OSW algorithm

This section describes the Sentinel-1 Ocean Swell Wave (OSW) algorithm, which is used by ESA's Internal Processing Facility (IPF) to calculate the ocean wave spectra from Sentinel-1 SAR imagery. A general outline of the algorithm is provided in Figure A.4 and exists of two parts, a Spectral Estimation Unit (further elaborated in Figure A.5) and a Spectral Inversion Unit (Figure A.6). During this thesis the Spectral Estimation Unit was implemented on S-1 IW SLC images, the Spectral Inversion Unit is only partially implemented in this thesis. An overview of the complete algorithm is provided in Johnson and Collard [39].

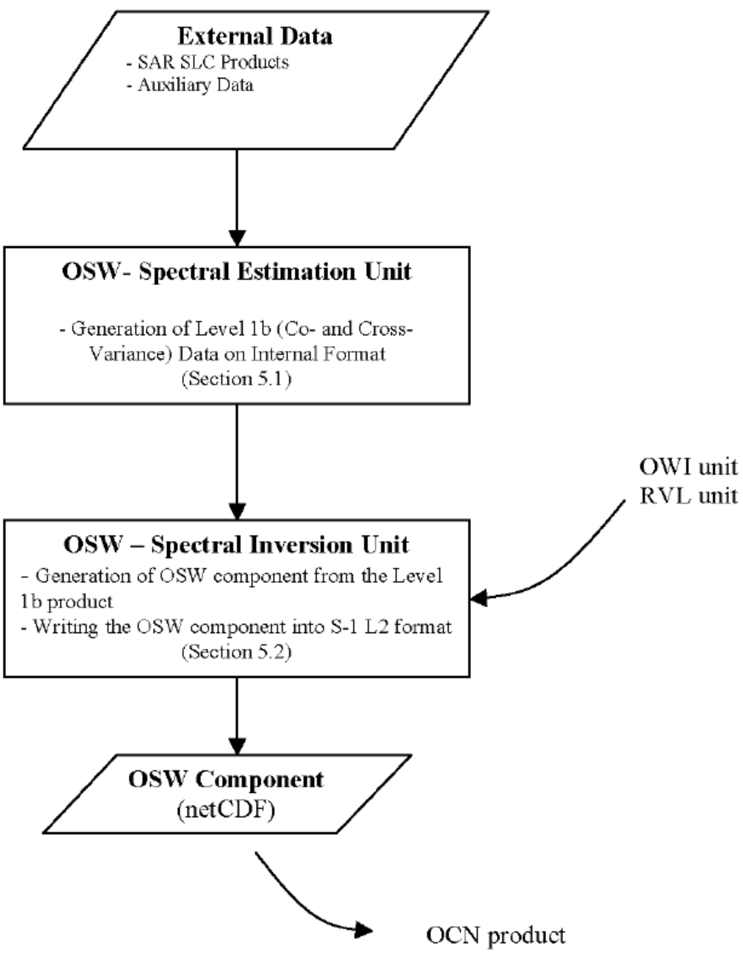

Figure A.4: Ocean Swell Wave (OSW) algorithm, a complete overview of the algorithm from SLC image to swell spectra [39].

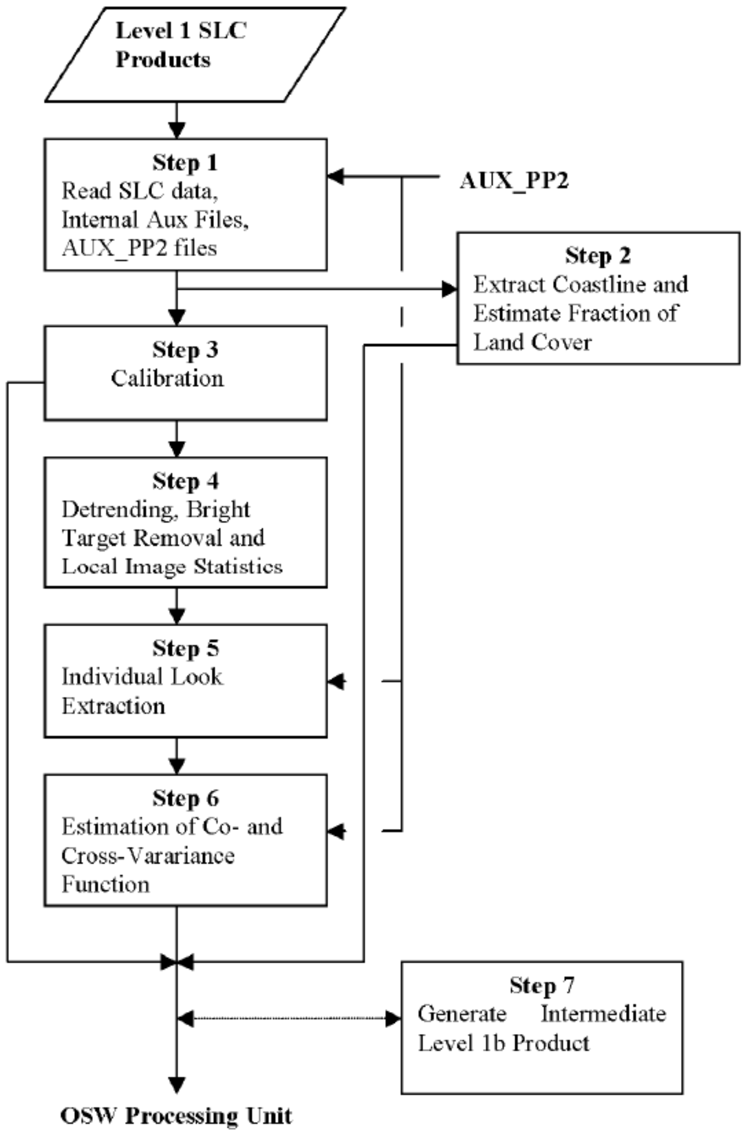

Figure A.5: OSW Spectral Estimation Unit [39], which describes steps to extract individual looks and cross spectra from the SLC image.

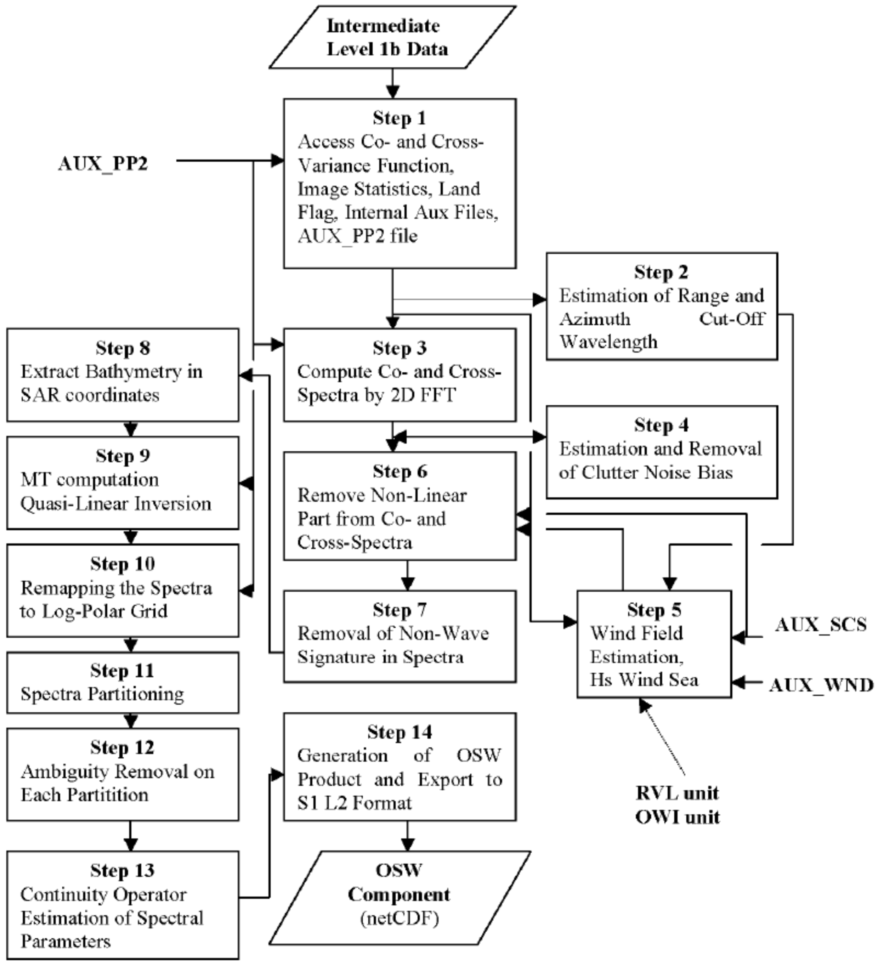

Figure A.6: OSW Spectral Inversion Unit [39]. This part of the algorithm calculates the ocean wave spectrum from SLC cross-spectra and auxiliary wind and wave information.

Decibel scale

Formula used to calculate the intensity of a SLC image in decibel. Where σ^0 is the radiometric backscatter of the image.

$$\sigma^0_{db} = 10.\log_{10}\sigma^0 \tag{A.1}$$

OCEANSAR settings

OCEANSAR uses two files as input, this section gives an overview of parameters which can be adjusted and shows an example configuration file. The first file used by OCEANSAR, is a file containing wave data, with a value for energy density, direction and spreading per frequency bin. The second file is a configuration file, containing meta-data and different settings.

Wave data file

Filename: spectra_20150426.npz

0.030	0.035	0.045	...	0.475	0.485	0.495
0.001	0.002	0.004	...	0.005	0.006	0.007
11.000	333.000	326.000	...	67.000	41.000	22.000
76.000	64.000	64.000	...	67.000	56.000	56.000

Table A.10: Example wave data file from 2015-04-26. First row are frequency bins. Second row, values of variance energy density. Third row, mean direction of the waves and fourth row, mean spreading of the waves.

OCEANSAR configuration file

Filename: 20150426_NOS.cfg

```
# This is an example parameter file needed by some example
# code or some higher level functions.
[sim]
path=D:\data\images\oceansar\20150426\
raw_run=True
raw_file=raw_data.nc
ocean_file=ocean.nc
ocean_reuse=False
errors_file=errors.nc
errors_reuse=False
proc_run=True
proc_file=proc_data.nc
ati_run=True
ati_file=ati_data.txt
mpi_exec=mpiexec
mpi_num_proc=4
corar_run=False

[sar]
f0=5.4e9
inc_angle=30.
pol=vv
prf=450.
rg_bw=50e6
over_fs=1.1
squint=0
alt=693e3
# auto for orbit height, set some value for airborne
v_ground=auto
# Heading East of North
heading=11.2
ascending=True
ant_L=40
L_total=True
Spacing=2
```

```
num_ch=1
use_errors=False
sigma_n_tx=0.12
phase_n_tx=2.3
sigma_beta_tx=0.2
phase_beta_tx=0.2
sigma_n_rx=0.04
phase_n_rx=0.2
sigma_beta_rx=0.04
phase_beta_rx=0.2



[ocean]
Lx=4096.
Ly=4096.
dx=2
dy=2
opt_res=True
dt=0.05
depth=25
wind_dir=0.
wind_U=4.
wind_fetch=500e3
swell_enable=False
swell_wl=80
swell_dir=45
swell_ampl=0.5
spec_model=elfouhaily
spread_model=elfouhaily
cutoff_wl=auto
current_mag=1.0
current_dir=90.
dt=0.05
fft_max_prime=3
choppy_enable=True
# Use buoy data instead of theoretical model
use_buoy_data=True
# If true then the rest will be read
buoy_data_file=d:\data\buoy\OCEANSAR\spectra_20150426.npz
year=2015
month=04
day=26
# To be clarified if these are UTC or local
hour=17
minute=33


[srg]
use_hmtf=True
nesz=-30.
wh_tol=5.
scat_spec_enable=True
scat_spec_mode=spa
scat_bragg_enable=True
scat_bragg_model=romeiser97
```

```
scat_bragg_spec=elfouhaily
scat_bragg_spread=romeiser97
scat_bragg_d=0.25

[processing]
az_weighting=0.8
doppler_bw=350.
plot_format=png
plot_tex=False
plot_save=True
plot_path=processing_plots/
plot_raw=False
plot_rcmc_dopp=False
plot_rcmc_time=False
plot_image_valid=True

[ati]
rg_ml=8
az_ml=2
# Multi look window: hanning, hamming, flat
ml_win=hanning
plot_save=True
plot_path=ati_plots/
plot_format=png
plot_tex=False
plot_surface=True
plot_proc_ampl=True
plot_coh=True
plot_coh_all=True
plot_ati_phase=True
plot_ati_phase_all=True
plot_vel_hist=True
plot_vel=False

[utils_nrcs]
realizations=5
inc_range=30
inc_steps=16
pol_vv=True
pol_hh=True
model_spec_ka_fa=False
model_spec_ka_spa=False
model_spec_kodis=False
model_spec_reference=True
model_bragg_r97=True
model_bragg_r97_spec=romeiser97
model_bragg_r97_spread=romeiser97
model_bragg_r97_d=0.25
plot_path=D:\OASIS\NRCS\test2
plot_format=svg
plot_tex=False
plot_total=False

[utils_anim]
dummy=True
```

Wave buoy spectral calculations

Wave data in the North Sea was gathered using a Waverider wave buoy. A value for the energy density, direction and directional spreading was measured per frequency band. The formulas in this section were described in the document "Golfverwerking - Bijlage bij de RWS standaard" [53], but are also described in Kuik et al. [43].

Frequency bands

The waverider buoy in the north sea provided spectral wave data with 48 frequency bands, ranging from 0.03 - 0.5. Bin size of each frequency band is described below.

f_1 [Hz]	f_2 [Hz]	Δf [Hz]
0.03	0.035	0.005
0.035	0.045	0.01
0.045	0.055	0.01
...	...	...
0.475	0.485	0.01
0.485	0.495	0.01
0.495	0.5	0.005

Table A.11: Frequency bins of the North Sea Waverider buoys.

Fourier Coefficients

The North Sea buoy data provided per frequency band a value for the variance density, mean direction and directional spreading. Rijkswaterstaat [53] describes how each value is calculated.

The first four Fourier-coefficients are derived from the auto-spectra C_{xx}, co-spectra C_{xy} and quad-spectra Q_i, these coefficients are used to calculate the mean direction, spreading, kurtosis and skewness of the wave spectrum. For a full derivation of the auto-, co- and quad-spectra we refer to Rijkswaterstaat [53].

$$A_1(f) = \frac{Q_{zx}(f)}{W(f)C_{zz}(f)} \tag{A.2}$$

$$A_2(f) = \frac{C_{xx}(f) - C_{yy}(f)}{C_{xx}(f) + C_{yy}(f)} \tag{A.3}$$

$$B_1(f) = \frac{Q_{zy}(f)}{W(f)C_{zz}(f)} \tag{A.4}$$

$$B_2(f) = \frac{2C_{xy}(f)}{C_{xx}(f) + C_{yy}(f)} \tag{A.5}$$

Where $W(f)$ is the wave-number. Additionally, the first order moment is required to calculate spreading and direction, which is defined as:

$$m_1(f) = \sqrt{(A_1(f))^2 + (B_1(f))^2} \tag{A.6}$$

Mean direction

According to nautical convention, the mean wave direction is the direction where waves are moving towards the sensor, where 0 ° is considered waves coming from North and 90 ° waves coming from East. The mean wave direction can be calculated from the Fourier coefficients and is given in degrees.

$$\bar{\theta}_0(f) = \sin^{-1}\left(\frac{-A_1(f)}{m_1(f)}\right) \tag{A.7}$$

Directional spreading

The mean directional spreading is calculated from the Fourier coefficients and the first order moment and is given in degrees.

$$\bar{\sigma} = \sqrt{2(1 - \bar{m}_1)} \tag{A.8}$$

Calculation of the wave number spectra

First the spectrum was transformed from a frequency variance density spectrum to a wavenumber variance density spectrum using the formulations found in [34], ignoring the directional spreading. A value for the variance density was provided for 48 discrete bins (see Table A.11), where per bin:

$$E(f_i) = \frac{1}{\Delta f} E\{\frac{1}{2}a^2\} \tag{A.9}$$

And the total energy of the variance density spectrum is equal to:

$$E_{tot} = \sum_{i}^{i=48} E(f_i) * \Delta f_i \tag{A.10}$$

First we transform the frequency spectrum into a radial frequency spectrum using the known relation for $\omega_i = 2\pi f_i$ (according to Holthuijsen [34], page 45). For the total energy we find:

$$E_{tot}(\omega) = \frac{1}{2\pi} E_{tot}(f) \tag{A.11}$$

The next step is transforming the radial-frequency spectrum into a wave number spectrum E(k), by calculating the wavenumber k for each ω_i.

The wave number k is calculated using the known dispersion relation for waves: Equation A.12. In which g, the gravitational acceleration $g = 9.81 m/s^2$ and water depth d equals the water depth at the location of the wave buoy. The water depth was derived from bathymetry data and equals 26.6 m for the K13 buoy.

$$\omega^2 = gk\tanh(kd) \tag{A.12}$$

Eckart [19] provides an explicit expression which approximates the solution of the dispersion equation.

$$kd \approx \alpha(tanh(\alpha))^{-1/2} \qquad with \quad \alpha = k_0 d = \omega^2 d/g \tag{A.13}$$

The approximation was refined by Fenton [23], this equation is used to calculate kd during this thesis.

$$kd \approx \frac{\alpha + \beta^2(cosh\beta)^{-2}}{tanh\beta + \beta(cosh\beta)^{-2}} \qquad with \quad \beta = \alpha(tanh(\alpha))^{-1/2} \tag{A.14}$$

Using Equation A.14, kd is calculated for every radial frequency ω_i and divided by water depth d to obtain the wave number k for every i. Tolman and Nooij [60] mentioned when a component of a wave field travels from deep to shallow water it undergoes large kinematic variations. These kinematic variations compress the wave field in k-space resulting in an effective loss of resolution in shallow water. Where the bin size was constant for f and ω, this is no longer the case for k. To solve this discrepancy. The variance density spectrum is interpolated on a new grid with constant bin size $\delta k = 0.001$ from $0.015 - 0.999$ and 985 bins using linear interpolation. The total energy of the spectrum was found to vary slightly compared to the original spectrum with an error in the order of 0.06 percent.

The total energy of the spectrum is calculated using:

$$E(k_i) = E(\omega_i)\frac{\Delta\omega_i}{\Delta k_i} \tag{A.15}$$

for every i and:

$$E_{tot}(k) = \sum_{i}^{i=985} E(k)_i * \Delta k_i \tag{A.16}$$

Until now, we assumed a 2D spectrum with a single value for direction. Directional spreading of the variance density spectrum is applied using the method proposed by Kuik et al. [43]. Which used the two-parameter model suggested by Longuet-Higgins et al. [45]:

$$D(\theta) = Acos^{2s}((\theta - \alpha_0)/2) \tag{A.17}$$

in which α_0 is the mean wave direction, s is a parameter which controls the directional width and A is a normalization constant. Since no information on the skewness γ was provided, we assume a symmetrical model with skewness γ is zero. According to Kuik et al. [43], the directional width is equal to:

$$\sigma = \left(\frac{2}{s+1}\right)^{1/2} \tag{A.18}$$

A value for σ was provided per frequency bin, which allows us to calculate the directional width parameter s. Directional spreading is applied with 360 bins which range from $0-2\pi$ with a bin size of $\Delta\theta = 2\pi/360$

$$E(k_i,\theta_j) = E(k_i)\frac{2\pi}{360} \tag{A.19}$$

and the total energy is equal to:

$$E_{tot} = \sum_{i}^{i=985}\sum_{j}^{j=360} E(k,\theta)_{i,j}\Delta k\Delta\theta \tag{A.20}$$

The next step is calculating kx and ky for every point (i,j). we calculate the imaginary number c, with:

$$c = k\exp^{-i\theta} \tag{A.21}$$

in which the wavenumber k is the wavenumber found at the middle of each bin. . Now we can compute $kx = Re(c)$ and $ky = Im(c)$.

The derivation of the Jacobian is described below. Using this Jacobian we can now compute the new variance density per bin with:

$$E(k_x,k_y) = E(k_i,\theta)J = E(k_i,\theta)/k \tag{A.22}$$

where k_i is the average wavenumber per bin i, calculated with $k_i = k1_i + \Delta k_i/2$ and $k1_i$ is the wavenumber at the start of each bin.

the total energy is now equal to the sum of the energy density per bin $E(k_x,k_y)$ times the size of each bin which is ΔA

$$E_{tot}(k_x,k_y) = \sum_{i}^{i=985*360} E(k_x,k_y)_i(\Delta k_x\Delta k_y) = \sum_{i}^{i=985*360} E(k_x,k_y)_i\Delta A \tag{A.23}$$

Jacobian
Below is the derivation of the Jacobian, based on the assumption that $dk_x dk_y = dA = kdkd\theta$.

$$\Delta A = \pi r^2 \frac{\Delta\theta}{2\pi} \tag{A.24}$$

$$\Delta A = \frac{\Delta\theta}{2} r^2 \tag{A.25}$$

$$\Delta A = \frac{\Delta\theta}{2}(k_1^2 - k_2^2) \tag{A.26}$$

Where

$$k_1 = k + \frac{\Delta k}{2} \tag{A.27}$$

$$k_2 = k - \frac{\Delta k}{2} \tag{A.28}$$

So

$$k_1^2 = k^2 + k\Delta k + \frac{\Delta k^2}{4} \tag{A.29}$$

$$\Delta A = \frac{\Delta\theta}{2}(2k\Delta k) = k\Delta k\Delta\theta \tag{A.30}$$

Now we can compute the Jacobian by normalizing the total energy and dividing trough the new area:

$$J = \frac{\Delta k \Delta\theta}{\Delta A} = \frac{\Delta k \Delta\theta}{k\Delta k\Delta\theta} = \frac{1}{k} \tag{A.31}$$

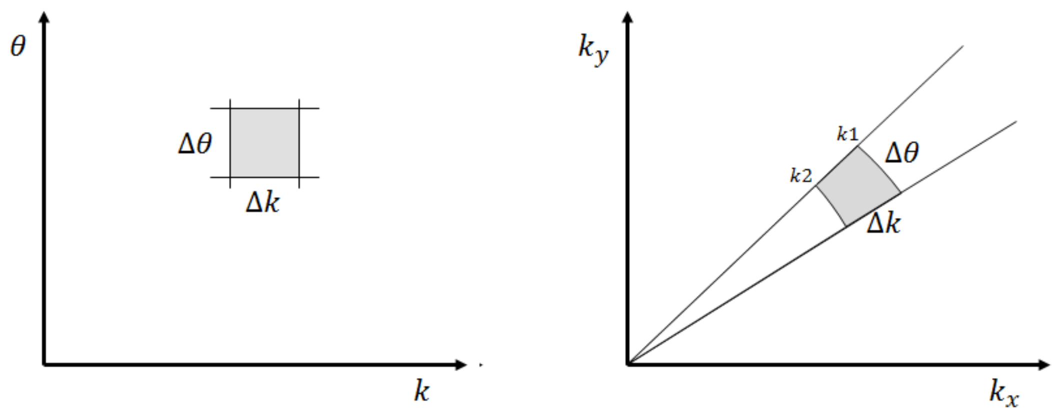

Figure A.7: Representation in Cartesian and polar coordinates

B Case studies

Comments:

- Test cases are presented in chronological order.
- At the top of each test case meta information is presented. Latitude and longitude are the calculated mean from the meta-data georeference points, heading is also calculated using the georeference points and is the angle from North in clockwise direction. e.g. an angle of 315 degrees is North-West direction, 90 degrees is East direction.
- Hydrodynamic conditions provided at the top of each test case were retrieved from Matroos from the K13-alpha buoy.
- Different wave buoys have been used as a source of spectral wave data. Before 2016-12-01 data from the K13-alpha buoy was used. Between 2016-12-01 and 2016-12-31 data from the IJ-geul stortplaats and after 2016-12-31, buoy data from the AUK A12 wave buoy was used. On 2016-10-01 and 2016-10-30 data from a different time stamp (0.5 - 2 hours later) was used, due to missing data.

Test cases: North Sea

Test case 2015-04-26

- Positive result, Swell peak visible on SAR image corresponding around ky=0.005 and kx -0.005 to 0, corresponding to swell peak from buoy measurements
- Buoy observations show significant swell (0.60 m) with a period of 11 seconds (kx 0.005) from NNW direction. Mild wind conditions 4 m/s from NW direction.
- SAR image spectra show a peak at the same wave number, peak of the spectrum is elongated in range direction on the SAR spectrum
- 1D image spectra show a corresponding peak, however the peak of the SAR spectrum seams to be flattened"
- The SAR spectra shows some noise / distortions in the higher frequency / wave number domain
- SAR SLC image shows an area with a higher variance, which would indicate a higher wind speed (wind gust), where spectral retrieval is more difficult
- SAR spectrum does not show any omni-directional spreading. What spreading function is used and is this the correct one?

Swell from NW direction was measured on this day, with a hm0 of 0.60 m and a period of 11 seconds. A light wind was blowing, from NNW direction. First results show a good comparison with wave buoy data. Due to the significant height of the swell, it showed a good comparison. The SAR image however, does not show a clear signal. This is most likely due to the presence of wind. Both show a peak at..

File	S1A_20150426T173313			
date 2015-04-26	swath IW2	orbit Ascending	lat - lon 53.73, 3.19	heading 349.86 deg
hm0 1.11 m	swell hm0 0.60 m	period Tp 11.11 s	wind speed 4.02 m/s	wind direction 345.6 deg

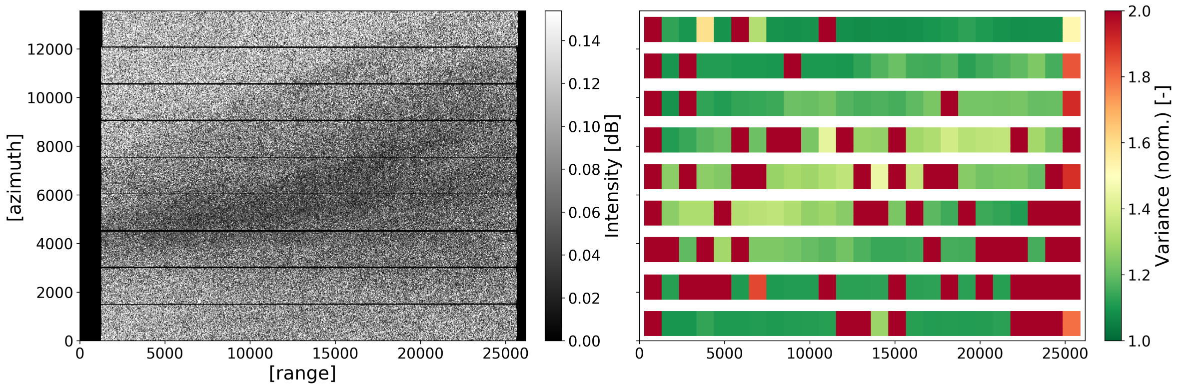

Figure B.1: Sentinel-1 SLC SAR image, acquired on 2015-04-26 17:33:13. Top left image shows the intensity (absolute) values of the 2nd sub-swath. Top right shows computed variance per 1024x1024 imagette of the same sub-swath.

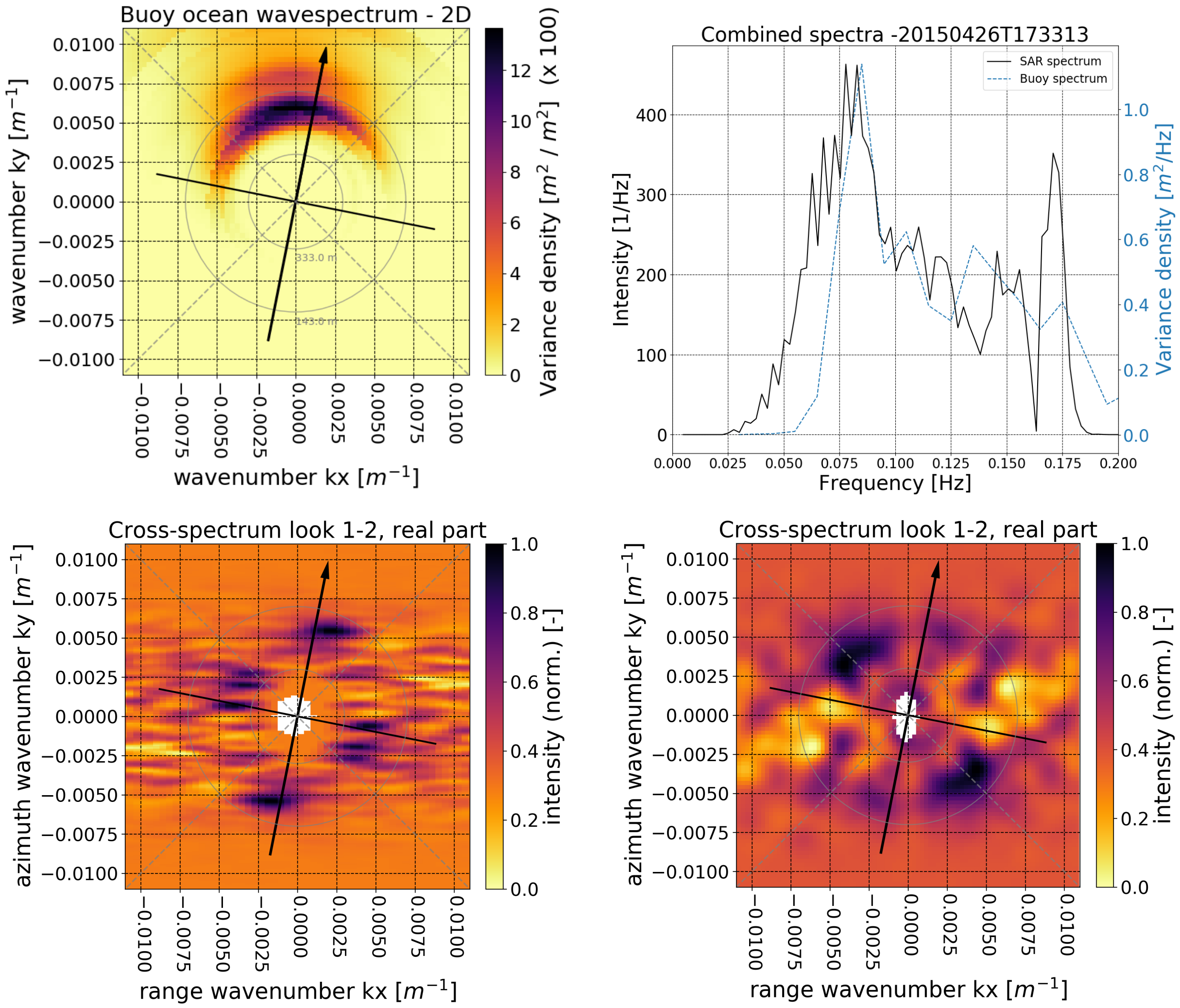

Figure B.2: The top left image shows K13-alpha buoy spectra, top right shows 1D buoy and SAR spectra from 26 April 2015. Bottom images show SAR image spectra (left) and OCEANSAR image spectra (right), between sub-look 1 and sub-look 2.

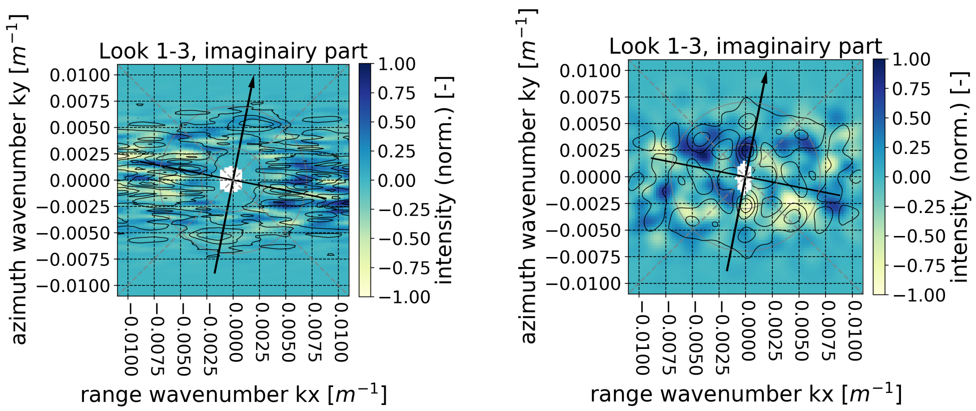

Figure B.3: Imaginary part of the cross spectrum between sub-look 1 and sub-look 3, contour lines show the real part of the cross spectrum. SAR image spectrum is plotted on the left and OCEANSAR spectrum on the right.

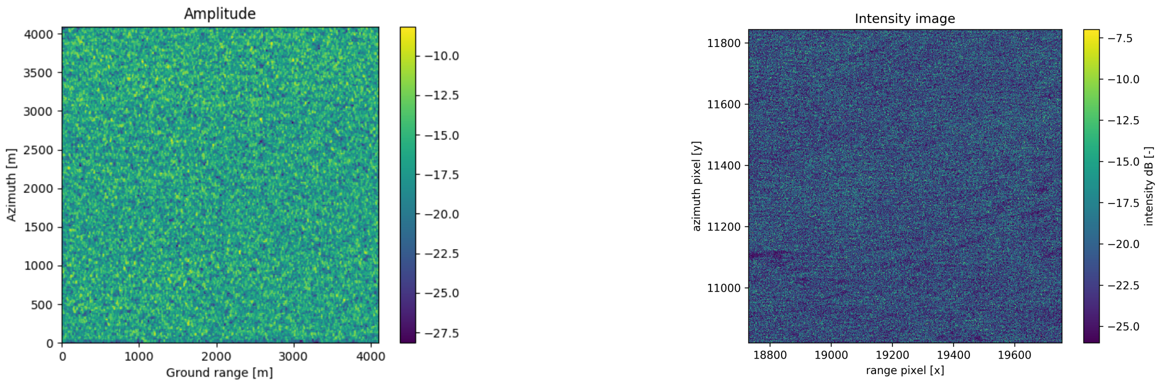

Figure B.4: Intensity (absolute values) images from the OCEANSAR imagette (left) and Sentinel-1 SLC imagette (right). The Sentinel-1 imagette was located at [7, 18] (number of subset in azimuth and range).

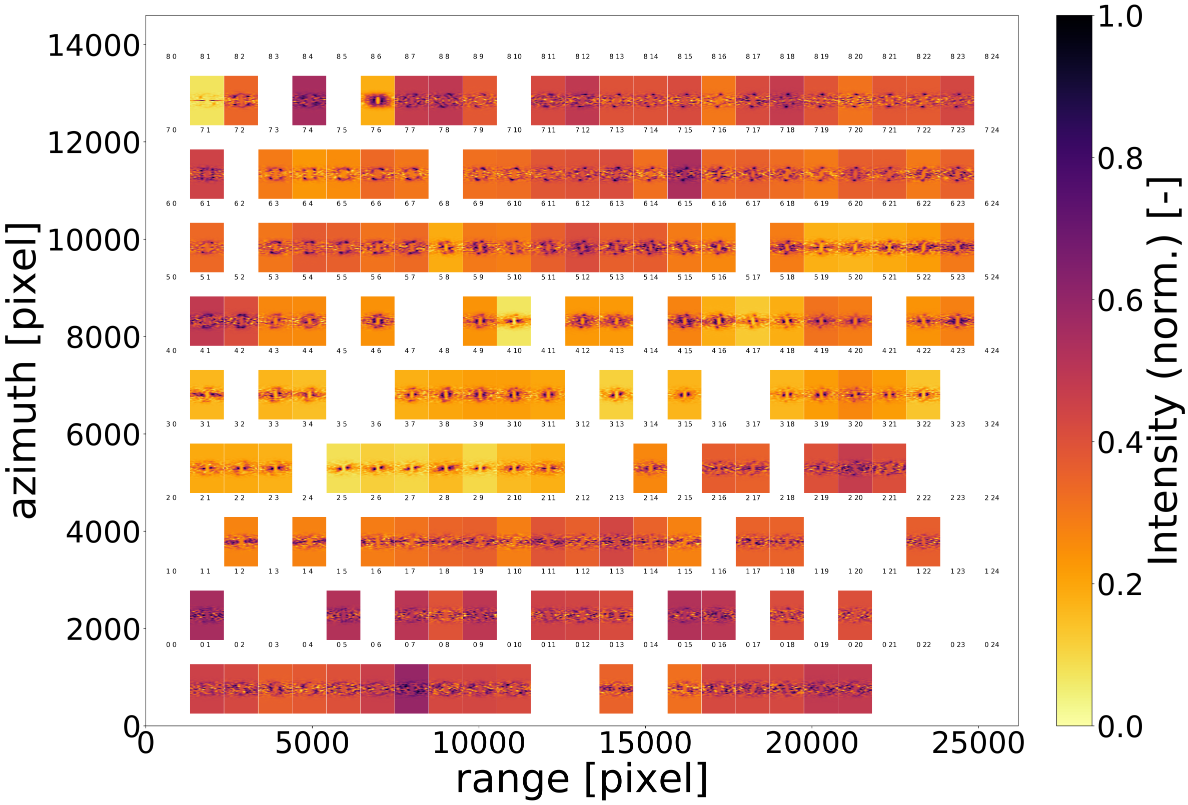

Figure B.5: Real part of the cross spectrum between sub-look 1 and sub-look 3 for different imagettes. size of each imagette is 1024x1024 pixels and the location in azimuth and range is displayed above it. When the computed variance of an imagette was too large, the imagette is white.

Test case 2016-05-19

- Negative result, no swell peak visible on SAR image cross spectra
- Low swell conditions (0.36 m with 11 s period), with a wind speed of 8 m/s. The SAR image showed a low variance.
- Local surfers reported swell waves along the dutch coast on 1th May (http://surfweer.nl/surf/surfweer-maandag-16-m however it was not possible to measure swell waves on SAR images.
- An explanation is distortion of the image by wind. Buoy measurements record a wind speed of 8.24 m/s, with an opposite direction (193 degrees) of the swell waves (350 degrees). As a result the SAR image contains too much noise (speckle) to distinguish swell waves.
- Another explanation is a reduced swell height due to opposing wind (REF). Wind blowing in opposite direction of the swell waves reduced the swell height. After which it was no longer possible to observe.
- Contrary to the S-1 SAR observations, the OCEANSAR cross spectra do show a swell peak. This is explained by the 1D and 2D wave buoy spectra, which show a swell peak, around 0.1 Hz, but no second peak at the higher frequencies (around 0.2 Hz). This means that according to the spectral wave data, no wind waves are present. This would be the case when there is a young sea state, with a local wind gust.

File	S1A_20160519T174119			
date	swath	orbit	lat - lon	heading
2016-05-19	IW3	Ascending	53.02, 2.59	350.88 deg
hm0	swell hm0	period Tp	wind speed	wind direction
0.71 m	0.36 m	11.11 s	8.24 m/s	193.9 deg

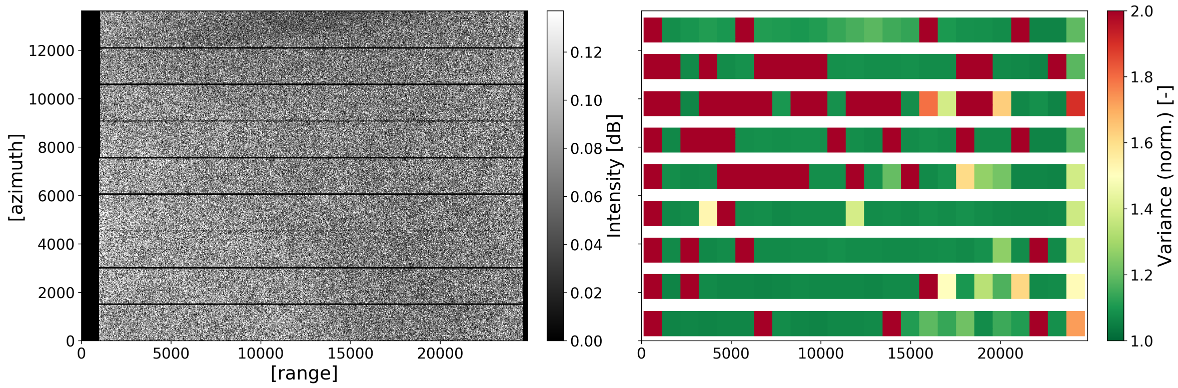

Figure B.6: Sentinel-1 SLC SAR image, acquired on 2016-05-19 17:41:19. Top left image shows the intensity (absolute) values of the 3rd sub-swath. Top right shows computed variance per 1024x1024 imagette of the same sub-swath.

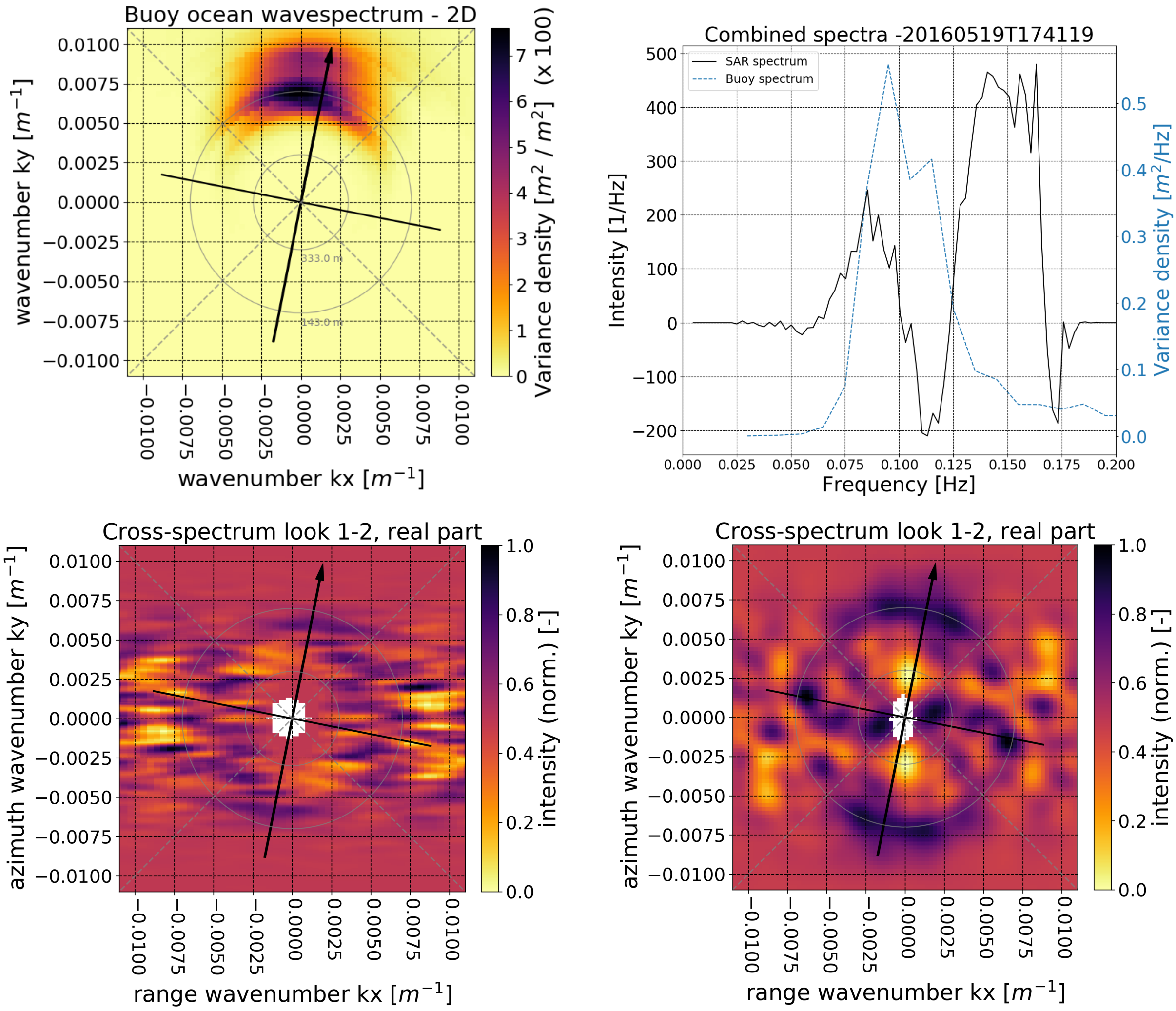

Figure B.7: The top left image shows K13-alpha buoy spectra, top right shows 1D buoy and SAR spectra from 19 May 2016. Bottom images show SAR image spectra (left) and OCEANSAR image spectra (right), between sub-look 1 and sub-look 2.

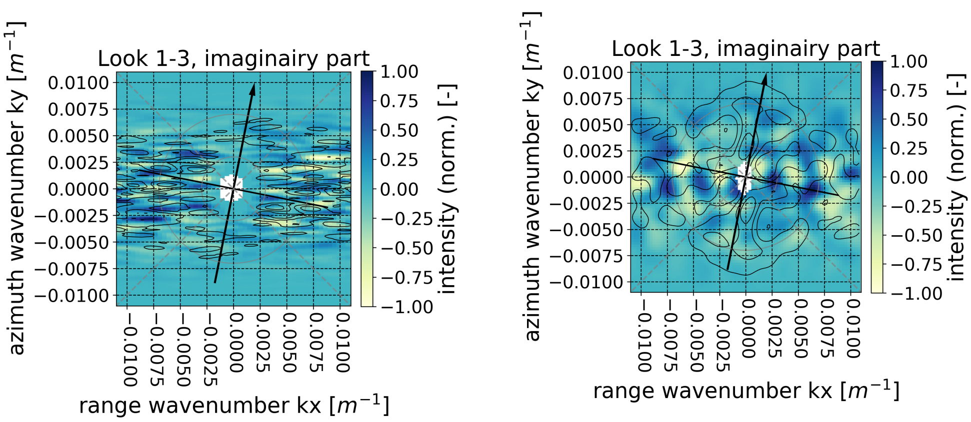

Figure B.8: Imaginary part of the cross spectrum between sub-look 1 and sub-look 3, contour lines show the real part of the cross spectrum. SAR image spectrum is plotted on the left and OCEANSAR spectrum on the right.

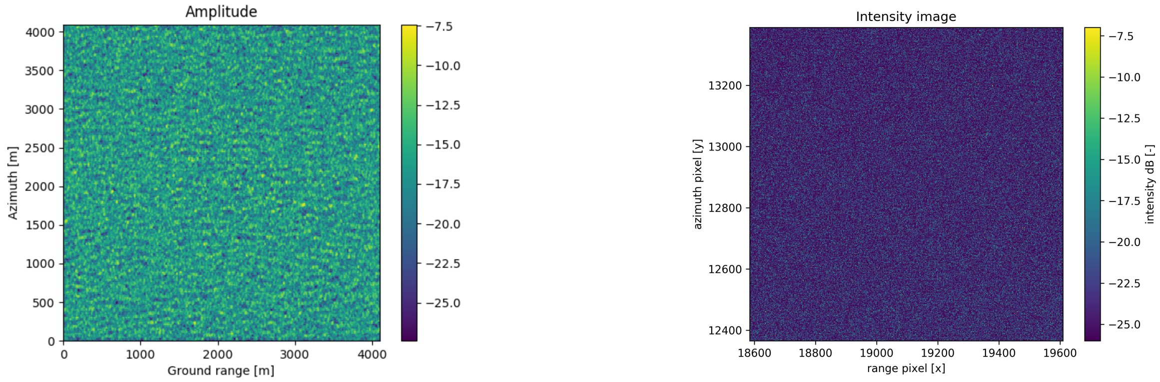

Figure B.9: Intensity (absolute values) images from the OCEANSAR imagette (left) and Sentinel-1 SLC imagette (right). The Sentinel-1 imagette was located at [8,18] (number of subset in azimuth and range).

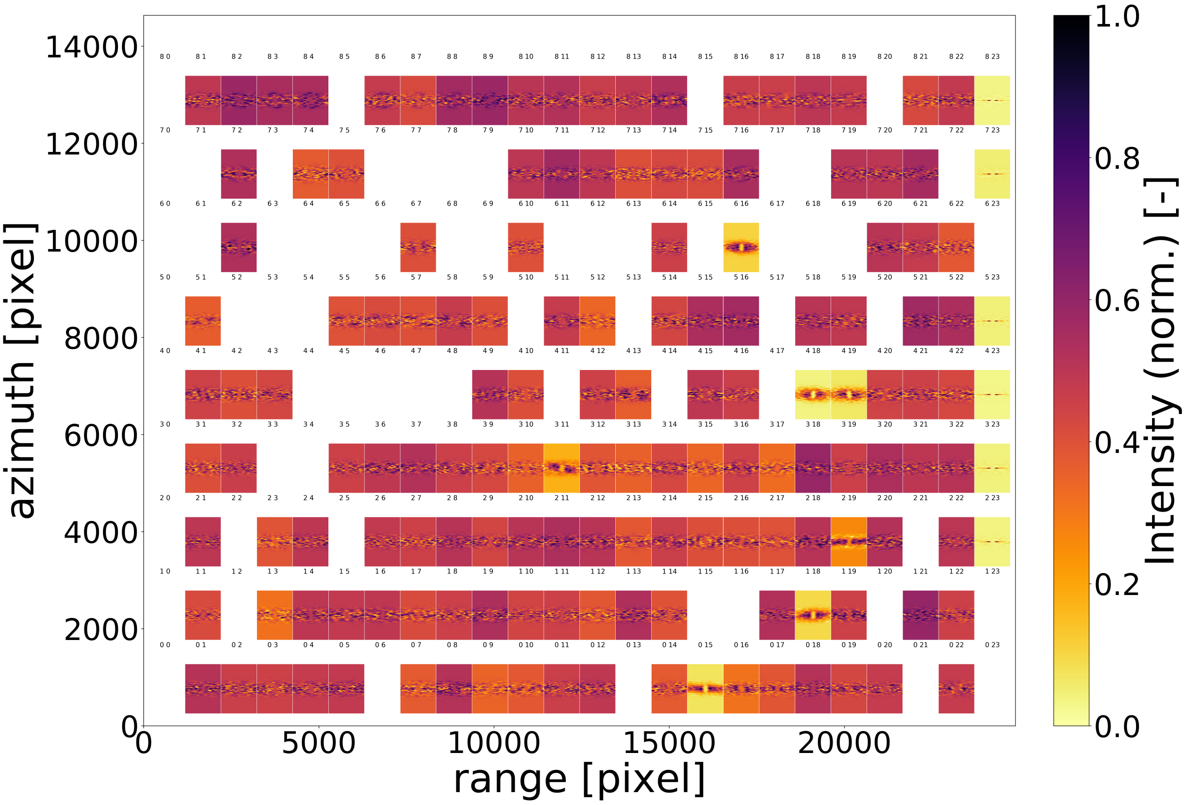

Figure B.10: Real part of the cross spectrum between sub-look 1 and sub-look 3 for different imagettes. size of each imagette is 1024x1024 pixels and the location in azimuth and range is displayed above it. When the computed variance of an imagette was too large, the imagette is white.

Test case 2016-10-01

- Negative result, no observable swell peak. Buoy observations show low swell hm0 of 0.22 m, compared to a significant wave height of 1.12 m. Swell signal is probably too small to be measured by SAR
- Spectral data plotted in figure A.7 is from different time stamp then satellite observation. There was no spectra buoy data available at the K13 alpha buoy at 06:05, the closest available data was at a time of 07:10, which was used in this case.
- 1D spectra show similarities, however when we look at the 2D spectra this is mostly due to noise (speckle)
- Descending pass, which means the direction between incoming swell is different compared to an ascending pass.
- Surf observations mention between 07:00 and 09:00 a swell height high enough to go surfing, this could also been seen on web cam pictures.. This suggests that swell waves were present on this day. http://surfweer.nl/surf/surfweer-zaterdag-1-oktober-2016/

File	S1B_20161001T060515			
date	swath	orbit	lat - lon	heading
2016-10-01	IW1	Descending	53.273, 3.440	11.167 deg
hm0	swell hm0	period Tp	wind speed	wind direction
1.12 m	0.22 m	5.00 s	2.75 m/s	159.6 deg

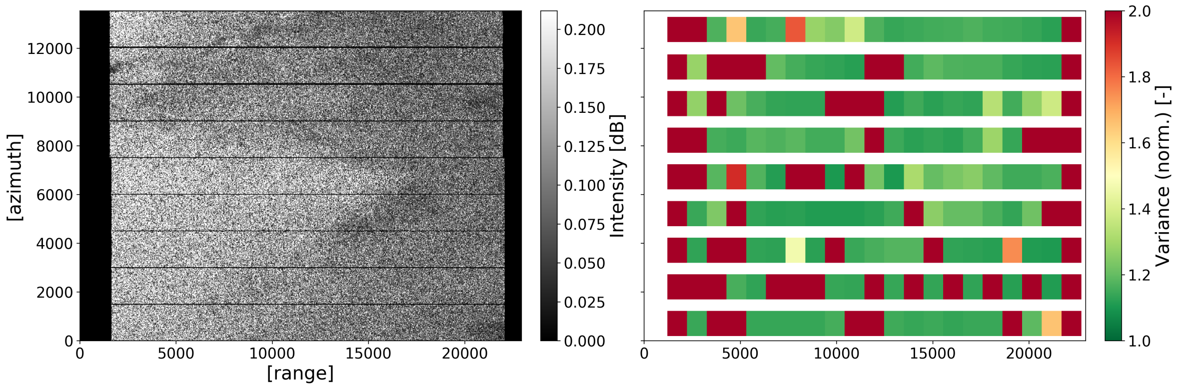

Figure B.11: Sentinel-1 SLC SAR image, acquired on 2016-10-01 06:05:15. Top left image shows the intensity (absolute) values of the 1st sub-swath. Top right shows computed variance per 1024x1024 imagette of the same sub-swath.

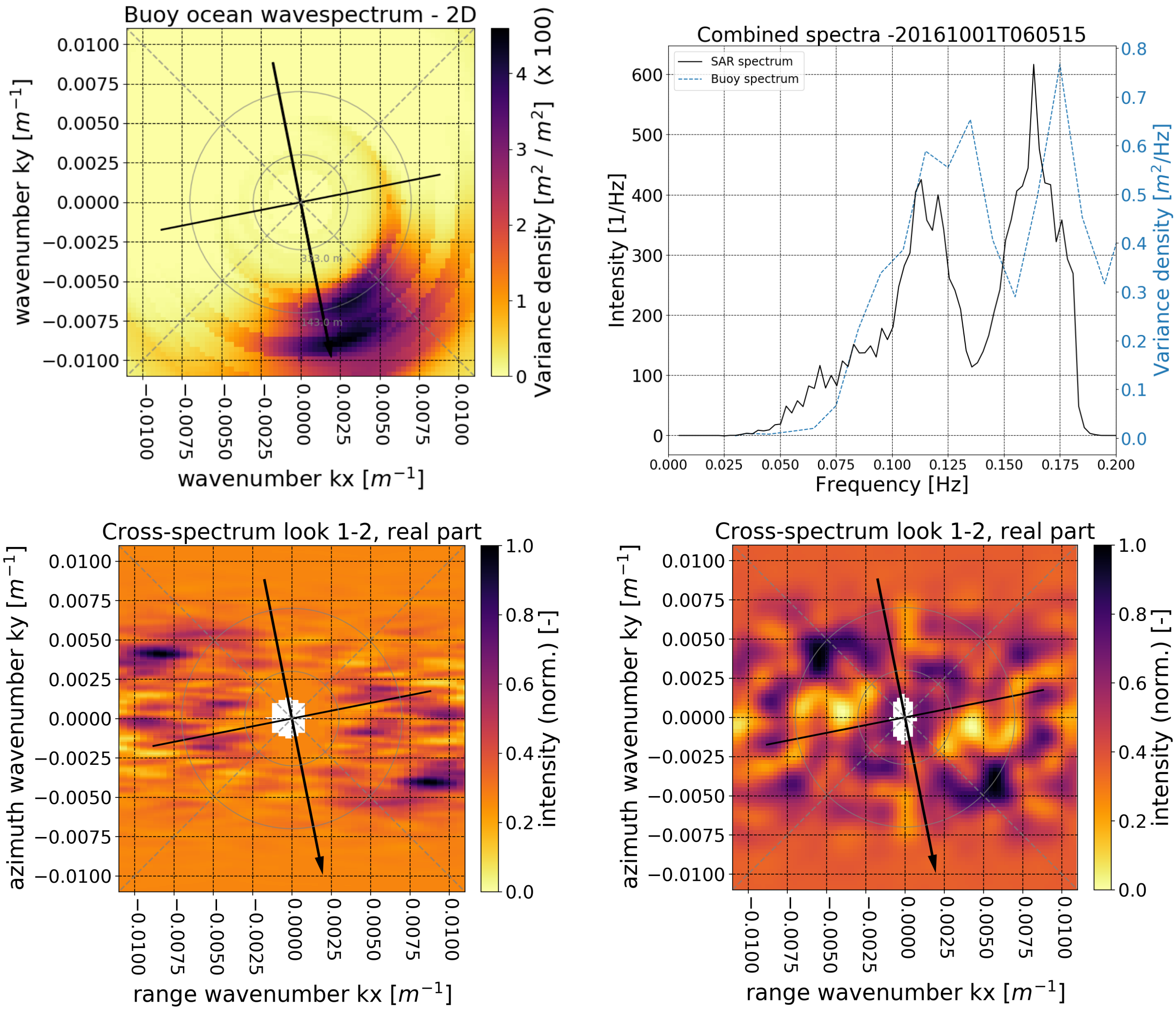

Figure B.12: The top left image shows K13-alpha buoy spectra, top right shows 1D buoy and SAR spectra from 01 October 2016. Bottom images show SAR image spectra (left) and OCEANSAR image spectra (right), between sub-look 1 and sub-look 2.

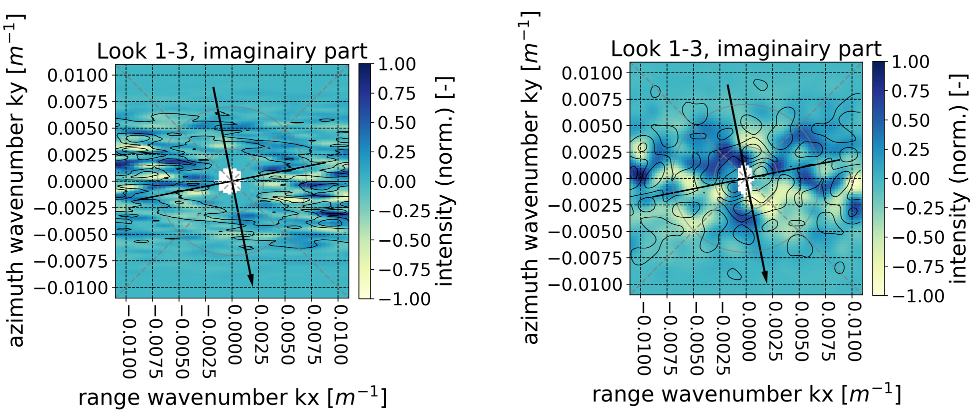

Figure B.13: Imaginary part of the cross spectrum between sub-look 1 and sub-look 3, contour lines show the real part of the cross spectrum. SAR image spectrum is plotted on the left and OCEANSAR spectrum on the right.

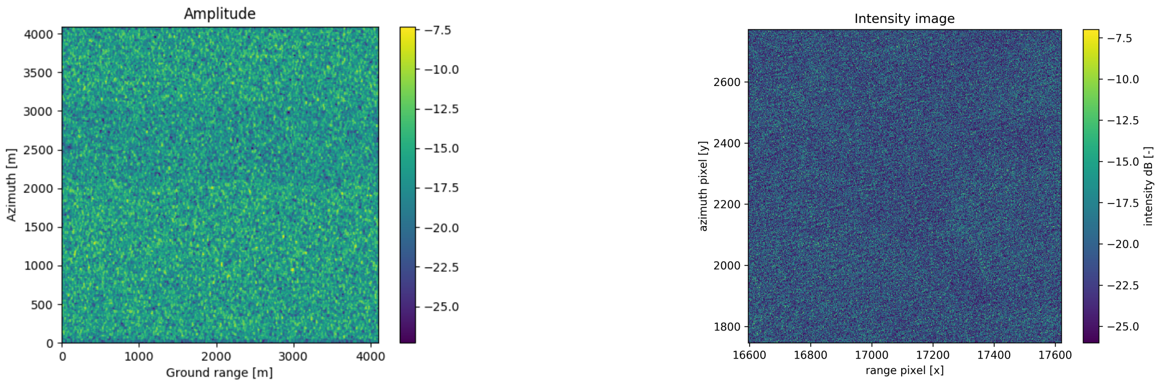

Figure B.14: Intensity (absolute values) images from the OCEANSAR imagette (left) and Sentinel-1 SLC imagette (right). The Sentinel-1 imagette was located at [1, 16] (number of subset in azimuth and range).

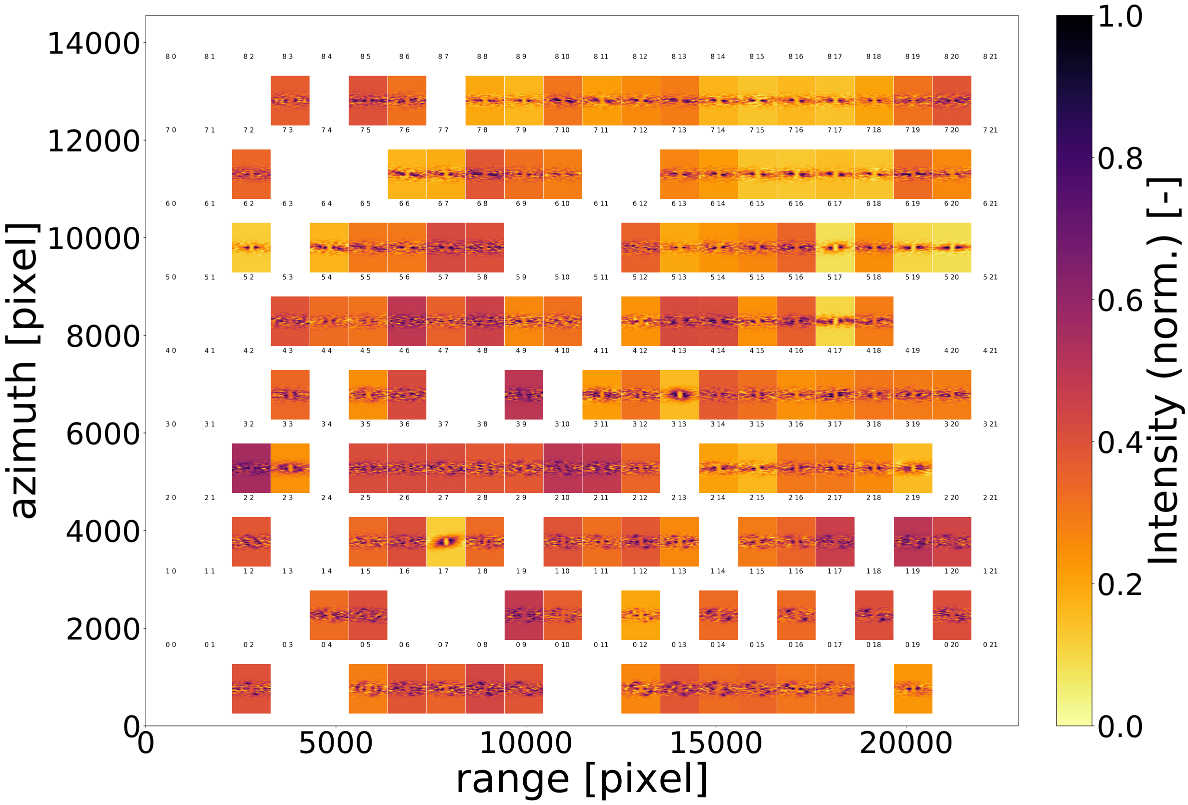

Figure B.15: Real part of the cross spectrum between sub-look 1 and sub-look 3 for different imagettes. size of each imagette is 1024x1024 pixels and the location in azimuth and range is displayed above it. When the computed variance of an imagette was too large, the imagette is white.

Test case 2016-10-30

- Positive result, swell is observed on SAR image at kx = 0.0 m and ky = 0.005 m, with a wave number matching spectral buoy observations.OCEANSAR simulations also show a peak at a wave number of 0.005 m.
- The clear observation of swell is probably due to the absence of wind (wind speed of 0.82 m/s) and a high swell wave height (of 0.62 m).
- Direction from buoy measurements (360 degrees) is slightly different compared to SAR cross spectra (350 degrees) and OCEANSAR spectra (340 degrees).
- OCEANSAR cross spectra show directional spreading of the swell peak from 330 to 360 degrees, with a size of approximately 30 degrees. This is larger compared to the spreading of the SAR spectra (10 degrees) or the wave buoy spectra (15 degrees). Additionally, SAR cross spectra do not show directional spreading. The swell peak is elongated in range direction. This is probably an effect of smoothing of the signal.
- 1D spectra show a matching peak around 0.08 Hz.
- Local surfers mention clear swell lines with a 10 second period observable along the dutch coast http://surfweer.nl/surf/surf-laatste-weekend-29-oktober-2016/.

File	S1B_20161030T172429			
date	swath	orbit	lat - lon	heading
2016-10-30	IW1	Ascending	53.484, 3.979	348.796 deg
hm0	swell hm0	period Tp	wind speed	wind direction
1.04 m	0.62 m	11.11 s	0.82 m/s	320.4 deg

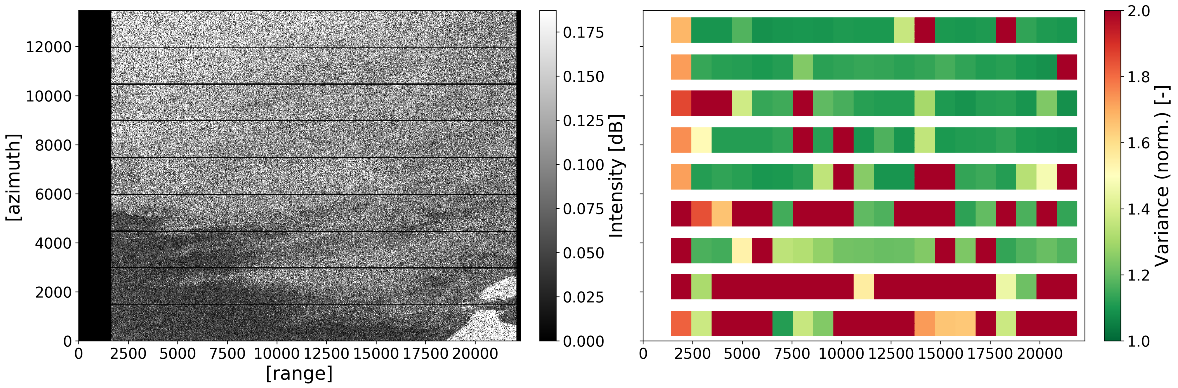

Figure B.16: Sentinel-1 SLC SAR image, acquired on 2016-10-30 17:24:29. Left image shows the intensity (absolute) values of the 1st sub-swath. Top right shows computed variance per 1024x1024 imagette of the same sub-swath.

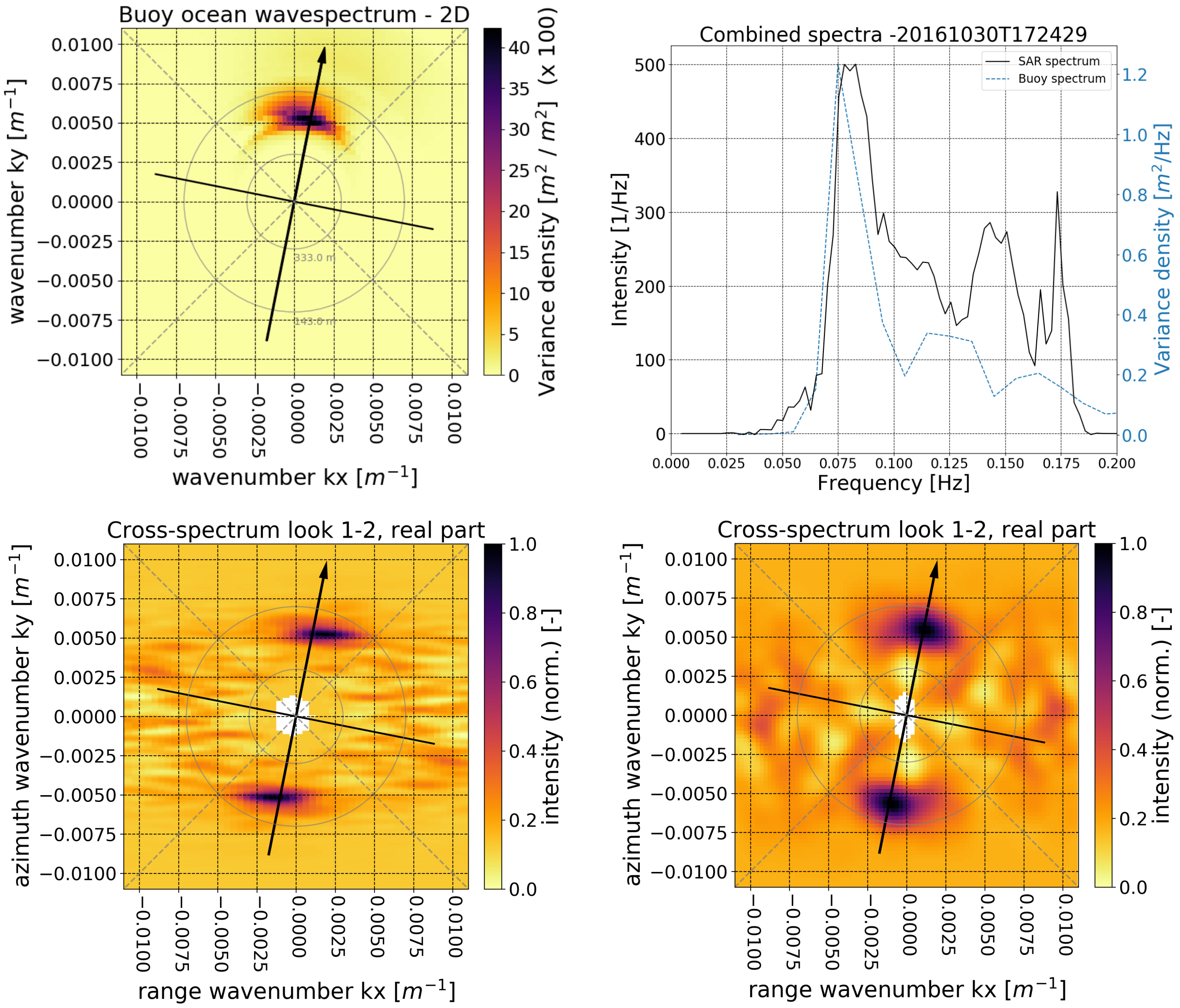

Figure B.17: The top left image shows K13-alpha buoy spectra, top right shows 1D buoy and SAR spectra from 30 October 2016. Bottom images show SAR image spectra (left) and OCEANSAR image spectra (right), between sub-look 1 and sub-look 2.

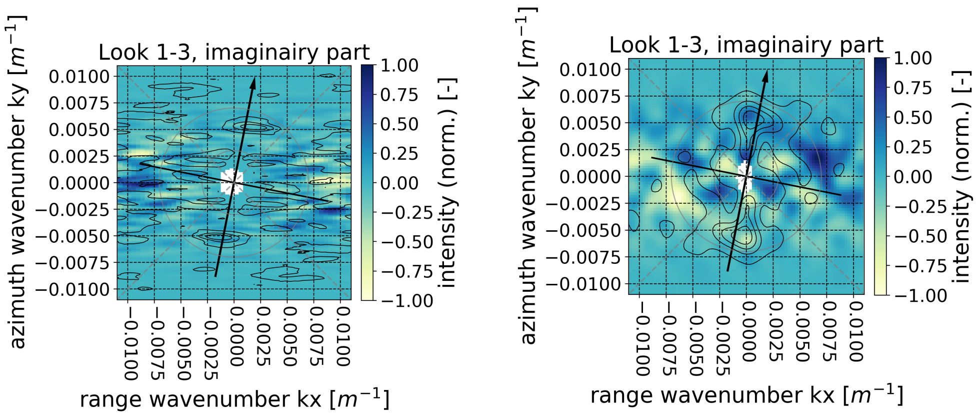

Figure B.18: Imaginary part of the cross spectrum between sub-look 1 and sub-look 3, contour lines show the real part of the cross spectrum. SAR image spectrum is plotted on the left and OCEANSAR spectrum on the right.

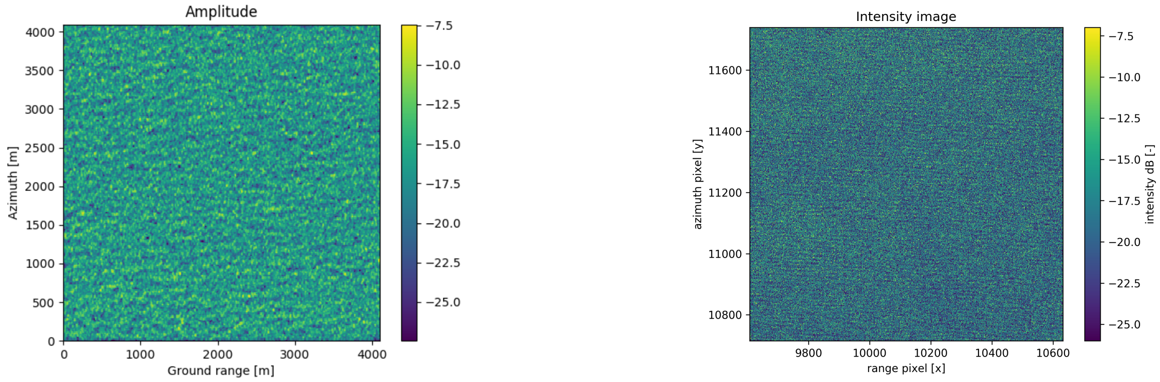

Figure B.19: Intensity (absolute values) images from the OCEANSAR imagette (left) and Sentinel-1 SLC imagette (right). The Sentinel-1 imagette was located at [7,9] (number of subset in azimuth and range).

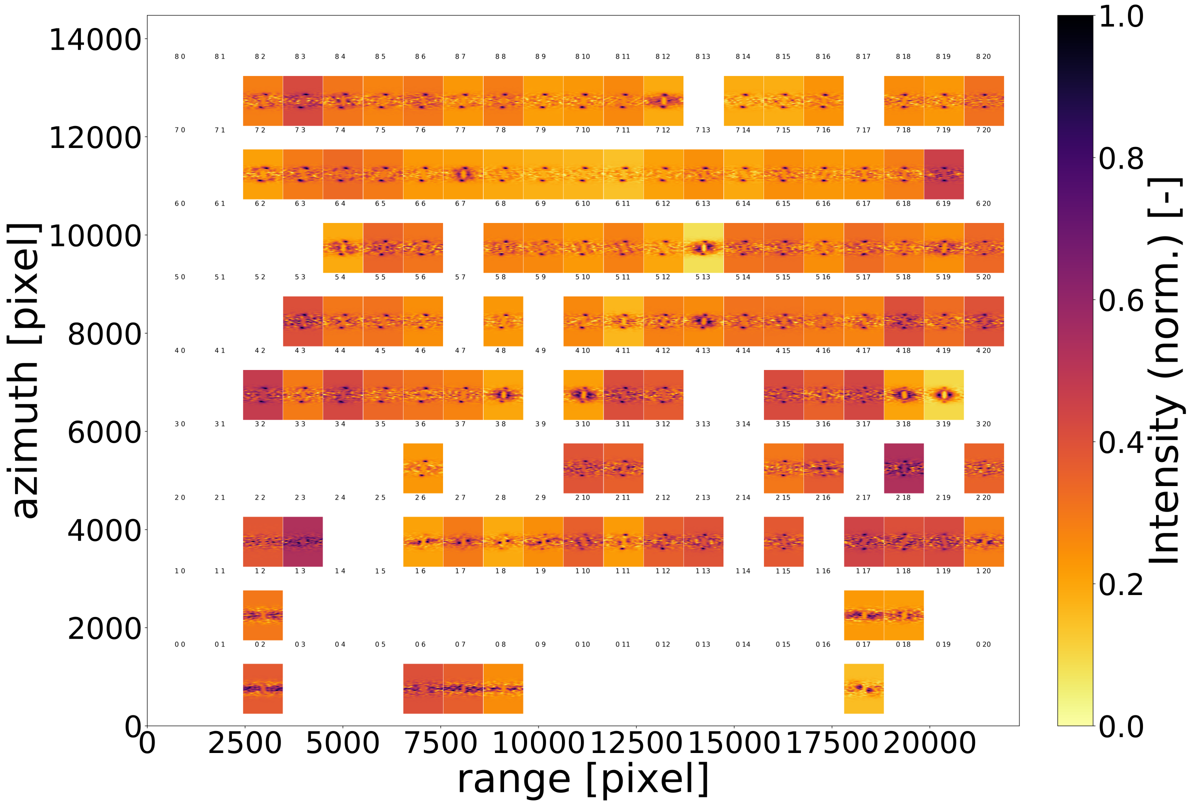

Figure B.20: Real part of the cross spectrum between sub-look 1 and sub-look 3 for different imagettes. size of each imagette is 1024x1024 pixels and the location in azimuth and range is displayed above it. When the computed variance of an imagette was too large, the imagette is white.

Test case 2016-10-31

- Mixed results. Most cross spectra from subsets showed a negative result. Only a few cross spectra showed a swell peak. Figure B.22 shows the cross spectrum at subset azimuth = 2 and range = 8.
- Despite medium swell on this day with low wind speed mostly negative results
- Hypothesis is a different direction, a descending pass, which made spectral retrieval more difficult.
- Area's where variance was too high, spectral retrieval possible near those area's.
- Intensity image showed several features present on the radar image. e.g. streaks which result from shipping motions, other streaks are also visible which might result either wind streaks or currents
- The appearance of streaks on the image would indicate that on this date, a very low significant wave height occurs. This is also observed the buoy data,
- cross spectra retrieval possible in area with higher variance, theory: wind gust creates Bragg-waves, scattering of Bragg waves enhanced by swell.
- No mention of swell waves by local surfers

  http://surfweer.nl/surf/surf-laatste-weekend-29-oktober-2016/.

File	S1A_20161031T060557			
date 2016-10-31	swath IW1	orbit Descending	lat - lon 53.27, 3.43	heading 11.16 deg
hm0 0.72 m	swell hm0 0.31 m	period Tp 11.11 s	wind speed 2.46 m/s	wind direction 197.5 deg

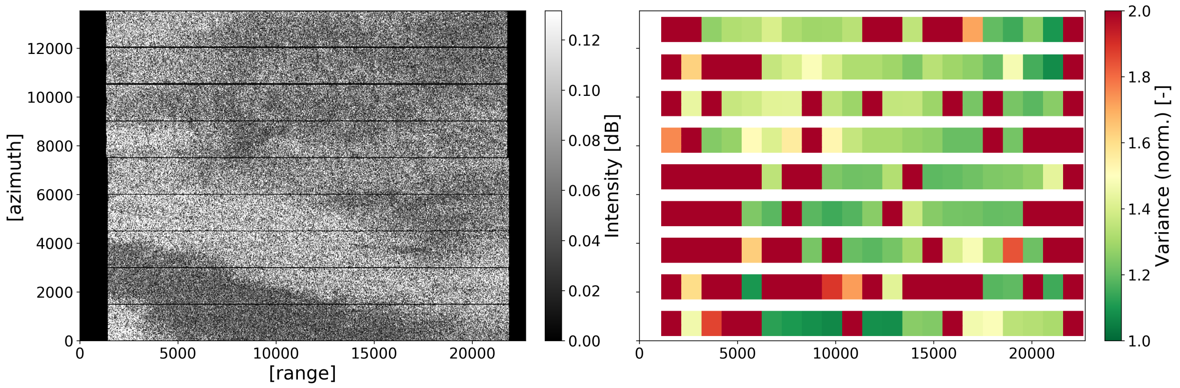

Figure B.21: Sentinel-1 SLC SAR image, acquired on 2016-10-31 06:05:57. Left image shows the intensity (absolute) values of the 1st sub-swath. Right image shows computed variance per 1024x1024 imagette of the same sub-swath.

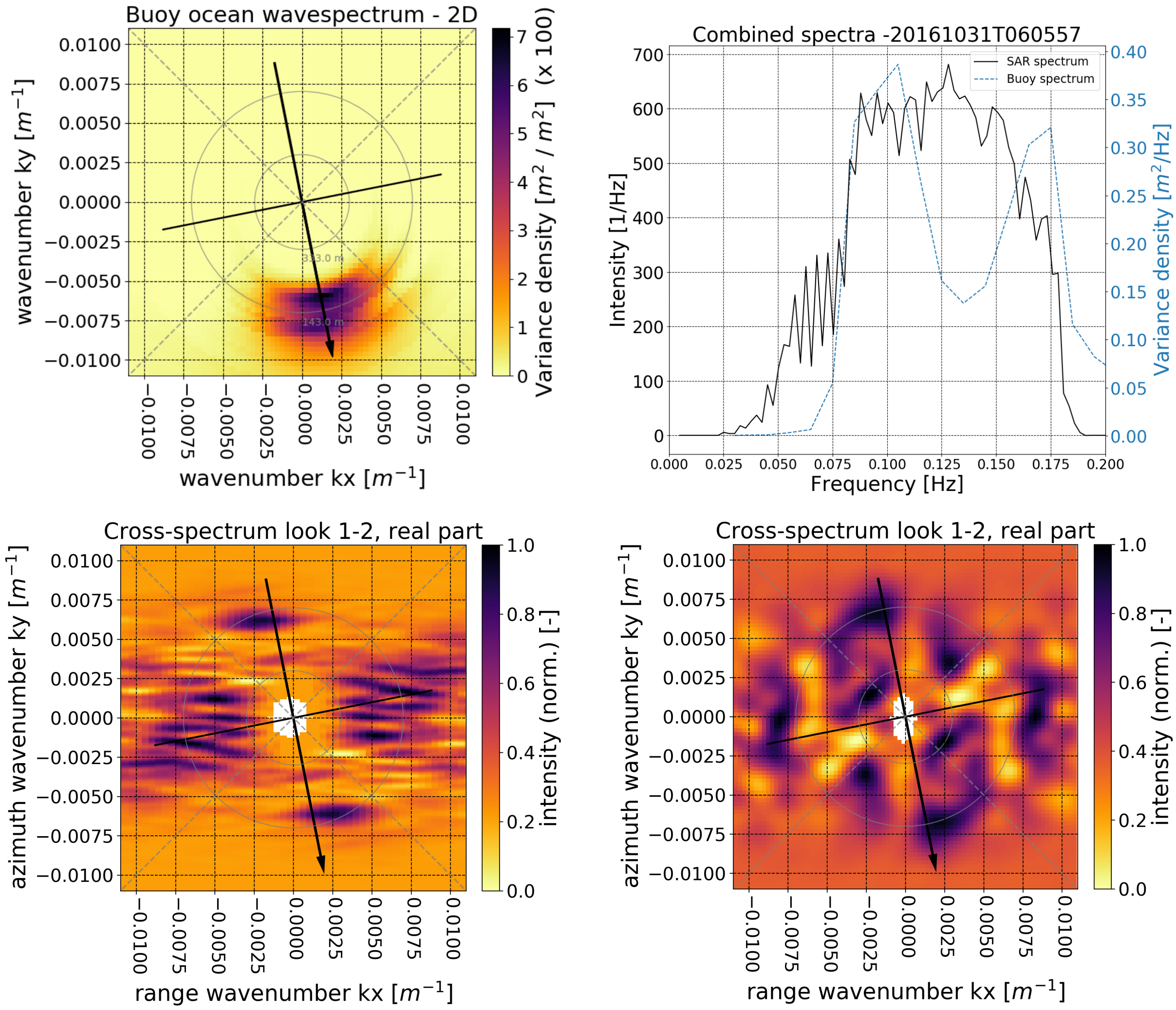

Figure B.22: The top left image shows K13-alpha buoy spectra, top right shows 1D buoy and SAR spectra from 31 October 2016. Bottom images show SAR image spectra (left) and OCEANSAR image spectra (right), between sub-look 1 and sub-look 2.

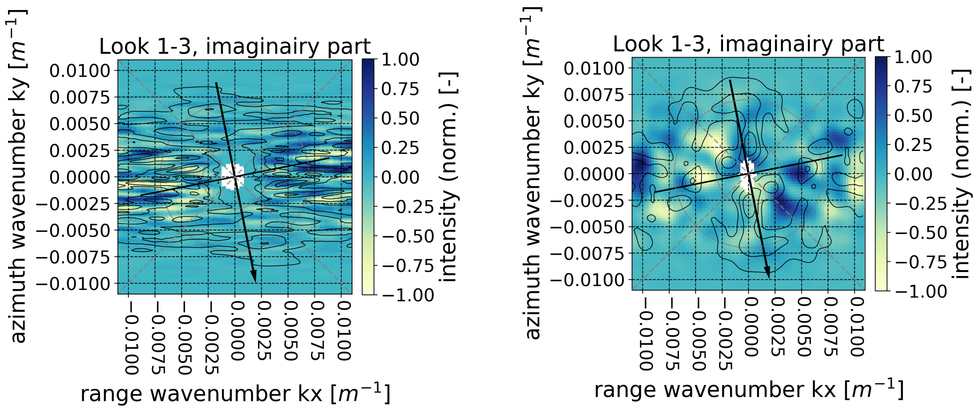

Figure B.23: Imaginary part of the cross spectrum between sub-look 1 and sub-look 3, contour lines show the real part of the cross spectrum. SAR image spectrum is plotted on the left and OCEANSAR spectrum on the right.

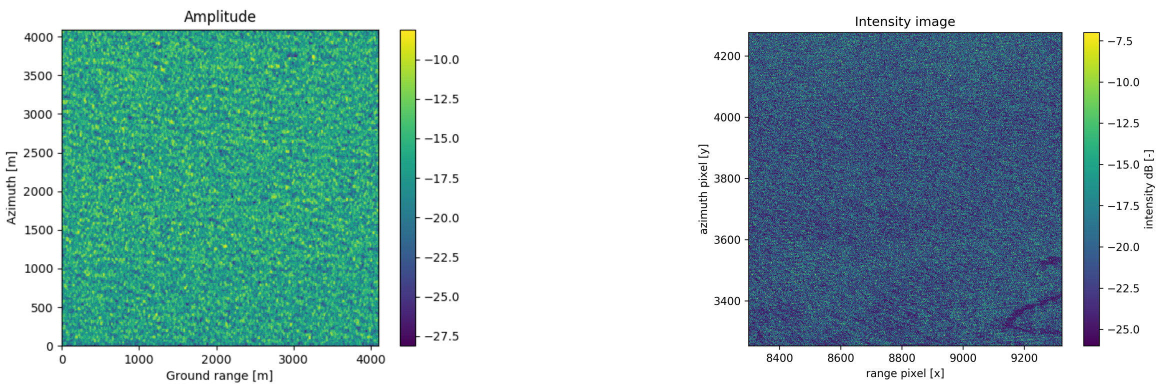

Figure B.24: Intensity (absolute values) images from the OCEANSAR imagette (left) and Sentinel-1 SLC imagette (right). The Sentinel-1 imagette was located at [2,8] (number of subset in azimuth and range).

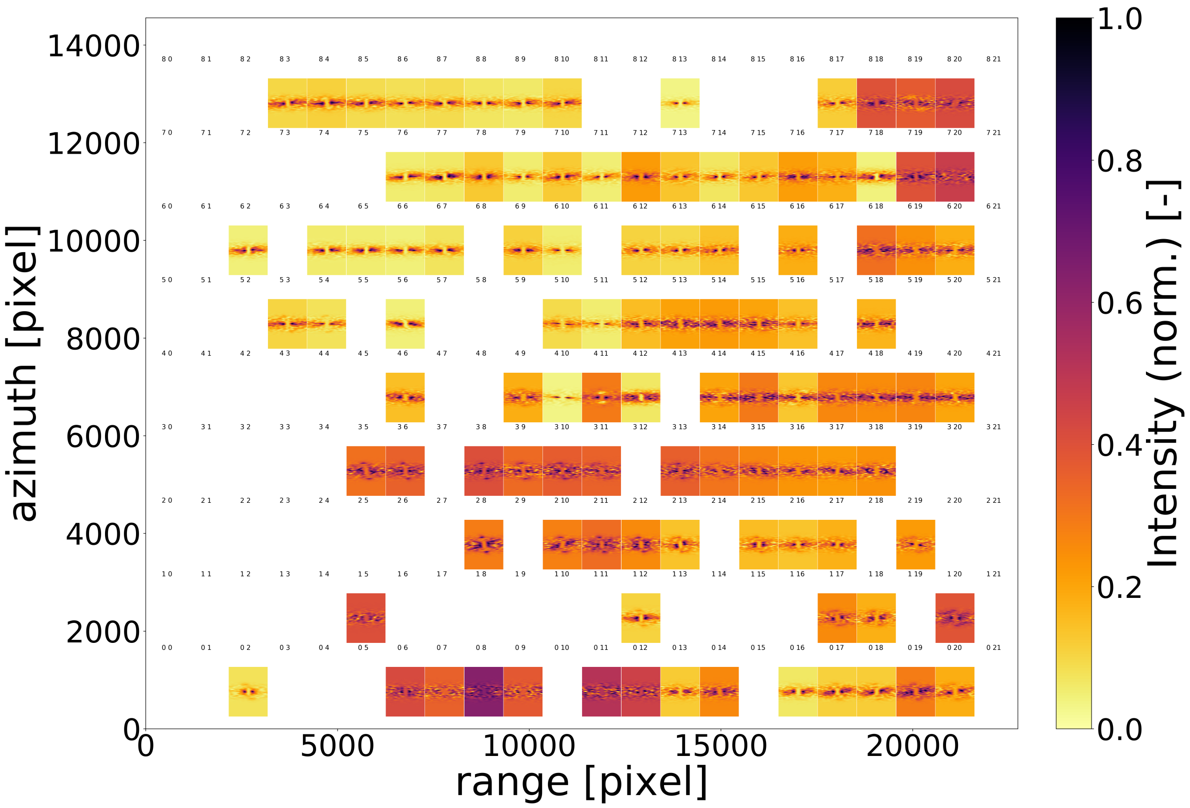

Figure B.25: Real part of the cross spectrum between sub-look 1 and sub-look 3 for different imagettes. size of each imagette is 1024x1024 pixels and the location in azimuth and range is displayed above it. When the computed variance of an imagette was too large, the imagette is white.

Test case 2016-11-29

- Negative result, no quasi-linear swell spectrum observed on imagettes. Buoy measurements show a low swell wave height (0.24 m) and a wind speed of 7.14 m/s. Most likely, quasi-linear signal is too weak to pick up by SAR sensor.
- 2D buoy spectra show a dual peak spectrum. One peak around $k = 0.0061/m$ and a lower second peak around $k = 0.0091/m$. The direction and wave length corresponding to the first peak should mean it is observable by SAR.
- 1D buoy spectra show is different compared to the SAR spectra due to a contribution of noise (speckle) and non-linear part of the signal due to wind.
- Local surfer observations (http://surfweer.nl/surf/surfweer-zondag-27-november-2016/) show low swell wave height with almost no wind. Swell waves were surf-able tough. Also, swell waves, especially the longer period waves dissipate due to bottom interaction, which decreases their height.

File	S1A_20161129T172515			
date 2016-11-29	swath IW1	orbit Ascending	lat - lon 53.648, 3.932	heading 348.79 deg
hm0 0.75 m	swell hm0 0.24 m	period Tp 10.00 s	wind speed 7.14 m/s	wind direction 261.6 deg

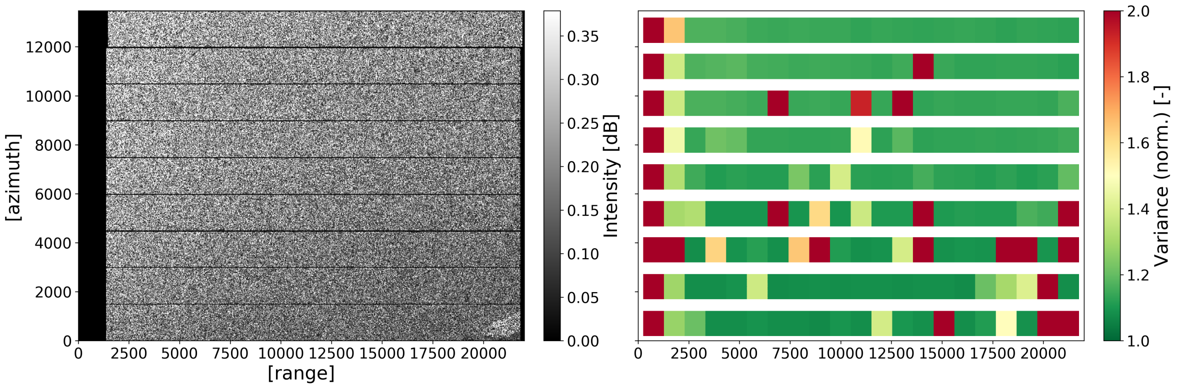

Figure B.26: Sentinel-1 SLC SAR image, acquired on 2016-11-29 17:25:15. Top left image shows the intensity (absolute) values of the 1st sub-swath. Top right shows computed variance per 1024x1024 imagette of the same sub-swath.

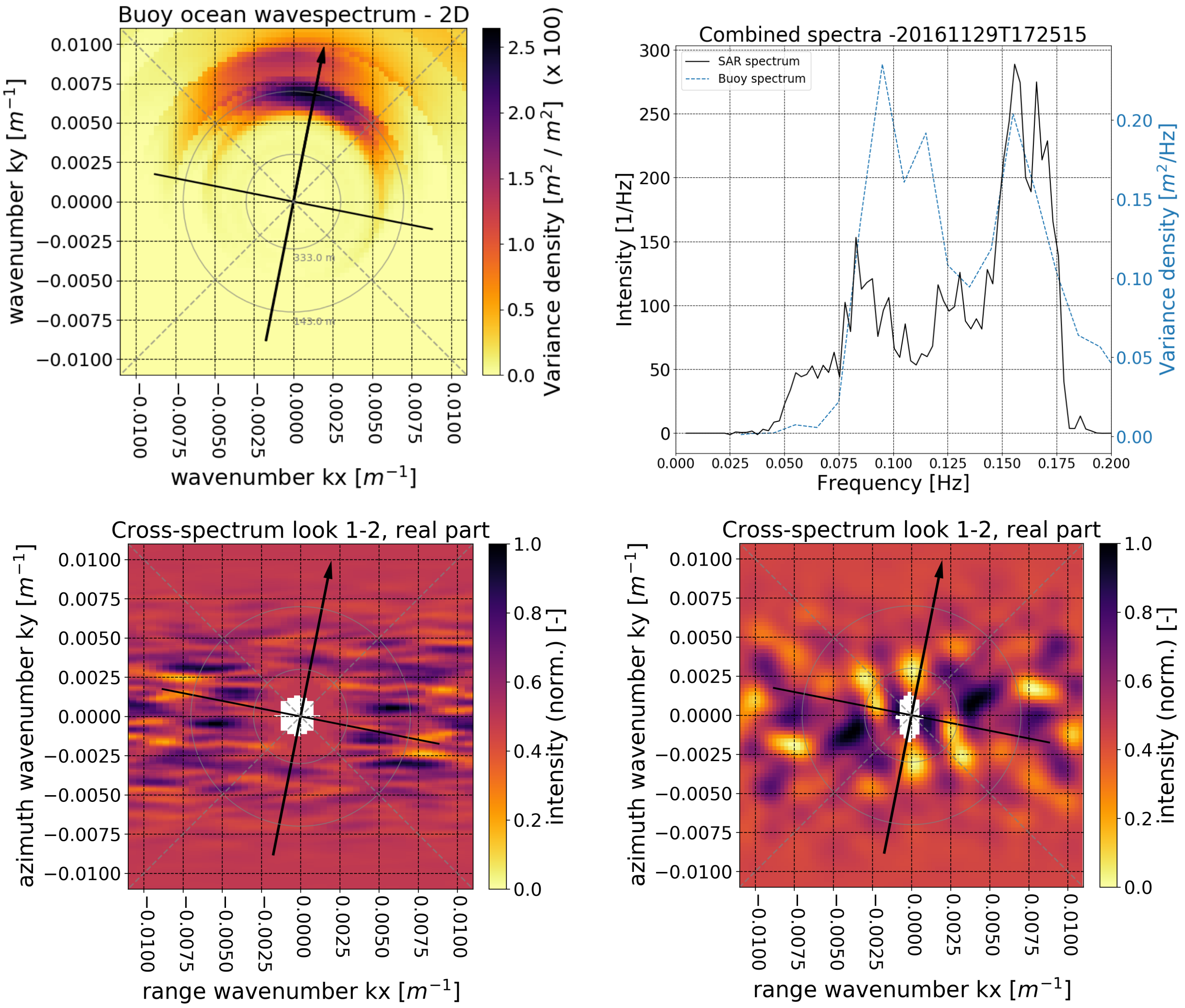

Figure B.27: The top left image shows K13-alpha buoy spectra, top right shows 1D buoy and SAR spectra from 29 November 2016. Bottom images show SAR image spectra (left) and OCEANSAR image spectra (right), between sub-look 1 and sub-look 2.

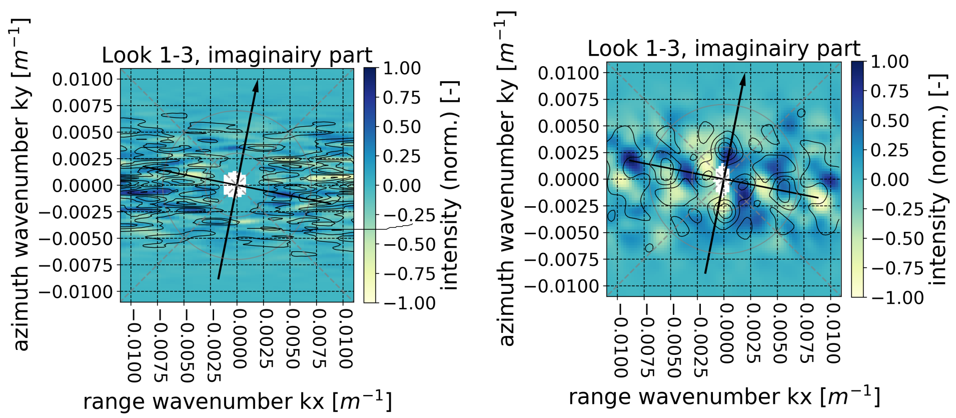

Figure B.28: Imaginary part of the cross spectrum between sub-look 1 and sub-look 3, contour lines show the real part of the cross spectrum. SAR image spectrum is plotted on the left and OCEANSAR spectrum on the right.

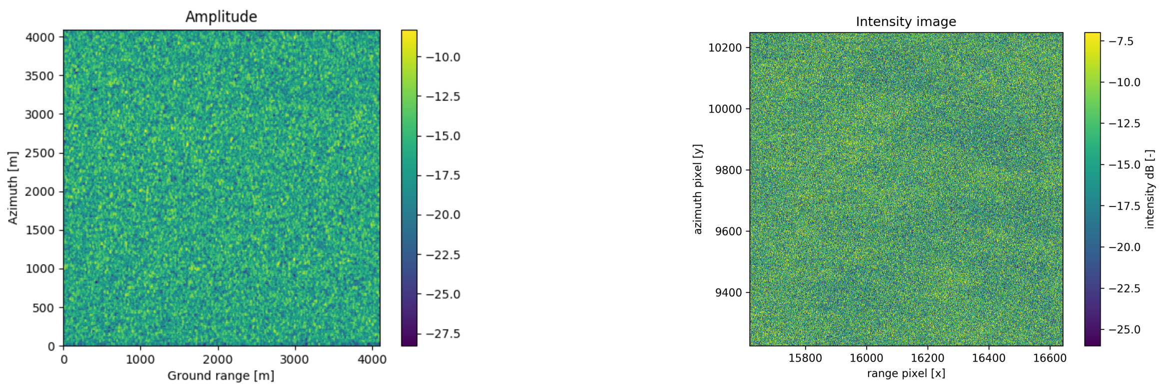

Figure B.29: Intensity (absolute values) images from the OCEANSAR imagette (left) and Sentinel-1 SLC imagette (right). The Sentinel-1 imagette was located at [6,15] (number of subset in azimuth and range).

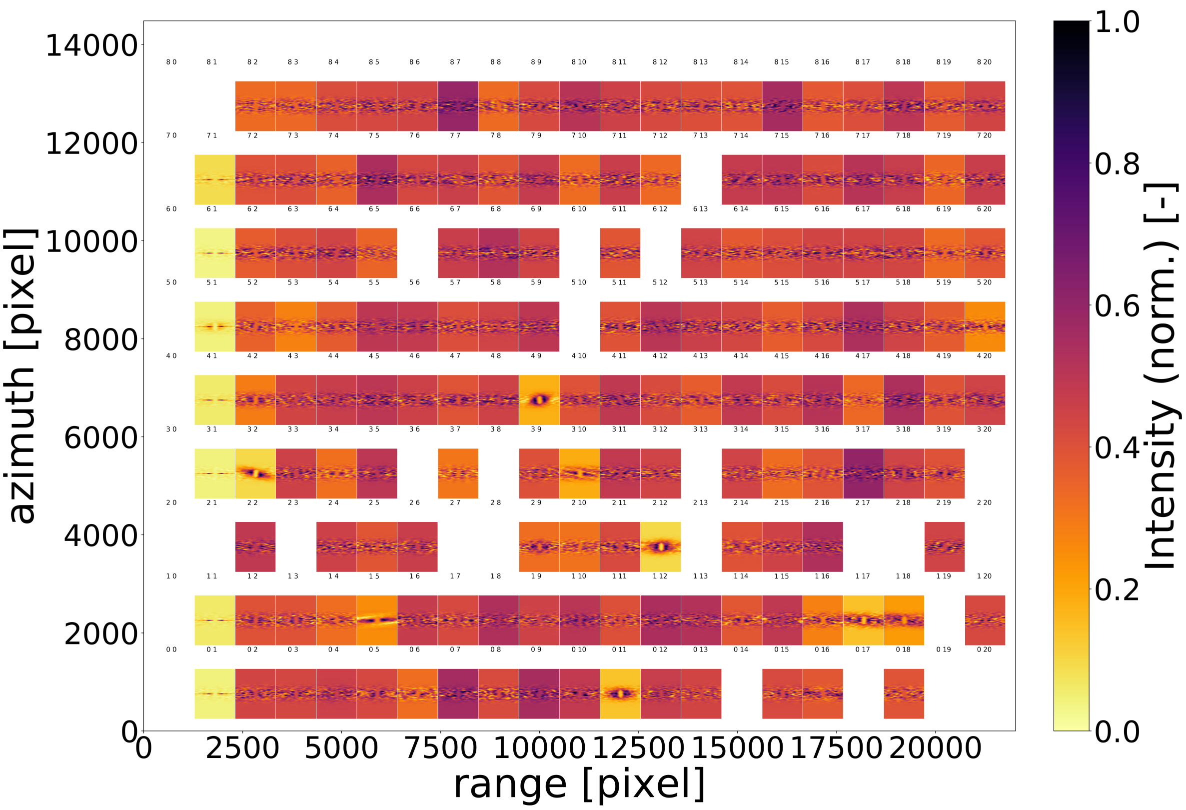

Figure B.30: Real part of the cross spectrum between sub-look 1 and sub-look 3 for different imagettes. size of each imagette is 1024x1024 pixels and the location in azimuth and range is displayed above it. When the computed variance of an imagette was too large, the imagette is white.

Test case 2016-12-10

– Mixed results, a few of the 216 imagettes cross spectra show a quasi-linear swell spectrum. It is arguable though if this truly is a quasi-linear contribution or simply noise. Most of the other cross spectra only show non-linear contributions due to wind and speckle (noise).

– Surfer observations mention a flat ocean surface with occasionally a single swell wave http://surfweer.nl/surf/surfweer-woensdag-7-december-2016/.

– 1D wave buoy spectra show two peaks, one peak around 0.06 Hz and a second peak around 0.167 Hz. According to buoy measurements, swell hm0 is only 0.24 m, with a wind speed of 6.71 m/s. Swell is probably too small to be measured by the SAR or non-linear contributions are stronger.

File	S1B_20161210T173232			
date 2016-12-10	swath IW2	orbit Ascending	lat - lon 53.066, 3.384	heading 349.889 deg
hm0 0.82 m	swell hm0 0.27 m	period Tp 5.56 s	wind speed 6.71 m/s	wind direction 240.8 deg

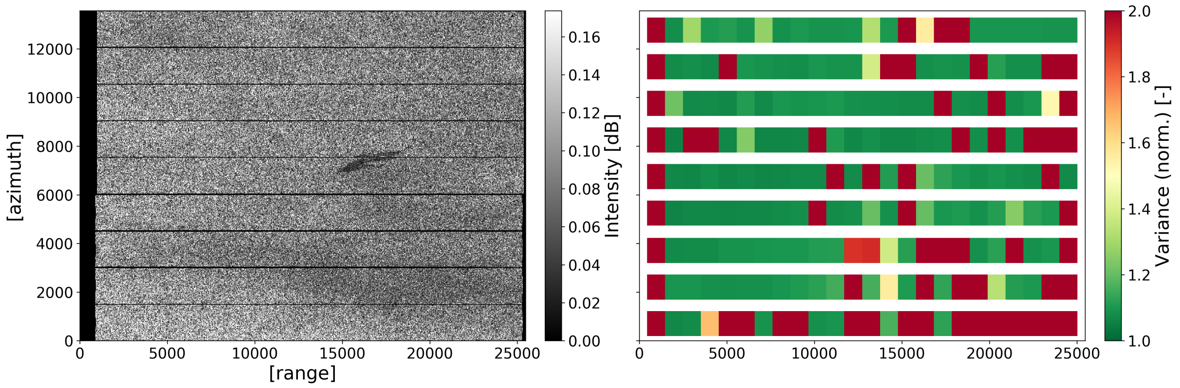

Figure B.31: Sentinel-1 SLC SAR image, acquired on 2016-12-10 17:32:32. Left image shows the intensity (absolute) values of the 2nd sub-swath. Right image shows computed variance per 1024x1024 imagette of the same sub-swath.

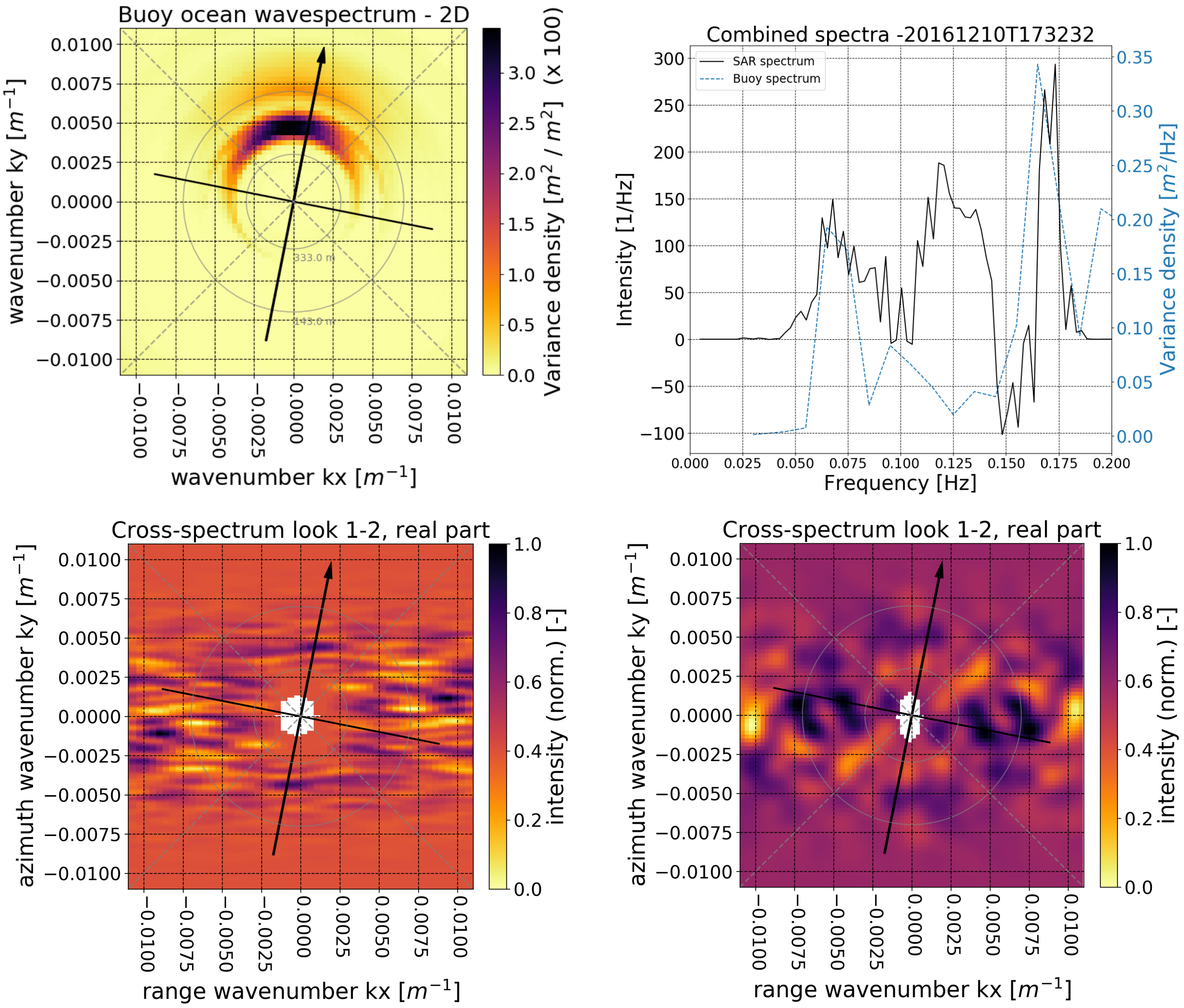

Figure B.32: The top left image shows IJ-geul buoy spectra, top right shows 1D buoy and SAR spectra from 12 December 2016. Bottom images show SAR image spectra (left) and OCEANSAR image spectra (right), between sub-look 1 and sub-look 2.

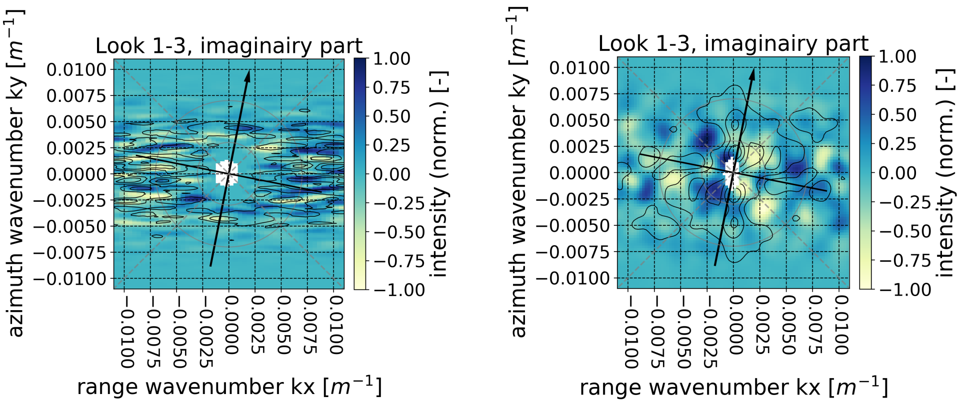

Figure B.33: Imaginary part of the cross spectrum between sub-look 1 and sub-look 3, contour lines show the real part of the cross spectrum. SAR image spectrum is plotted on the left and OCEANSAR spectrum on the right.

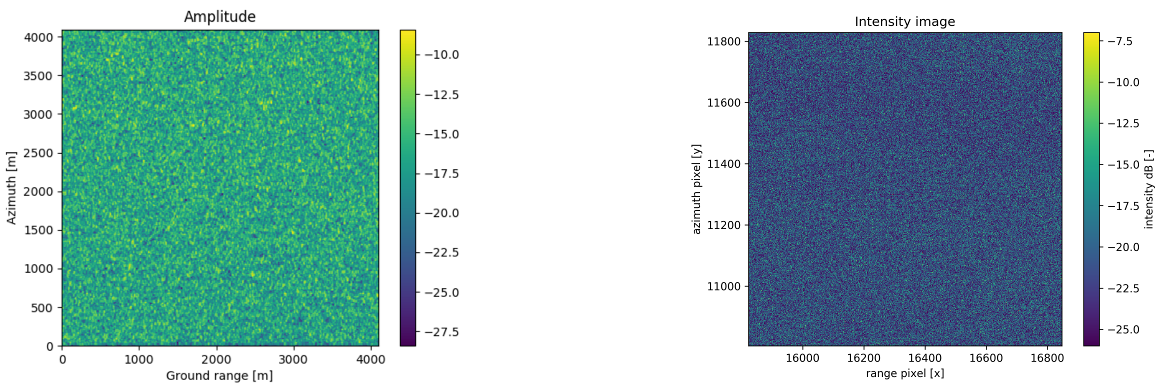

Figure B.34: Intensity (absolute values) images from the OCEANSAR imagette (left) and Sentinel-1 SLC imagette (right). The Sentinel-1 imagette was located at [7, 15] (number of subset in azimuth and range).

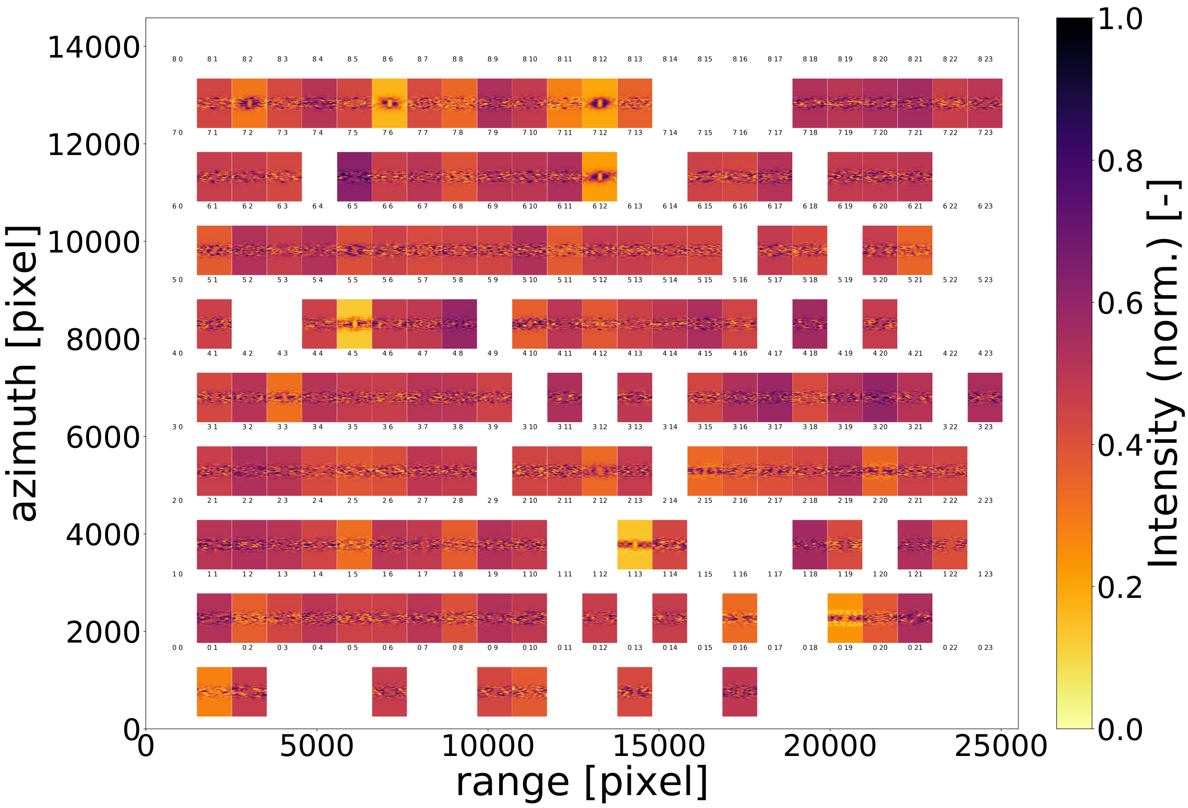

Figure B.35: Real part of the cross spectrum between sub-look 1 and sub-look 3 for different imagettes. size of each imagette is 1024x1024 pixels and the location in azimuth and range is displayed above it. When the computed variance of an imagette was too large, the imagette is white.

Test case 2017-01-08

- Positive result, peak observable on SAR imagette cross spectra, the quasi-linear swell peak matches peak of buoy observations.
- SAR peak is smeared in range direction, sort of lensing effect, possibly due to smoothing? What causes smearing in range?
- Very long period swell, 14-16 seconds, with a height of 0.48 m
- Direction of cross spectra on individual imagettes seams to change along SAR image. Possible refraction?
- http://surfweer.nl/surf/surfweer-maandag-2-januari-2017/#comments Surfer observations and web cam pictures show small swell on this day.

File	S1B_20170108T174048			
date	swath	orbit	lat - lon	heading
2017-01-08	IW3	Ascending	53.602, 2.432	350.866 deg
hm0	swell hm0	period Tp	wind speed	wind direction
0.89 m	0.48 m	14.29 s	3.32 m/s	222.1 deg

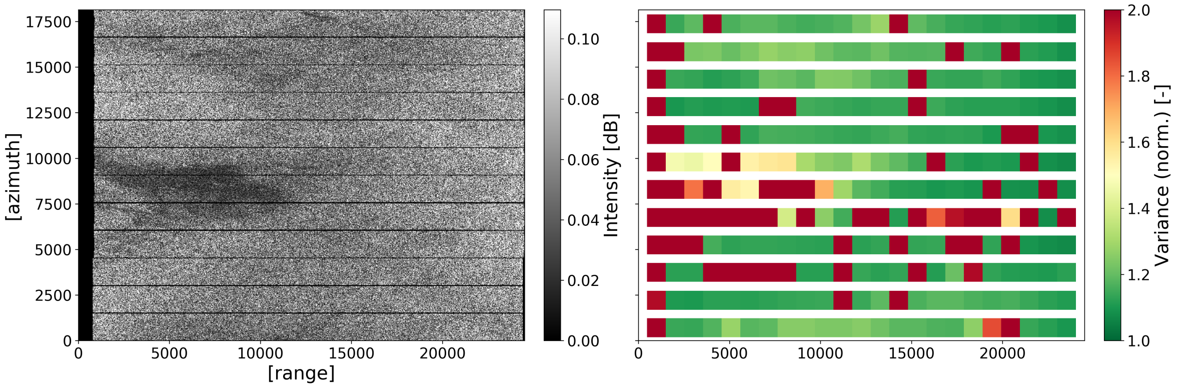

Figure B.36: Sentinel-1 SLC SAR image, acquired on 2017-01-08 17:40:48. Top left image shows the intensity (absolute) values of the 3rd sub-swath. Top right shows computed variance per 1024x1024 imagette of the same sub-swath.

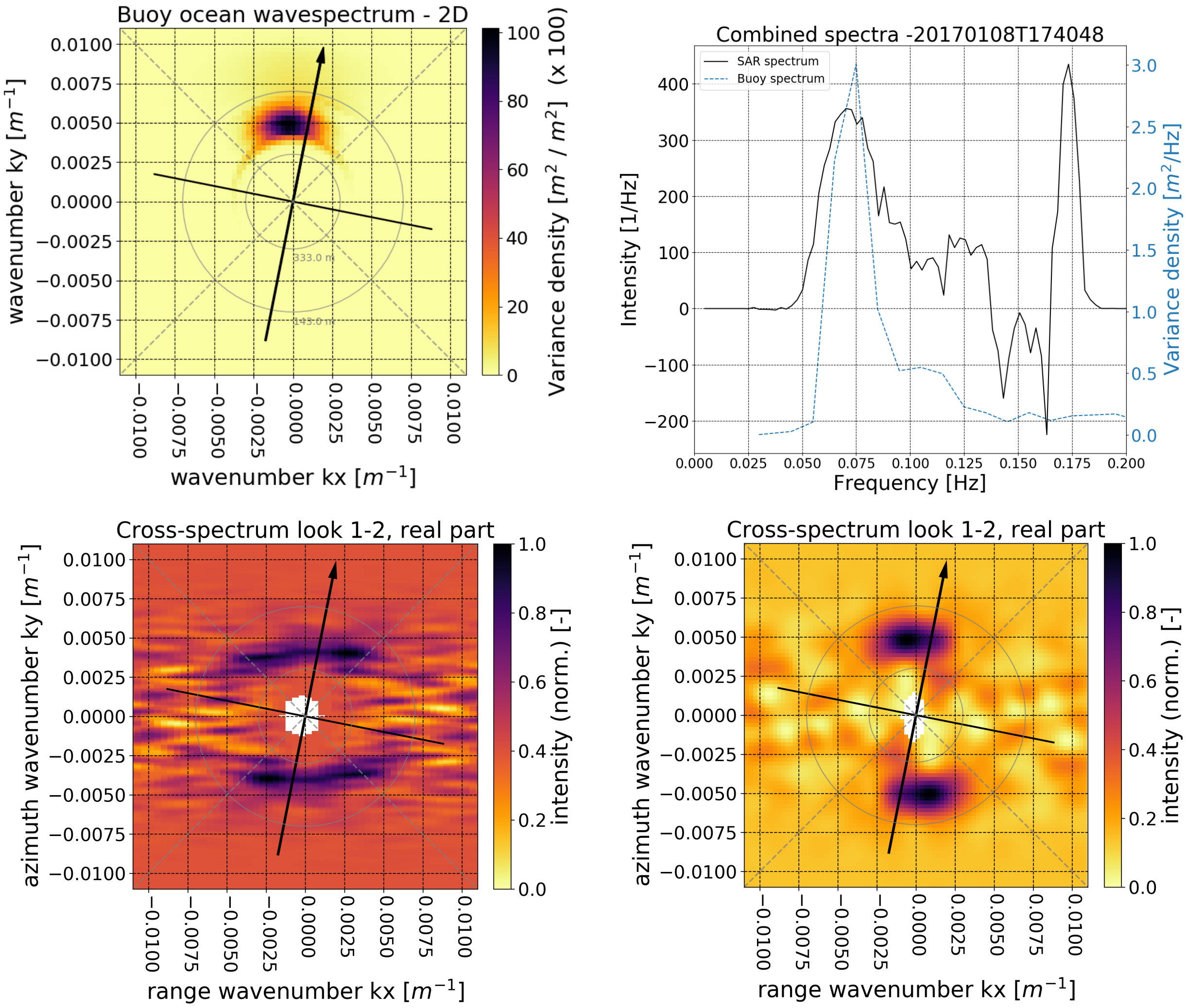

Figure B.37: The top left image shows IJ-geul buoy spectra, top right shows 1D buoy and SAR spectra from 8 January 2017. Bottom images show SAR image spectra (left) and OCEANSAR image spectra (right), between sub-look 1 and sub-look 2.

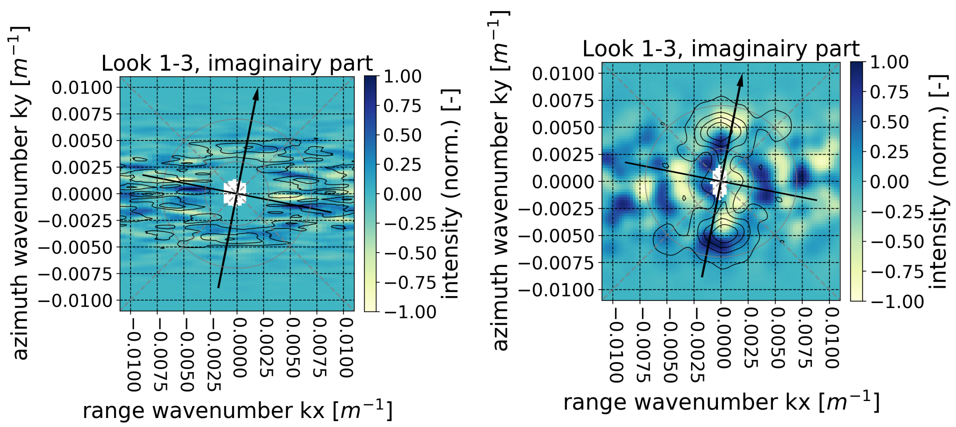

Figure B.38: Imaginary part of the cross spectrum between sub-look 1 and sub-look 3, contour lines show the real part of the cross spectrum. SAR image spectrum is plotted on the left and OCEANSAR spectrum on the right.

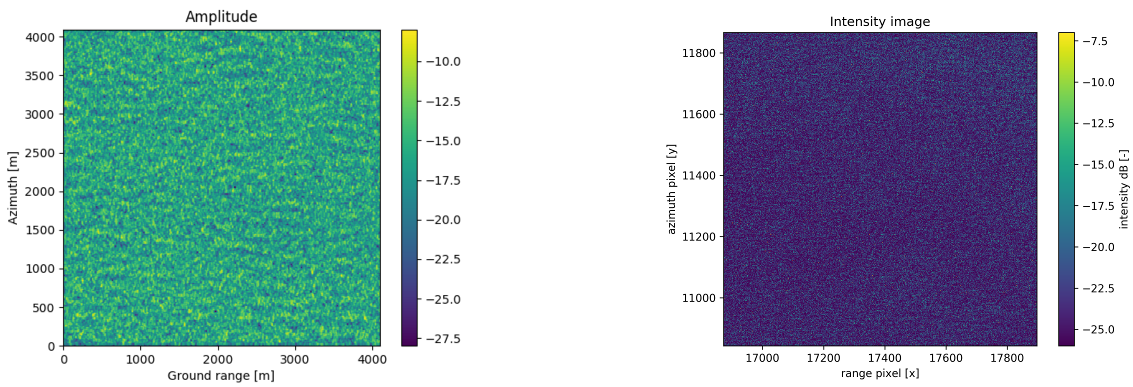

Figure B.39: Intensity (absolute values) images from the OCEANSAR imagette (left) and Sentinel-1 SLC imagette (right). The Sentinel-1 imagette was located at [7, 13] (number of subset in azimuth and range).

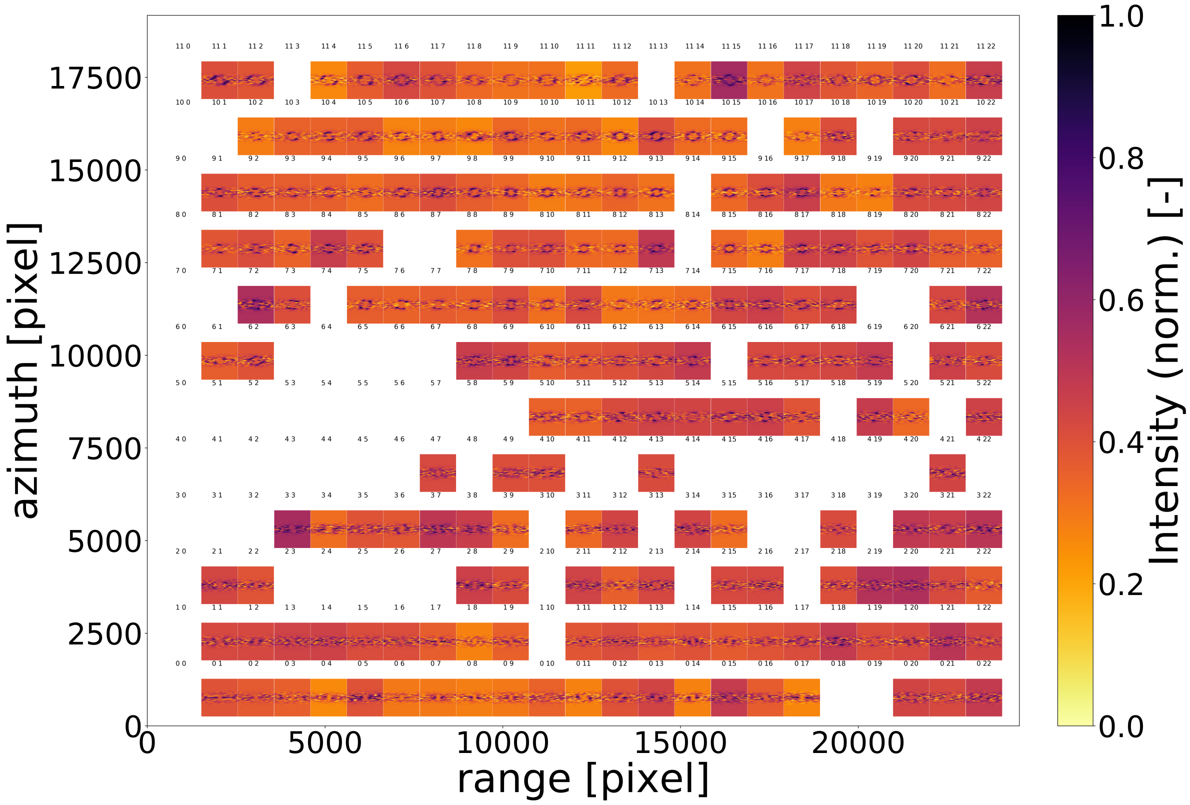

Figure B.40: Real part of the cross spectrum between sub-look 1 and sub-look 3 for different imagettes. size of each imagette is 1024x1024 pixels and the location in azimuth and range is displayed above it. When the computed variance of an imagette was too large, the imagette is white.

Test case 2017-01-09

– Negative result, swell waves are not observed on 1D and 2D buoy spectra. SAR cross spectra only shows non-linear effects no quasi-linear part. High significant wave height (2.13 m), low swell wave height.

– Very strong winds,

– Although the 1D spectra seam to correlate due to the non-linear contribution, this is most likely random noise (speckle)

File	S1A_20170109T173321			
date 2017-01-09	swath IW2	orbit Ascending	lat - lon 53.624, 3.244	heading 349.87 deg
hm0 2.13 m	swell hm0 0.30 m	period Tp 6.25 s	wind speed 13.37 m/s	wind direction 216.5 deg

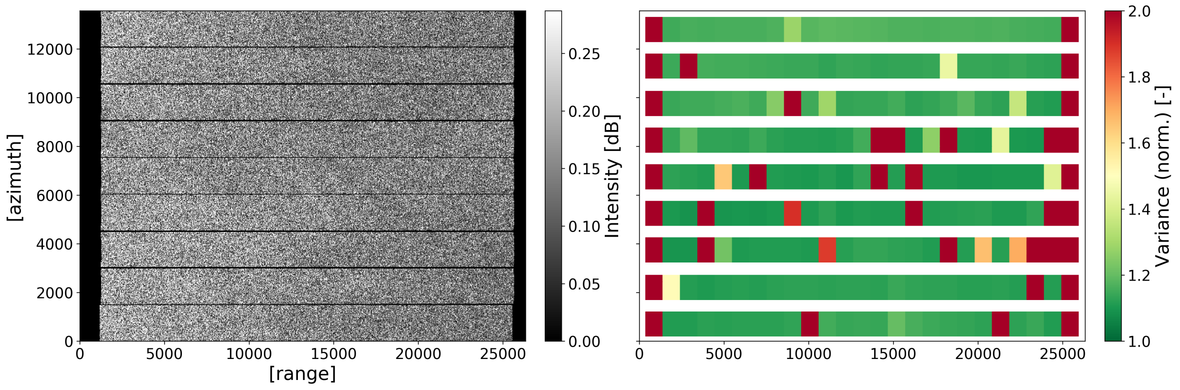

Figure B.41: Sentinel-1 SLC SAR image, acquired on 2017-01-09 17:33:21. Top left image shows the intensity (absolute) values of the 2nd sub-swath. Top right shows computed variance per 1024x1024 imagette of the same sub-swath.

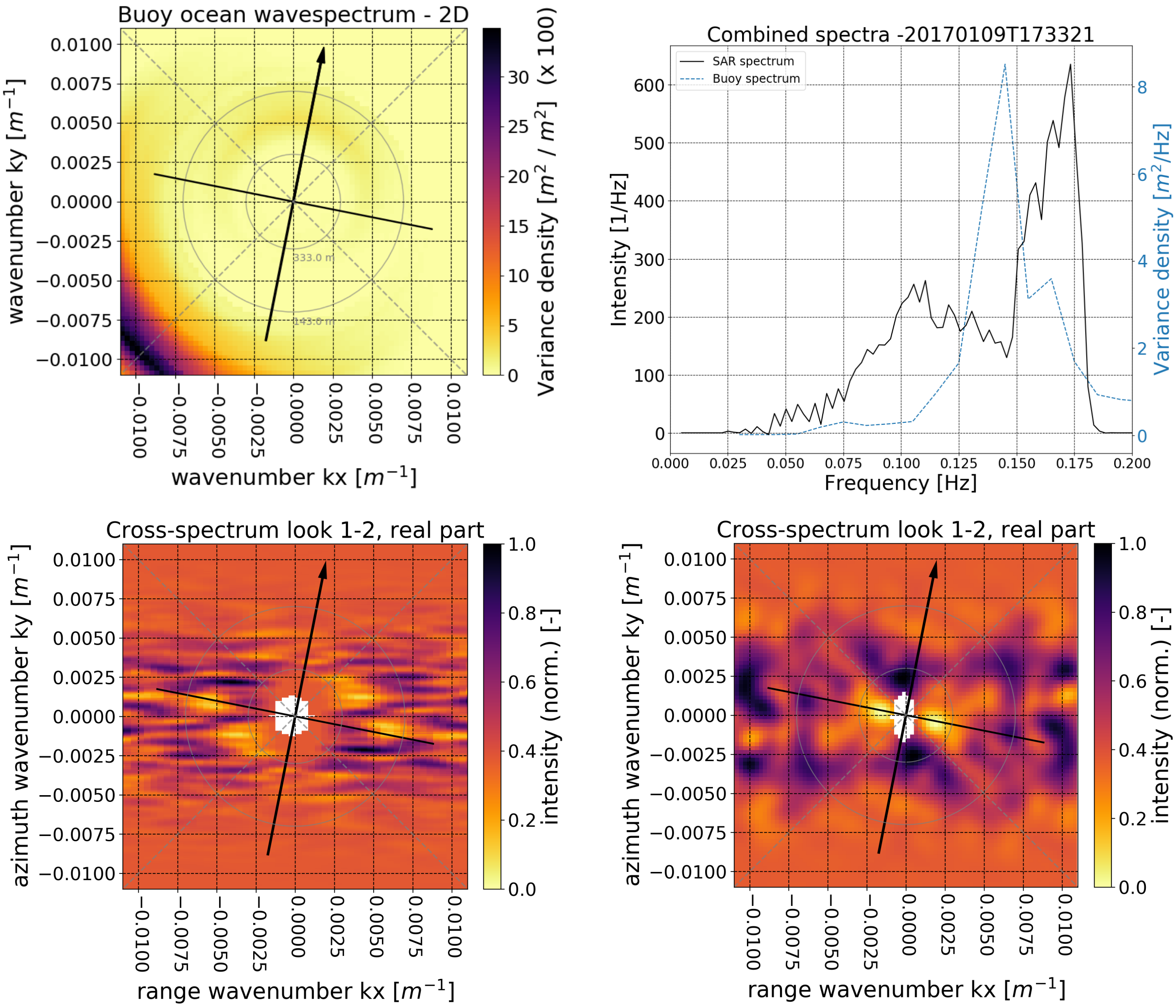

Figure B.42: The top left image shows IJ-geul buoy spectra, top right shows 1D buoy and SAR spectra from 09 January 2017. Bottom images show SAR image spectra (left) and OCEANSAR image spectra (right), between sub-look 1 and sub-look 2.

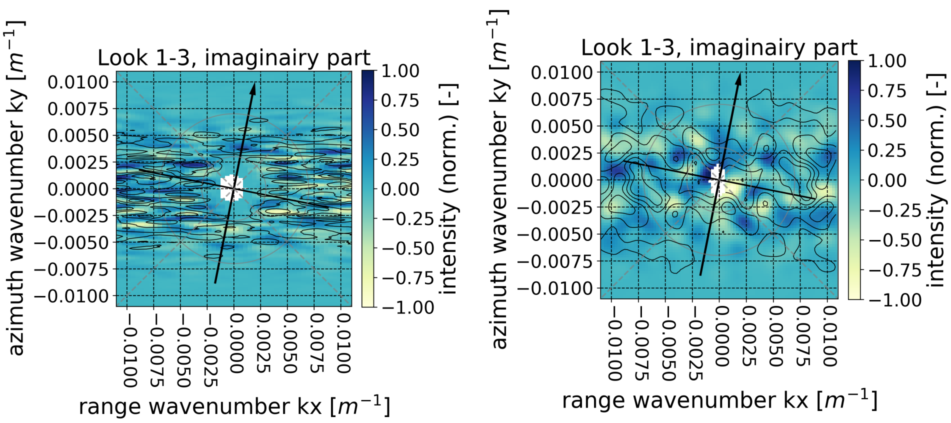

Figure B.43: Imaginary part of the cross spectrum between sub-look 1 and sub-look 3, contour lines show the real part of the cross spectrum. SAR image spectrum is plotted on the left and OCEANSAR spectrum on the right.

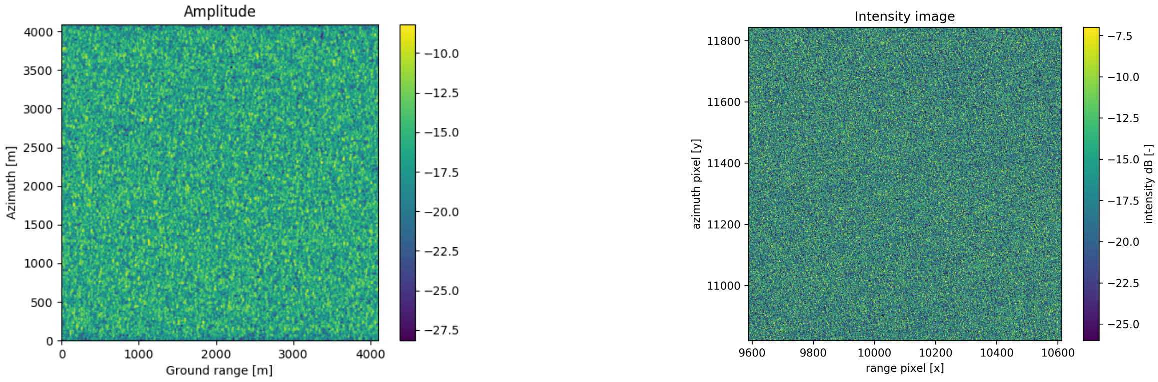

Figure B.44: Intensity (absolute values) images from the OCEANSAR imagette (left) and Sentinel-1 SLC imagette (right). The Sentinel-1 imagette was located at [7, 9] (number of subset in azimuth and range).

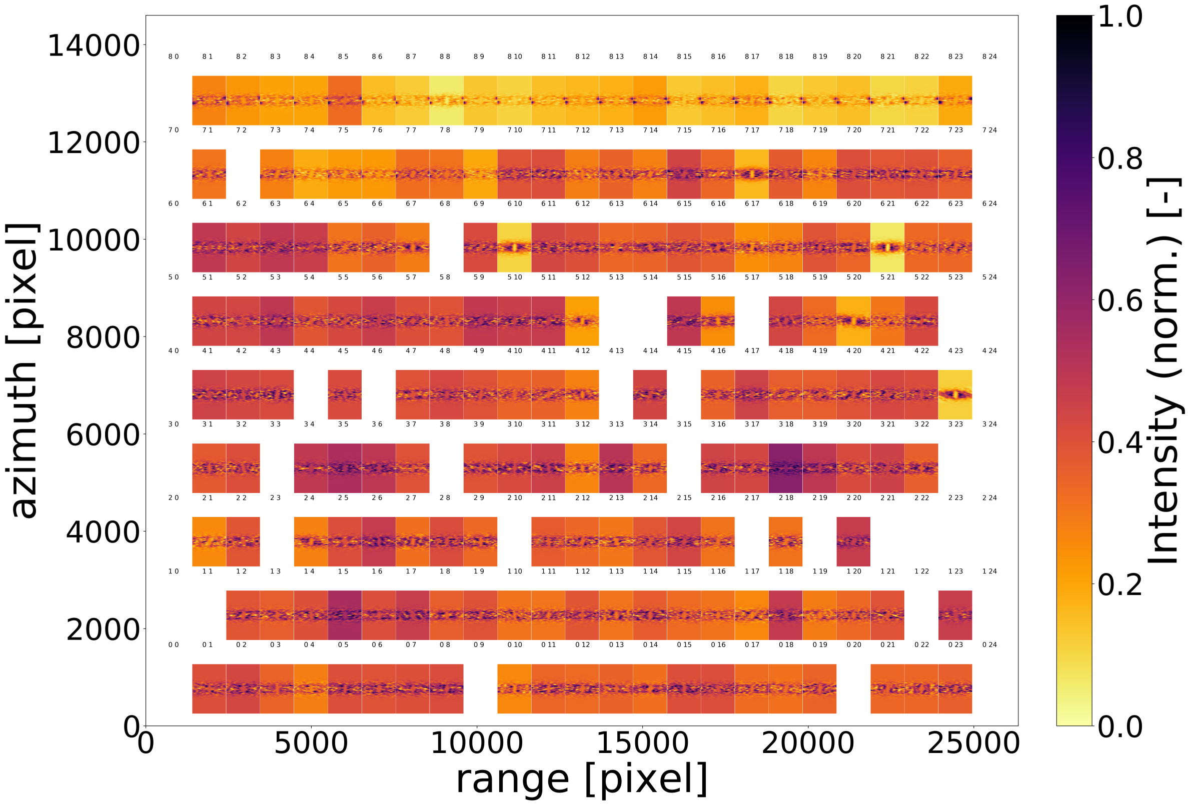

Figure B.45: Real part of the cross spectrum between sub-look 1 and sub-look 3 for different imagettes. size of each imagette is 1024x1024 pixels and the location in azimuth and range is displayed above it. When the computed variance of an imagette was too large, the imagette is white.

Test case 2017-01-16

- Positive result, clear quasi-linear swell peak observable on SAR imagettes cross spectra. Swell peak around $ky = 0.0051/m$ matches both SAR and OCEANSAR peak. Direction of buoy peak is different compared to SAR measurement. Possible due to refraction of the relatively long swell waves. Buoy measurements were taken at the IJgeul wave buoy, which is located in more shallow water compared to the K13 alpha buoy.
- OCEANSAR results show a slightly different direction compared to wave buoy data.
- Local surf observations show pictures of a flat ocean surface with clear swell. http://surfweer.nl/surf/surfweer-zaterdag-14-januari-2016/

File	S1A_20170116T172512			
date	swath	orbit	lat - lon	heading
2017-01-16	IW1	Ascending	53.649, 3.931	348.79 deg
hm0	swell hm0	period Tp	wind speed	wind direction
0.94 m	0.58 m	14.29 s	3.73 m/s	134.3 deg

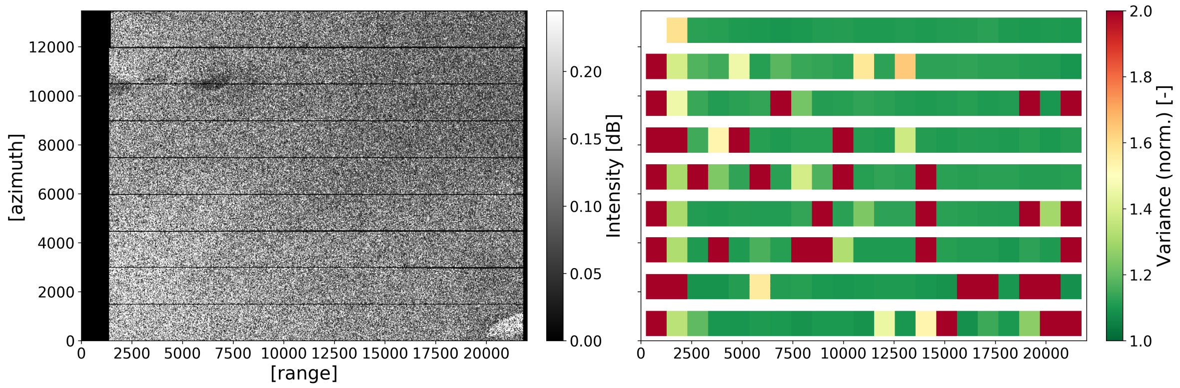

Figure B.46: Sentinel-1 SLC SAR image, acquired on 2017-01-16 17:25:12. Top left image shows the intensity (absolute) values of the 1st sub-swath. Top right shows computed variance per 1024x1024 imagette of the same sub-swath.

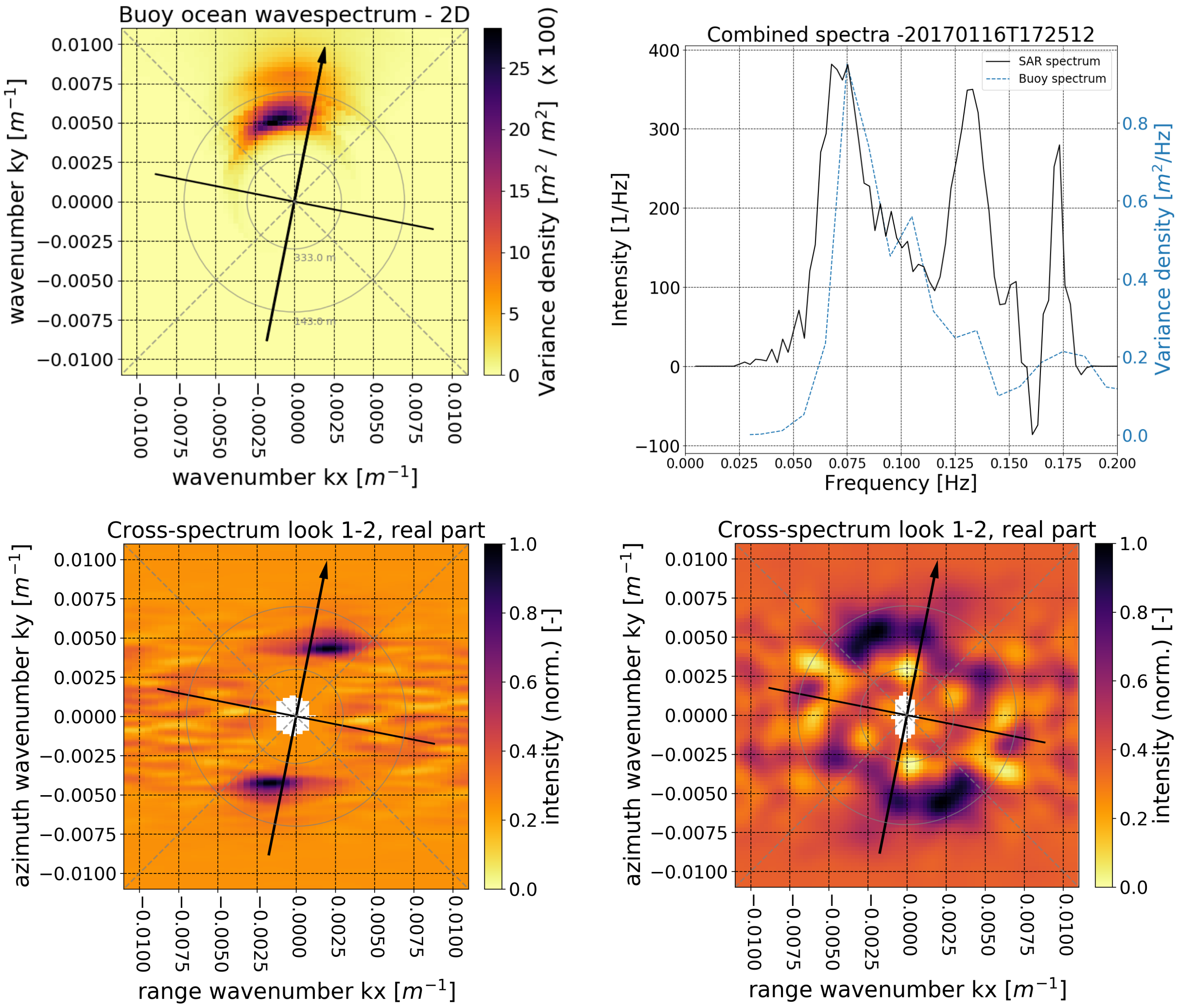

Figure B.47: The top left image shows IJ-geul buoy spectra, top right shows 1D buoy and SAR spectra from 16 January 2017. Bottom images show SAR image spectra (left) and OCEANSAR image spectra (right), between sub-look 1 and sub-look 2.

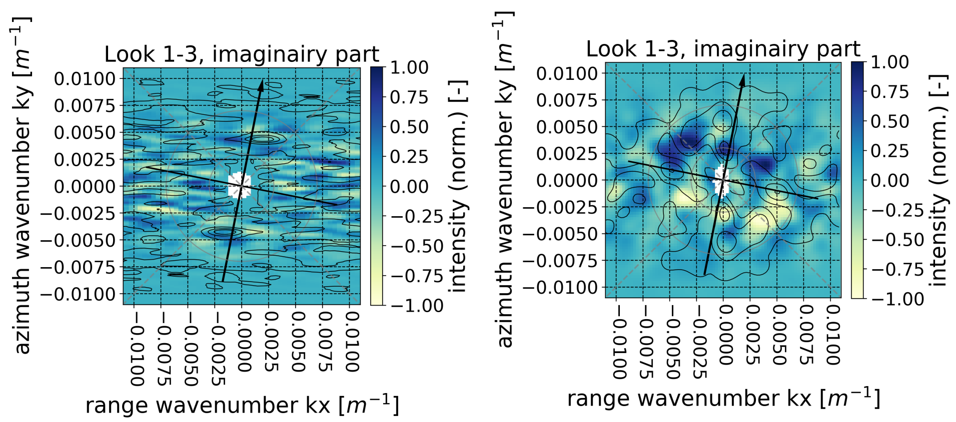

Figure B.48: Imaginary part of the cross spectrum between sub-look 1 and sub-look 3, contour lines show the real part of the cross spectrum. SAR image spectrum is plotted on the left and OCEANSAR spectrum on the right.

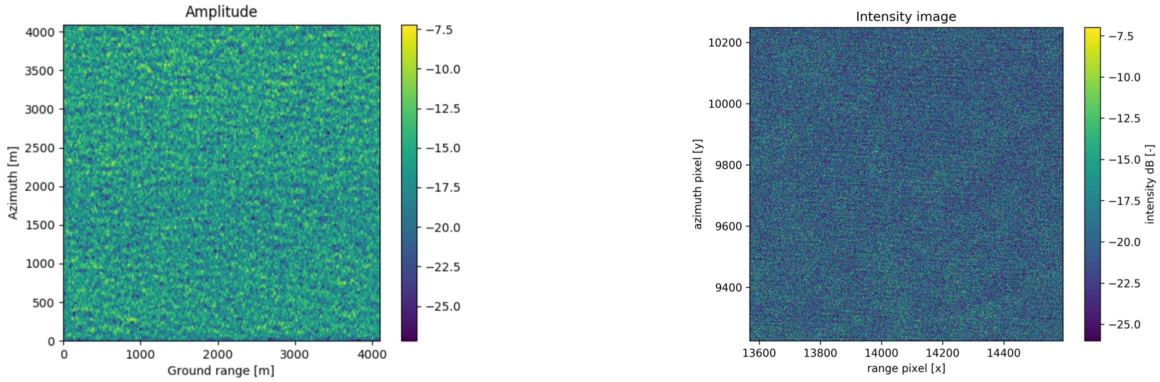

Figure B.49: Intensity (absolute values) images from the OCEANSAR imagette (left) and Sentinel-1 SLC imagette (right). The Sentinel-1 imagette was located at [6, 13] (number of subset in azimuth and range).

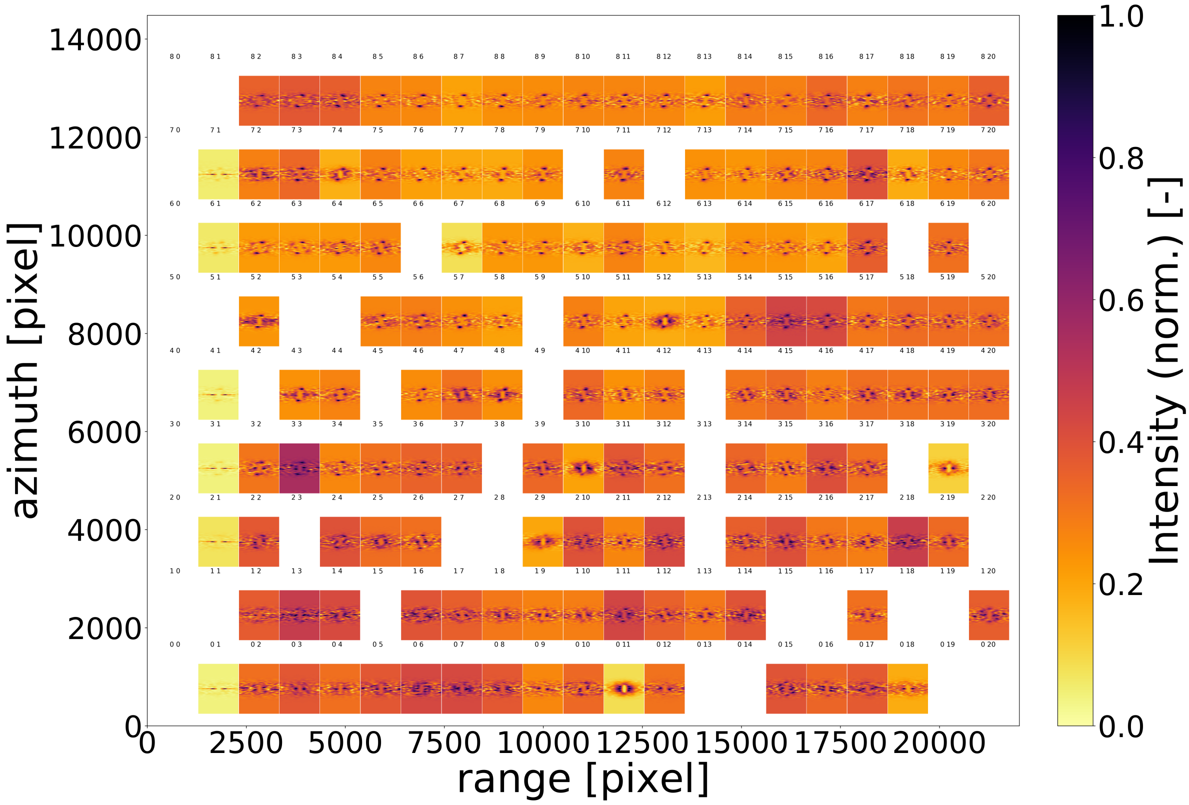

Figure B.50: Real part of the cross spectrum between sub-look 1 and sub-look 3 for different imagettes. size of each imagette is 1024x1024 pixels and the location in azimuth and range is displayed above it. When the computed variance of an imagette was too large, the imagette is white.

Test case 2017-01-21

- Negative result, imagette cross spectra do not show a quasi-linear swell peak. Mostly a non-linear contribution from wind waves. 2D spectra does show a swell peak. Swell height probably too low, or disturbed by the presence of wind waves.
- Surfer observations do not mention any presence of swell on this day. http://surfweer.nl/surf/surfweer-zaterdag-14-januari-2
#comments

File	S1A_20170121T173321			
date	swath	orbit	lat - lon	heading
2017-01-21	IW2	Ascending	53.564, 3.242	349.869 deg
hm0	swell hm0	period Tp	wind speed	wind direction
0.79 m	0.34 m	11.11 s	5.16 m/s	100.6 deg

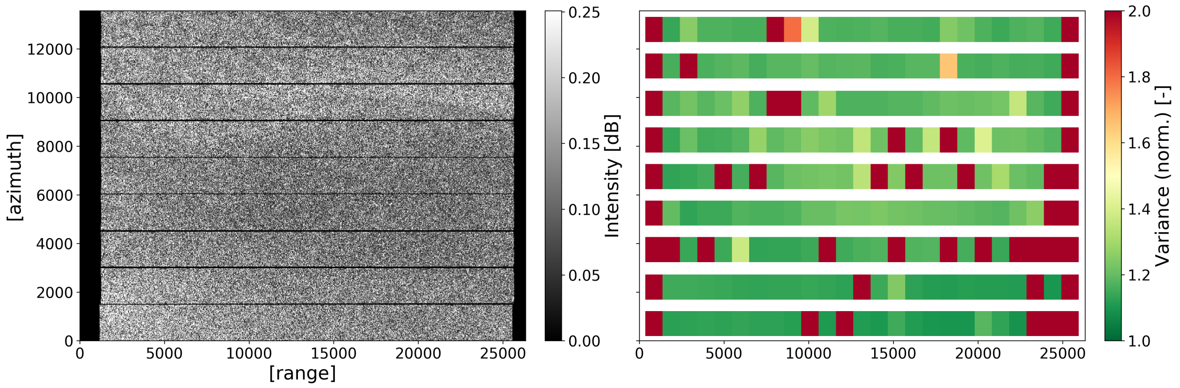

Figure B.51: Sentinel-1 SLC SAR image, acquired on 2017-01-21 17:33:21. Top left image shows the intensity (absolute) values of the 2nd sub-swath. Top right shows computed variance per 1024x1024 imagette of the same sub-swath.

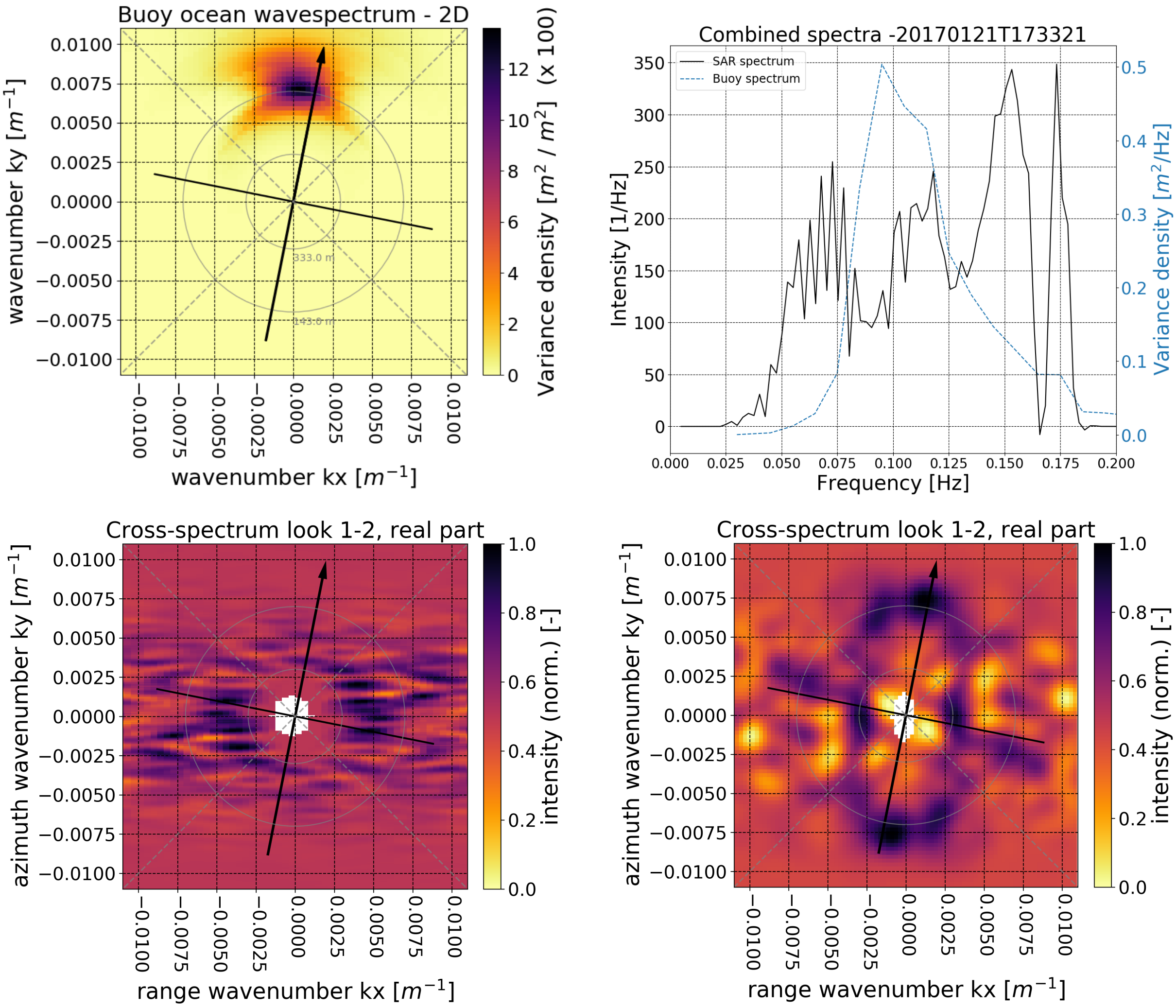

Figure B.52: The top left image shows IJ-geul buoy spectra, top right shows 1D buoy and SAR spectra from 21 January 2017. Bottom images show SAR image spectra (left) and OCEANSAR image spectra (right), between sub-look 1 and sub-look 2.

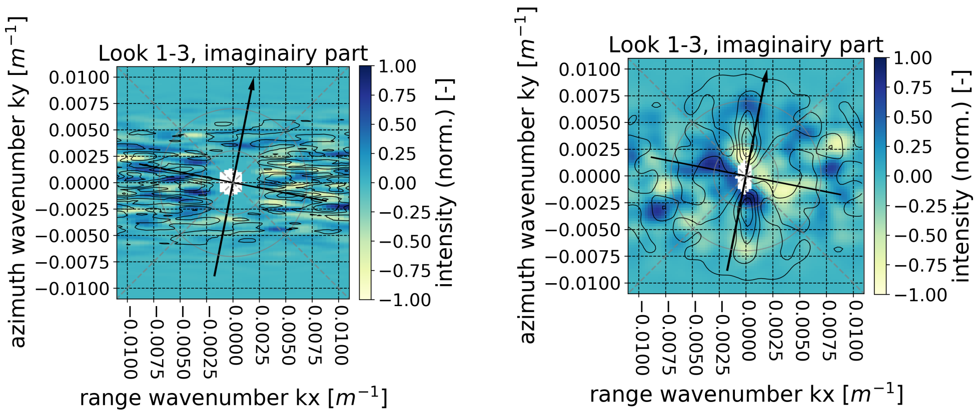

Figure B.53: Imaginary part of the cross spectrum between sub-look 1 and sub-look 3, contour lines show the real part of the cross spectrum. SAR image spectrum is plotted on the left and OCEANSAR spectrum on the right.

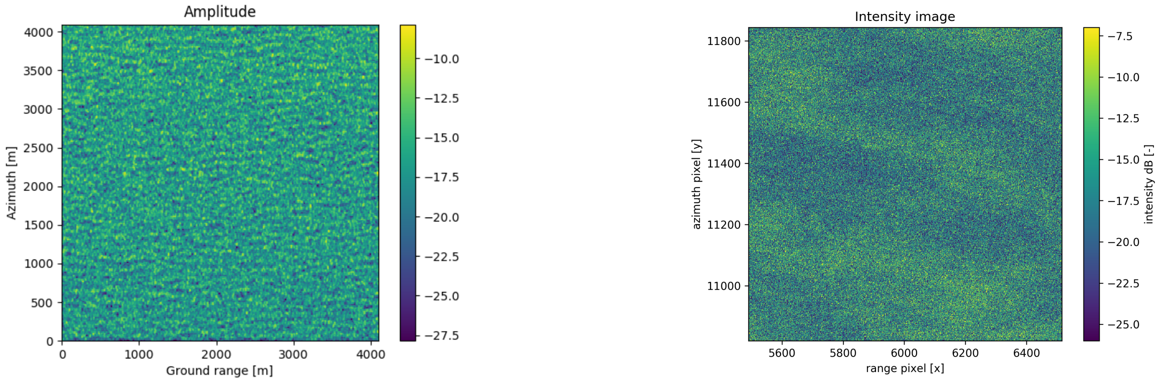

Figure B.54: Intensity (absolute values) images from the OCEANSAR imagette (left) and Sentinel-1 SLC imagette (right). The Sentinel-1 imagette was located at [7,5] (number of subset in azimuth and range).

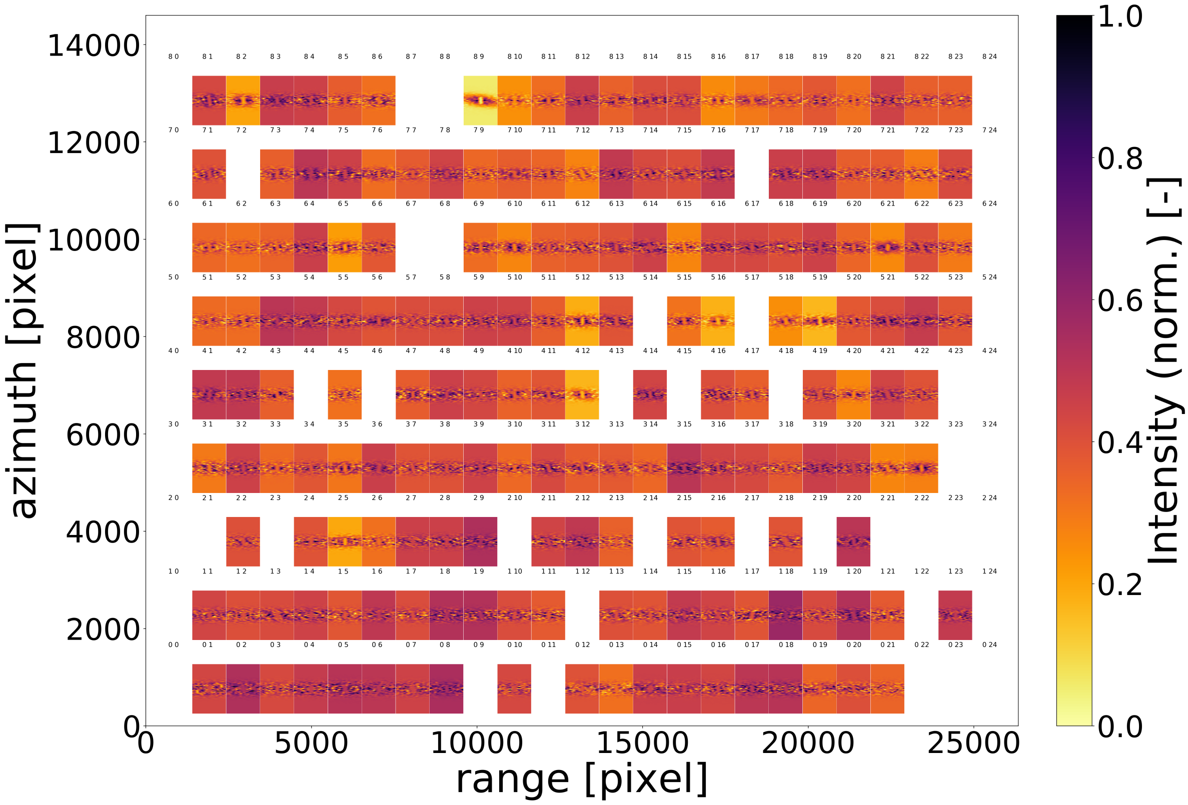

Figure B.55: Real part of the cross spectrum between sub-look 1 and sub-look 3 for different imagettes. size of each imagette is 1024x1024 pixels and the location in azimuth and range is displayed above it. When the computed variance of an imagette was too large, the imagette is white.

Test cases: Portugal

Test case 2014-11-25

- Monican 1 buoy measurements from 2014-11-25 showed a significant wave height of 2.1 m and a period of 17 seconds from a NW direction, corresponding to a wave length of approximately 400 m, with a wave number of 0.0025 [1/m]. Figure B.57 shows the ocean wave spectrum at the Monican 1 wave buoy with a peak at kx = 0.002 1/m and ky = 0.002 1/m, resulting in a wave number k = 0.0028 1/m 357 m.

- By counting pixels and using known range and azimuth pixel resolution a first estimate of the wave length could be made, which was about 400 m. **??** shows the SLC image swath within which the Monican 1 wave buoy was located and the computed variance. The image was divided in subsets of 1024x1024 pixels (or 2 x 12 km) which were subsequently processed, the variance of each subset was calculated using Equation 3.16.

- The cross spectrum from **??** shows a peak near a wavenumber of kx = 0.0025 1/m and ky = 0.0017 1/m, resulting in k = 0.003 1/m or 331 m, which is slightly different compared to the peak wave number from the buoy data (k = 0.0028 1/m). Taking flipping of the SLC image along the y-axis into account, a difference in direction θ of 10.8° is observed. The next step was simulating the SAR radar image with OCEANSAR using Monican 1 wave buoy data from **??**. After simulating the ocean surface, the cross spectrum was also calculated for the simulated SAR image, resulting in **??**. Two peaks can be observed, where the main peak is observed at kx = 0.0028 1/m and ky = 0.0012 1/m, resulting in a wavenumber of k = 0.003 1/m. The direction is again slightly different compared to buoy data, a different θ of 21.8° is observed.

- 1D buoy and SAR spectra both show a clear peak.

File	S1A_20141125T183457			
date	swath	orbit	lat - lon	heading
2014-11-25	IW2	Ascending	38.9494 , -9.479	349.99 deg
hm0	period Tp	wave dir.	wind speed	wind dir.
2.05 m	17.28 s	316.7 deg	5.05 m/s	294.7 deg

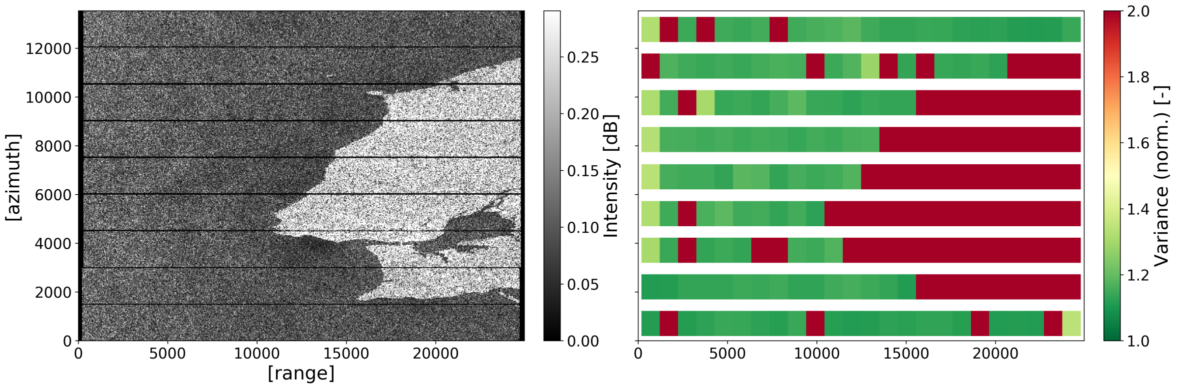

Figure B.56: Sentinel-1 SLC SAR image, acquired on 2014-11-25 18:34:57. Top left image shows the intensity (absolute) values of the 2nd sub-swath. Top right shows computed variance per 1024x1024 imagette of the same sub-swath.

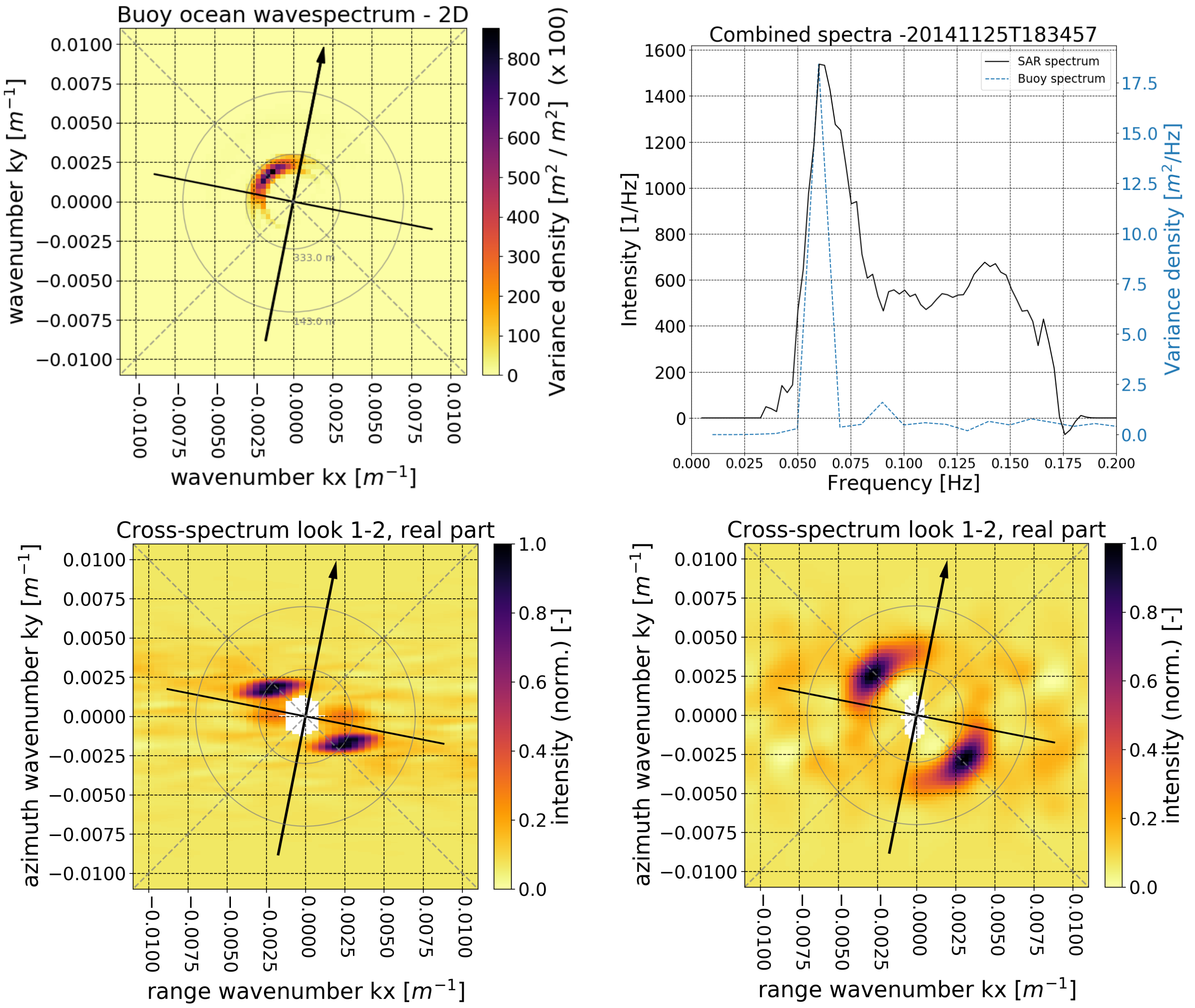

Figure B.57: The top left image shows Monican 1 buoy spectra, top right shows 1D buoy and SAR spectra from 25 November 2014. Bottom images show SAR image spectra (left) and OCEANSAR image spectra (right), between sub-look 1 and sub-look 2.

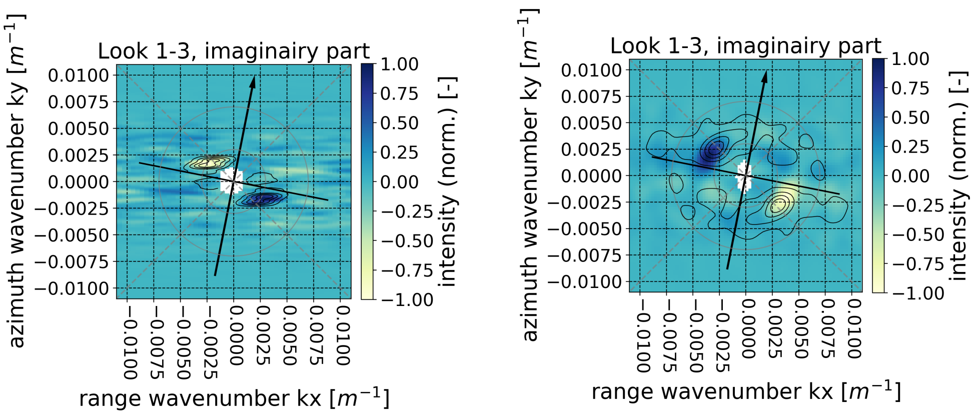

Figure B.58: Imaginary part of the cross spectrum between sub-look 1 and sub-look 3, contour lines show the real part of the cross spectrum. SAR image spectrum is plotted on the left and OCEANSAR spectrum on the right.

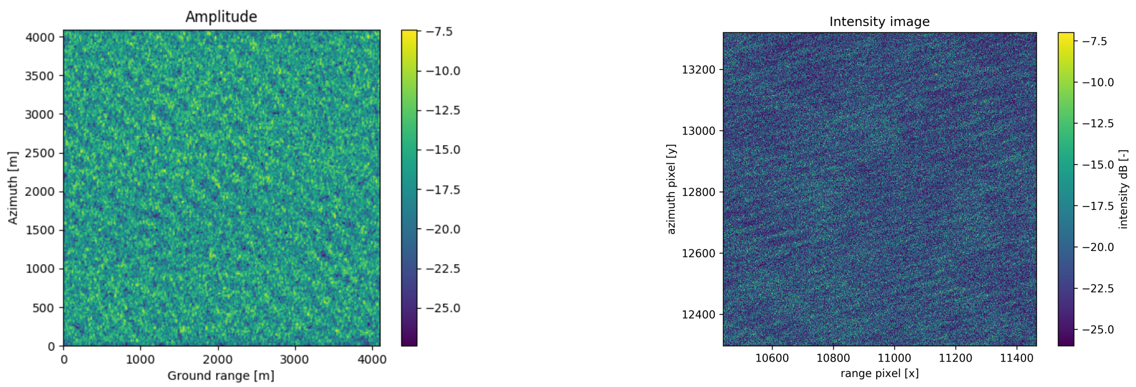

Figure B.59: Intensity (absolute values) images from the OCEANSAR imagette (left) and Sentinel-1 SLC imagette (right). The Sentinel-1 imagette was located at [8, 10] (number of subset in azimuth and range).

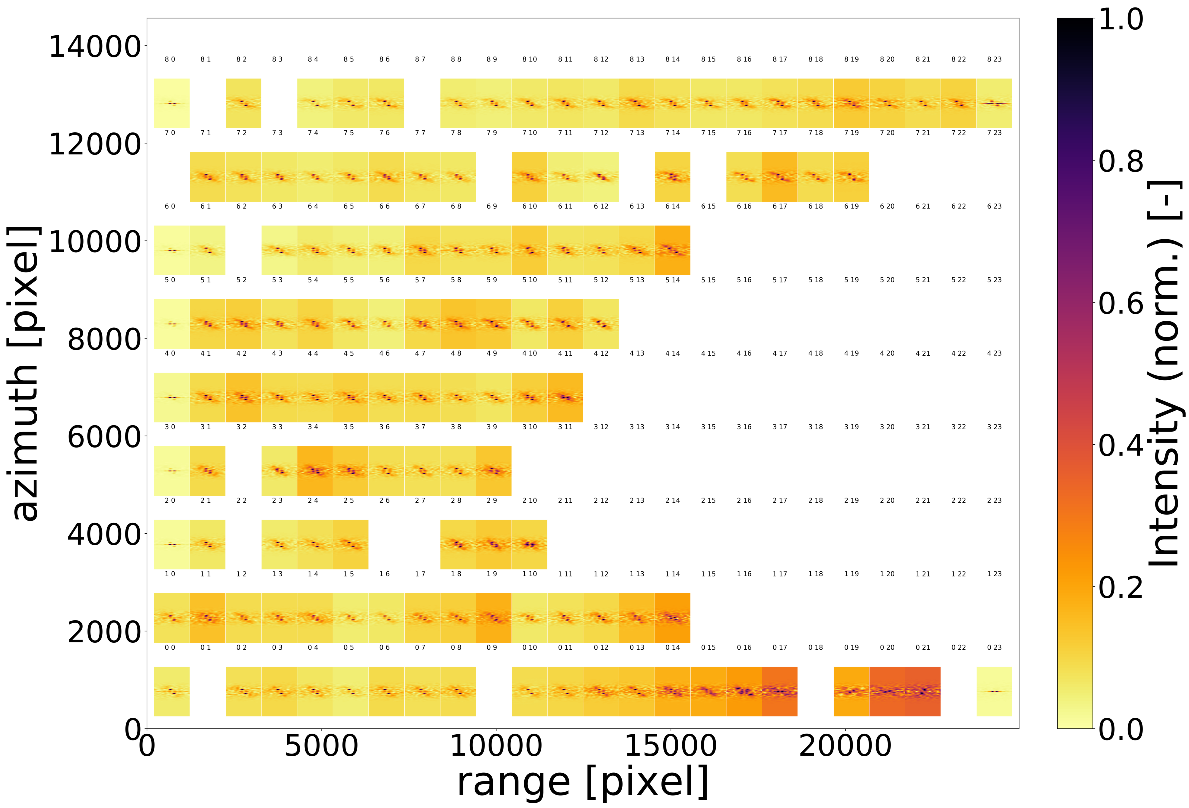

Figure B.60: Real part of the cross spectrum between sub-look 1 and sub-look 3 for different imagettes. size of each imagette is 1024x1024 pixels and the location in azimuth and range is displayed above it. When the computed variance of an imagette was too large, the imagette is white.

Test case 2015-01-24

- Positive result, spectral retrieval possible in most imagettes cross spectra. Cross spectra do show a non-linear contribution from wind.
- Direction of buoy observations is slightly different compared to SAR cross spectra.
- Buoy spectra show significant spreading of the swell spectrum. This is also observed on multiple SAR images.
- 1D spectrum from SAR imagette show a shift of the peak to higher frequencies.

File	S1A_20150124T183456			
date	swath	orbit	lat - lon	heading
2015-01-24	IW2	Ascending	38.9497, -9.480	349.997 deg
hm0	period Tp	wave dir.	wind speed	wind dir.
1.72 m	10.88 s	346.6 deg	8.43 m/s	25.8 deg

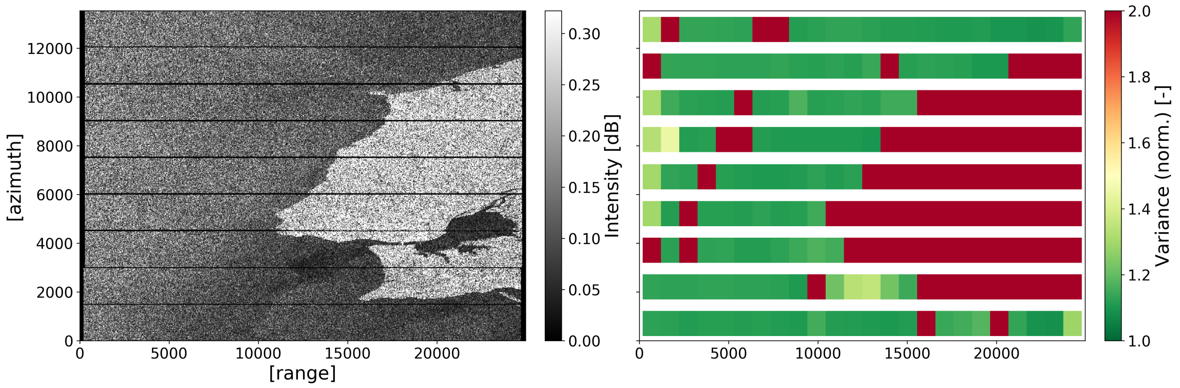

Figure B.61: Sentinel-1 SLC SAR image, acquired on 2015-01-24 18:34:56. Top left image shows the intensity (absolute) values of the 2nd sub-swath. Top right shows computed variance per 1024x1024 imagette of the same sub-swath.

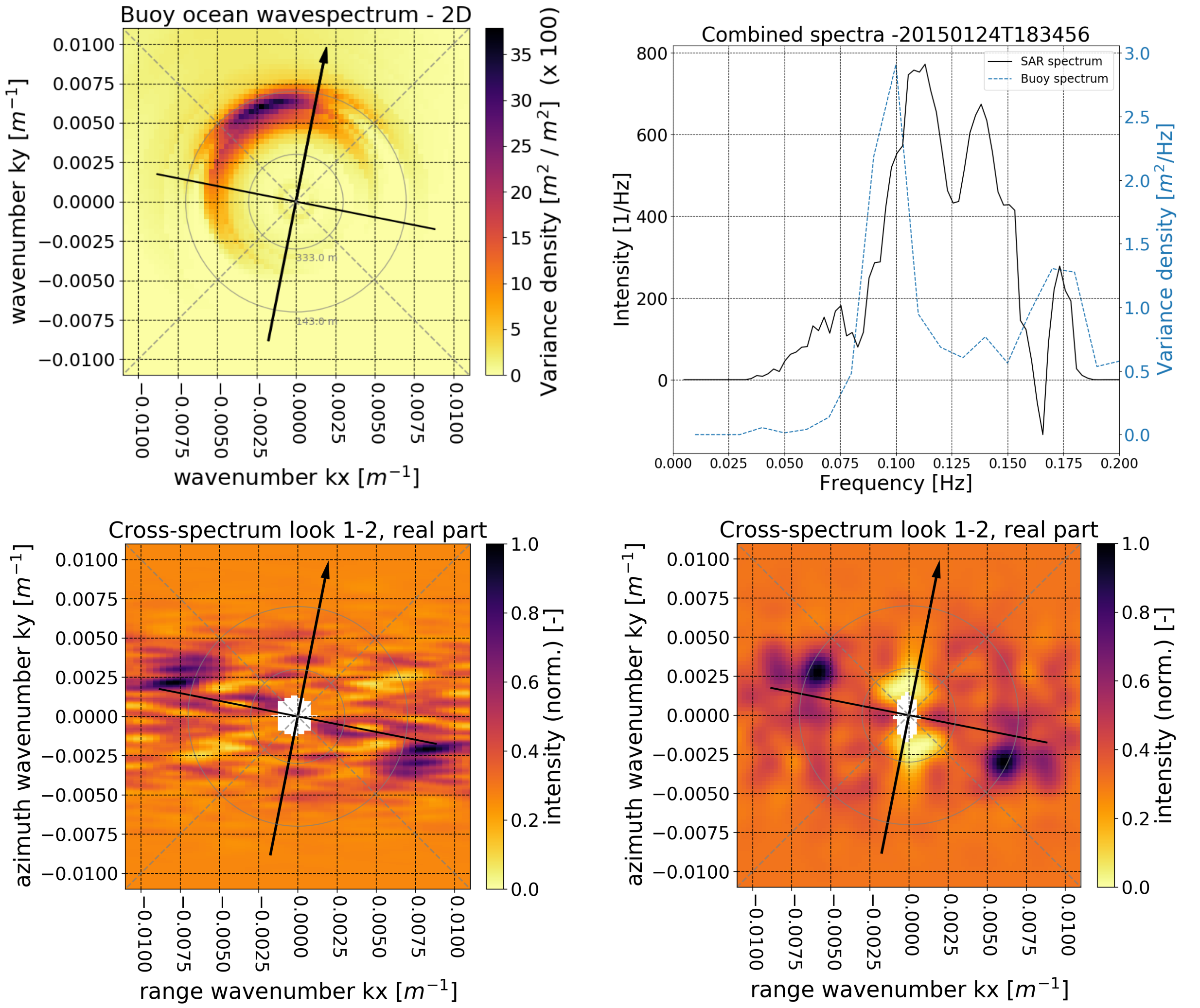

Figure B.62: The top left image shows Monican 1 buoy spectra, top right shows 1D buoy and SAR spectra from 24 January 2015. Bottom images show SAR image spectra (left) and OCEANSAR image spectra (right), between sub-look 1 and sub-look 2.

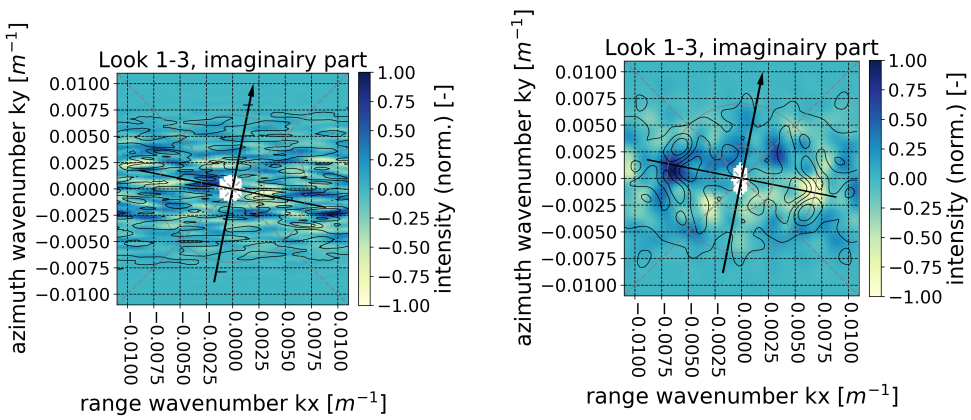

Figure B.63: Imaginary part of the cross spectrum between sub-look 1 and sub-look 3, contour lines show the real part of the cross spectrum. SAR image spectrum is plotted on the left and OCEANSAR spectrum on the right.

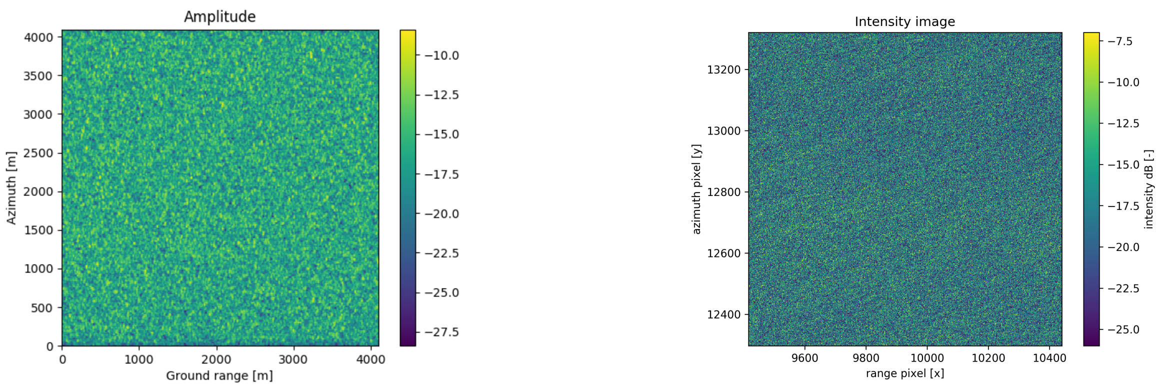

Figure B.64: Intensity (absolute values) images from the OCEANSAR imagette (left) and Sentinel-1 SLC imagette (right). The Sentinel-1 imagette was located at [8, 9] (number of subset in azimuth and range).

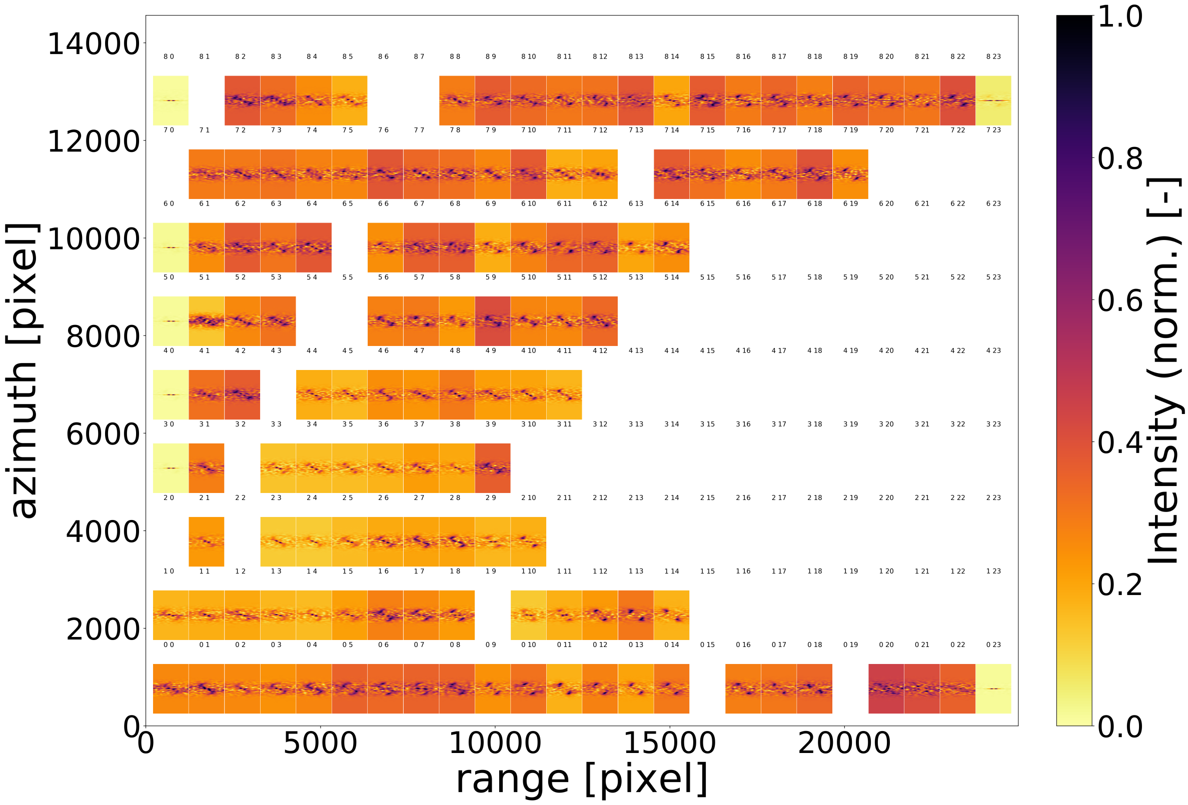

Figure B.65: Real part of the cross spectrum between sub-look 1 and sub-look 3 for different imagettes. size of each imagette is 1024x1024 pixels and the location in azimuth and range is displayed above it. When the computed variance of an imagette was too large, the imagette is white.

Test case 2015-10-27

- Positive result, quasi-linear swell peak visible on all imagette cross spectra. Several SAR cross spectra show an elongated swell peak in range direction. A possible explanation is the effect of smoothing on a rectangular pixel.
- SAR swell peak on 2D matches well with buoy spectra in both wave number and direction. When we investigate the 1D spectrum, it is seen that due to smoothing of the signal, the spectrum is distributed along higher frequencies.

File	S1A_20151027T183506			
date 2015-10-27	swath IW2	orbit Ascending	lat - lon 39.115, -9.507	heading 350.007 deg
hm0 4.92 m	period Tp 15.84 s	wave dir. 312.1 deg	wind speed 7.97 m/s	wind dir. 238.3 deg

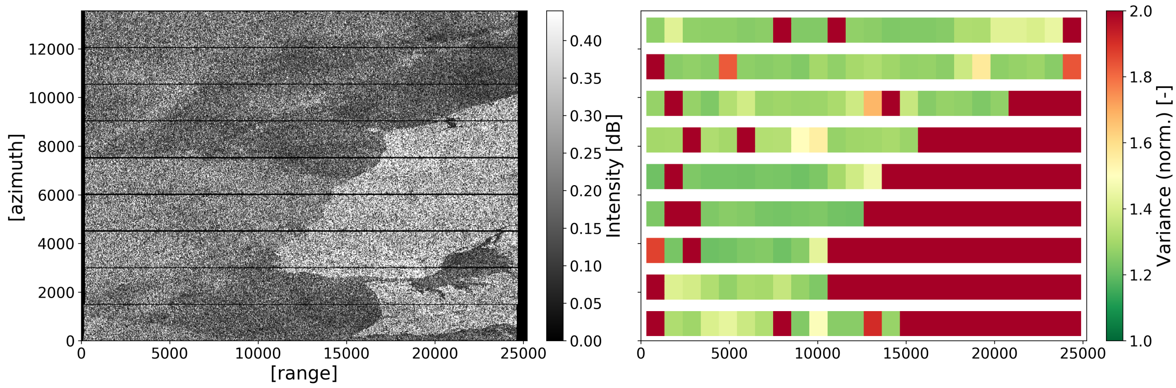

Figure B.66: Sentinel-1 SLC SAR image, acquired on 2015-10-27 18:35:06. Top left image shows the intensity (absolute) values of the 2nd sub-swath. Top right shows computed variance per 1024x1024 imagette of the same sub-swath.

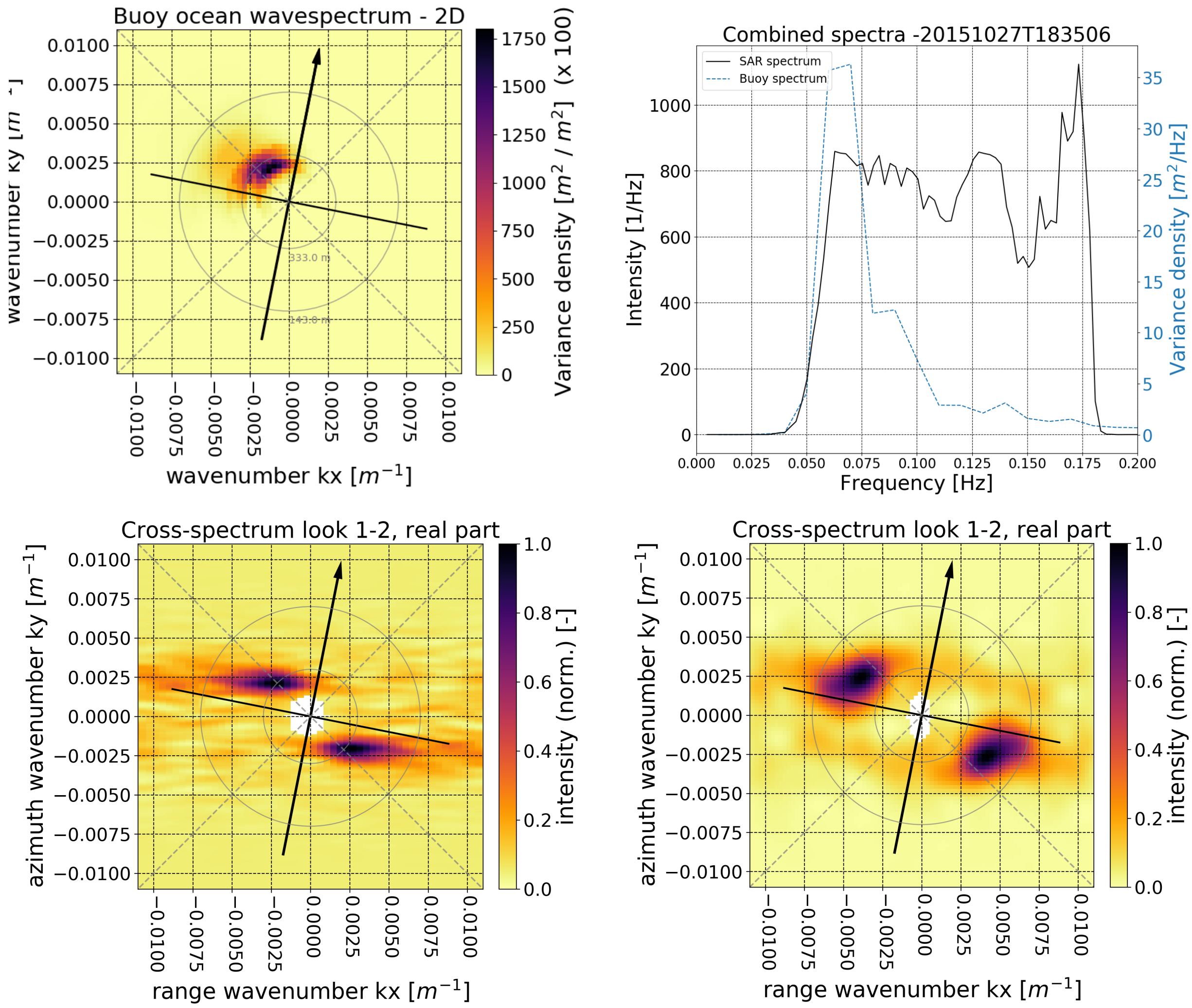

Figure B.67: The top left image shows Monican 1 buoy spectra, top right shows 1D buoy and SAR spectra from 27 October 2015. Bottom images show SAR image spectra (left) and OCEANSAR image spectra (right), between sub-look 1 and sub-look 2.

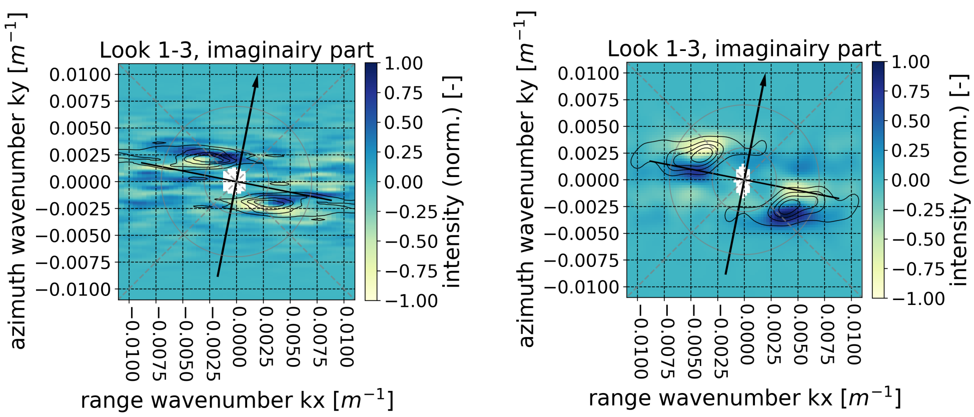

Figure B.68: Imaginary part of the cross spectrum between sub-look 1 and sub-look 3, contour lines show the real part of the cross spectrum. SAR image spectrum is plotted on the left and OCEANSAR spectrum on the right.

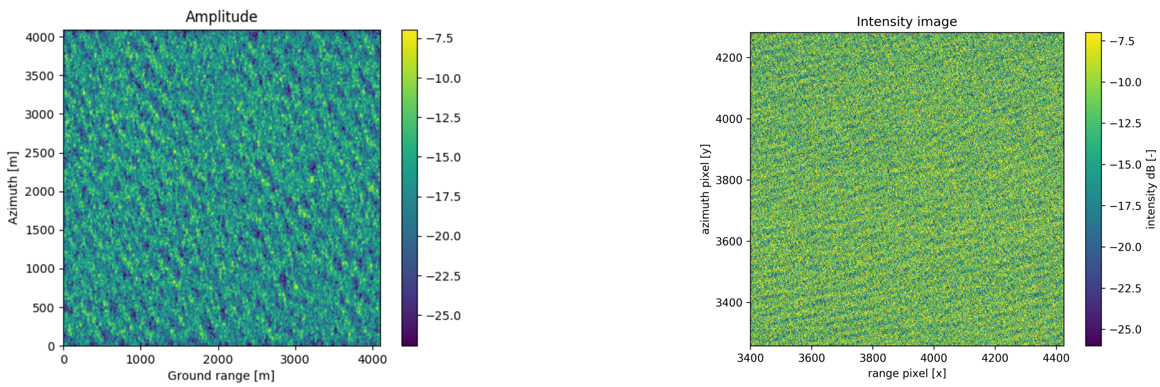

Figure B.69: Intensity (absolute values) images from the OCEANSAR imagette (left) and Sentinel-1 SLC imagette (right). The Sentinel-1 imagette was located at [2, 3] (number of subset in azimuth and range).

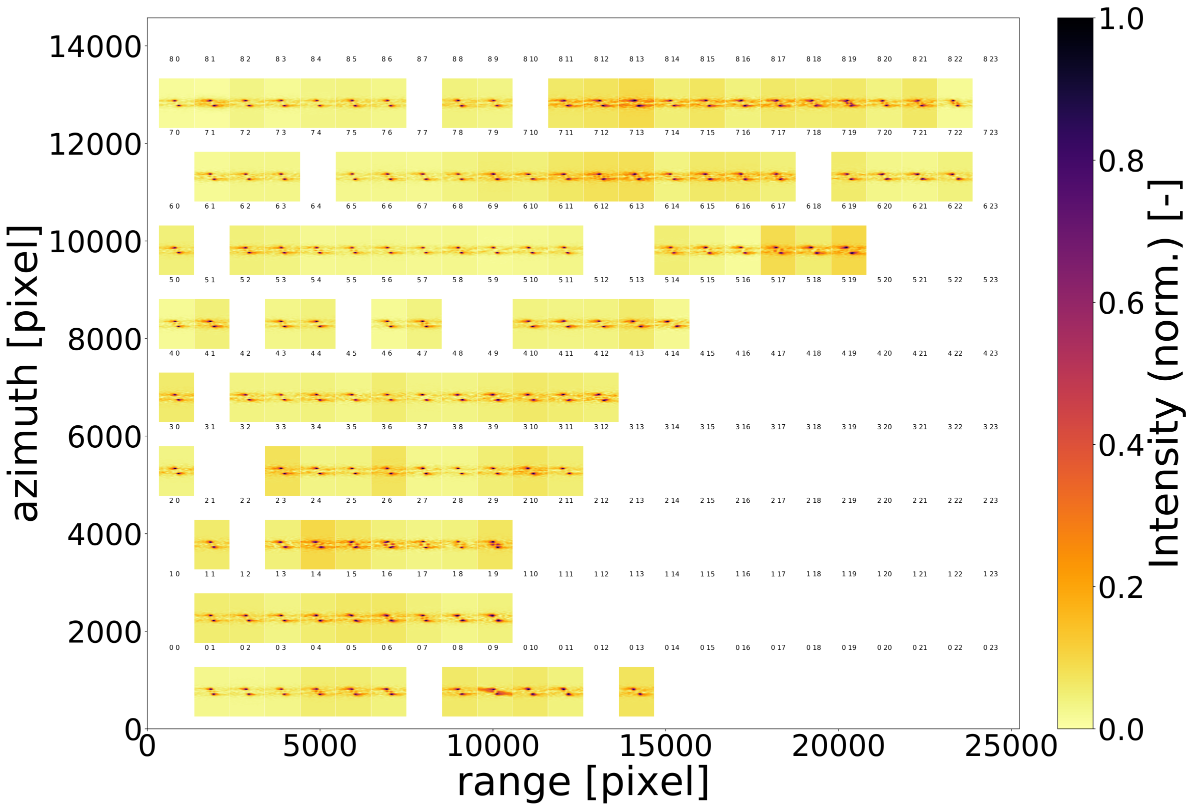

Figure B.70: Real part of the cross spectrum between sub-look 1 and sub-look 3 for different imagettes. size of each imagette is 1024x1024 pixels and the location in azimuth and range is displayed above it. When the computed variance of an imagette was too large, the imagette is white.

C

Hydrodynamic conditions

This appendix contains buoy data showing different hydrodynamic conditions during test cases in the North Sea and Portugal.

North Sea buoy data

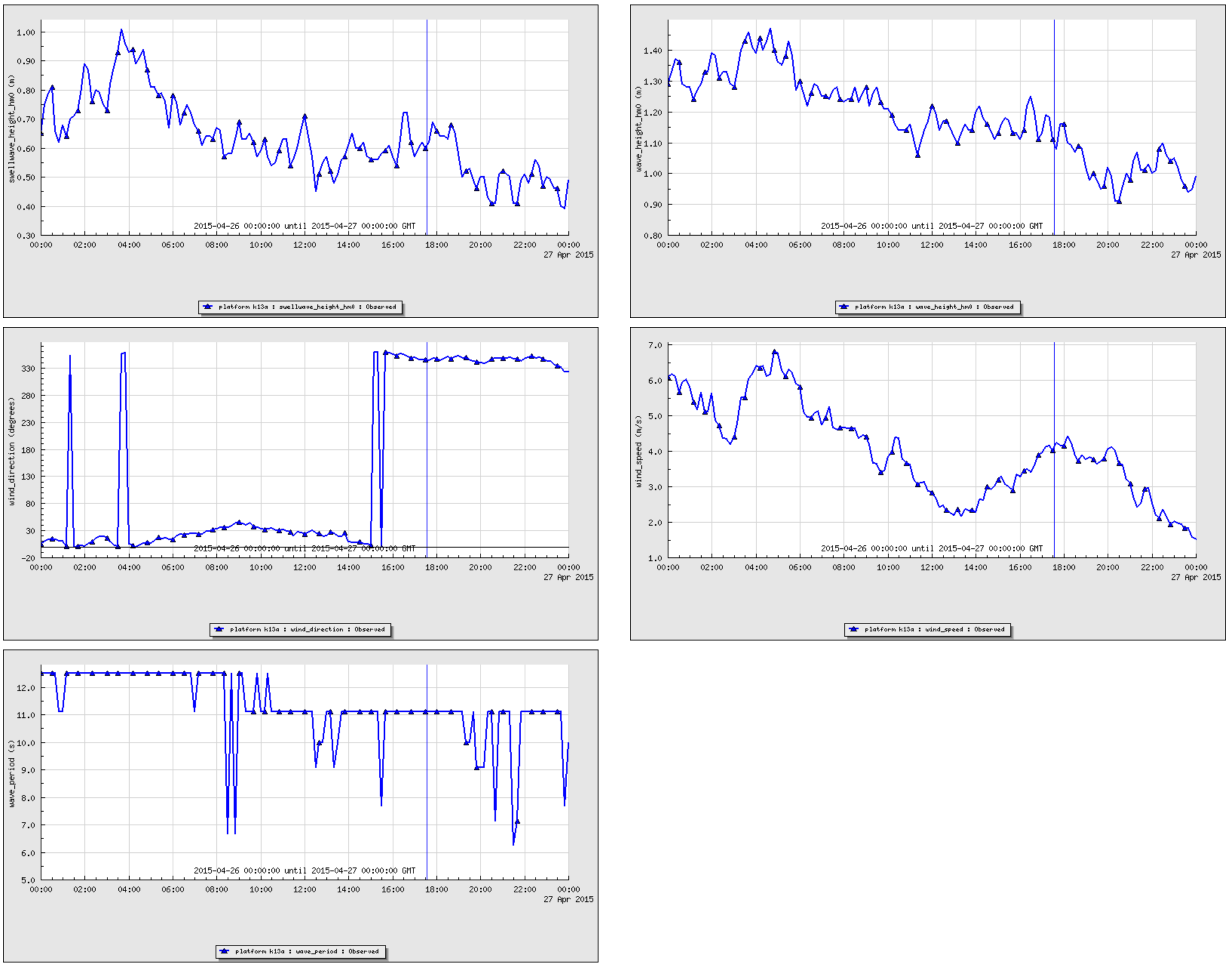

Figure C.1: Buoy data from the k13 alpha wave buoy on 29 April 2015, data retrieved from matroos.deltares.nl.

Portugal buoy data

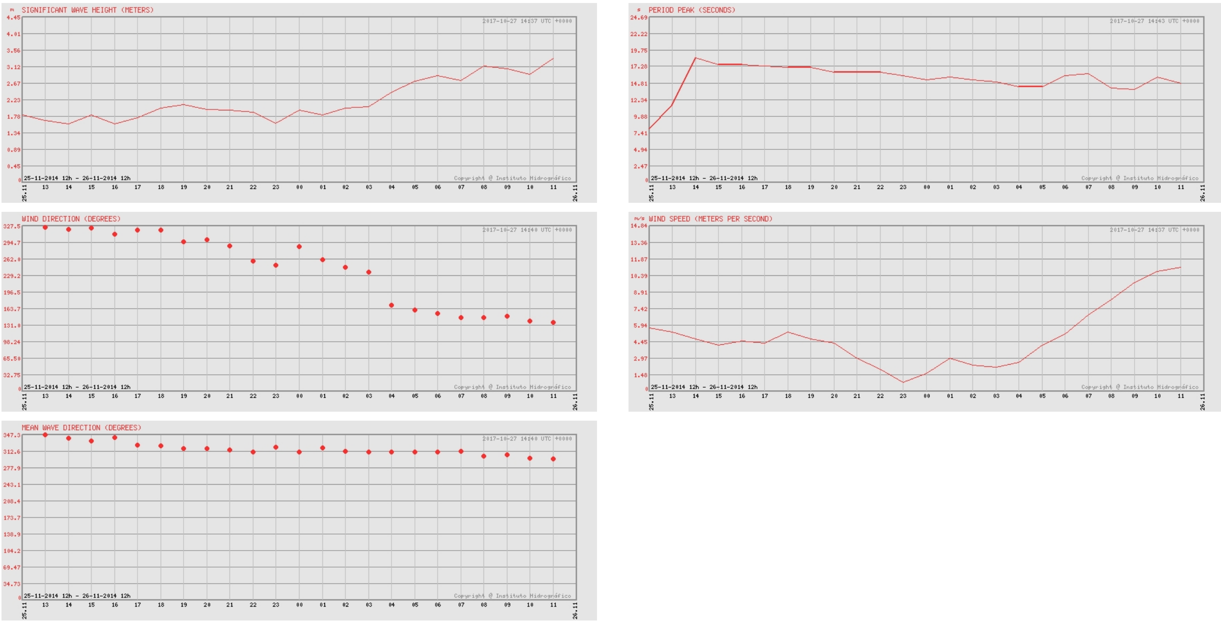

Figure C.2: Buoy data from the Monican 1 wave buoy on 25 November 2014, data retrieved from http://monican.hidrografico.pt/en/default/monican.php.

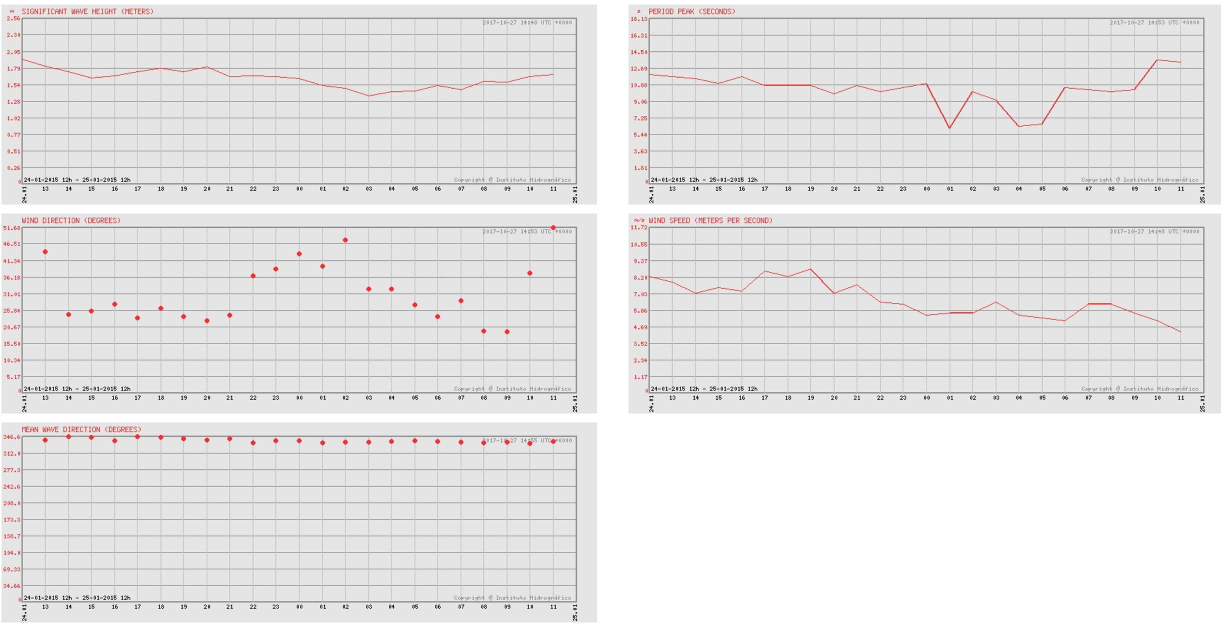

Figure C.3: Buoy data from the Monican 1 wave buoy on 24 January 2015, data retrieved from http://monican.hidrografico.pt/en/default/monican.php.

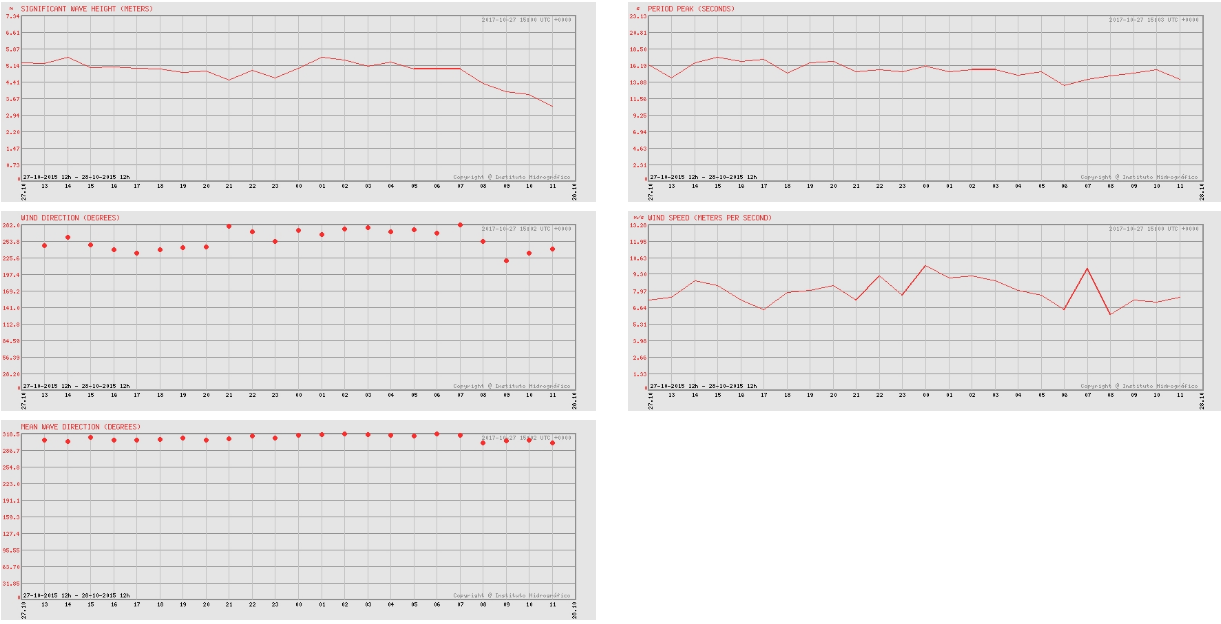

Figure C.4: Buoy data from the Monican 1 wave buoy on 27 October 2015, data retrieved from http://monican.hidrografico.pt/en/default/monican.php.